

Threshold Current Temperature Dependence of Indium Phosphide Quantum Dot Lasers

by

Haji Awang Makarimi Haji Awang Kasim

Cardiff University

**a thesis for the degree of Doctor of Philosophy
in the School of Physics and Astronomy**

November 2014

Declaration

This work has not previously been accepted in substance for any degree and is not being concurrently submitted in candidature for any degree.

Signed _____ (candidate)

Date ____/____/____

Statement 1

This thesis is being submitted in partial fulfilment of the requirements for the degree of PhD.

Signed _____ (candidate)

Date ____/____/____

Statement 2

This thesis is the result of my own investigations, except where otherwise stated. Other sources are acknowledged giving explicit references. A bibliography is appended.

Signed _____ (candidate)

Date ____/____/____

Statement 3

I hereby give constant for my thesis, if accepted, to be available for photocopying and for interlibrary loan and for the title and summary to be made available to outside organisations.

Signed _____ (candidate)

Date ____/____/____

Abstract

InP quantum dot (QDs) lasers grown on GaAs substrates have potential applications in photodynamic therapies, as multi-wavelength sources and for biophotonic sensing. However, to make these devices practical, further improvements are required in threshold current at elevated temperature. The main reason for this study is to identify the factors in the improved performance of lasers with respect to lowering the threshold current density and lowering the temperature dependence of threshold current density for samples with different Ga composition in the upper confining layer (UCL). A new way of determining the mode loss per unit length (α_i) was introduced by extracting the peak net modal gain ($G - \alpha_i$) value of 6 cm^{-1} for a 2-mm-long laser from the averaged value of the modal gain (G), which is more accurate and significant than determining α_i just at the value which loss (at net modal absorption or $A + \alpha_i$) and gain (at net modal gain or $G - \alpha_i$) spectra tend to at low photon energy. The highest α_i value is 2.30 cm^{-1} for $\text{Ga} = 0.54$, 1.10 cm^{-1} for $\text{Ga} = 0.52$, and $\text{Ga} = 0.56$ and 0.58 have almost zero α_i values. I show that to maintain the same peak modal gain at 300 K at a higher temperature, for instance 360 K, one will need to compensate for two situations. First, increasing the current density to achieve 300 K inversion level (or the difference between the quasi-Fermi level separation and the absorption edge) to compensate for the increased nonradiative recombination processes and secondly adding more current density on top of that to compensate for the carrier spreading to higher energy states, in order to reach the peak net modal gain required at 360 K. Spontaneous emission rate spectra measured at $J_{6 \text{ cm}^{-1}}$ show more filled QW states for $\text{Ga} = 0.54$ compared to $\text{Ga} = 0.58$ and compared with data taken at constant inversion level indicates that more carriers are supplied to the $\text{Ga} = 0.54$ to compensate for its high optical mode loss (α_i), when compared to $\text{Ga} = 0.58$. As the temperature increases, some of the energetic carriers from the QW escape to the lower confining layer (LCL) and spontaneous emission measurements show this happens more in the $\text{Ga} = 0.58$ than in the $\text{Ga} = 0.54$. Absorption measurements indicate this is because QD and QW states move closer to the LCL states as the Ga composition in the well increases. Three series of samples grown at different times but with similar designs were compared in the study. Lowering the Al composition in the cladding layer, tends to lower the optical confinement factor (Γ), which causes the threshold current density to be increased in Series 1. The results show that α_i plays the dominant role, not only in lowering the J_{th} but also lowering the threshold current temperature-dependence of these series.

Acknowledgements

Alhamdulillah, first of all I would like to give my heartfelt expression of gratitude to Professor P. M. Snowton, my Supervisor (Advisor) for his relentless encouragement, trust, guidance and support since day one of the long-distance phone call interview until the completion of my PhD. Special thanks to Dr Phil Buckle for advising during the early years and for being my second supervisor. I would also like to thank Dr S. N. Elliot for believing in me and taking me as her co-worker and student in pursuing the challenging experimentations and measurements. Special thanks to Karen Barnett, Dr Sobiesierski, Dr Lang and members of staff for the preparation of wafer samples and supply of liquid nitrogen. An enormous thanks to Professor P. Blood and colleges for the knowledgeable information and important Friday talk sharing-sessions and practices which proved invaluable for the study. Special thanks to Dr. S. Shutts for being technical expert and a friend during those times and also Dr R. Thomas for sharing his knowledge and viva experience. A special thanks also to Dr. Mohamed Al-Ghamdi who came to visit Cardiff University willingly now and then and share his experimental technique using the spectrograph setup. Special thanks to Lewis Kastein for the discussions and knowledge-sharing, including practically implementing the 7 secrets of successful PhD students. Special thanks to Rob Pascoe for helping to calibrate the spectrograph, Peter Rees for the calibration of the EPVS, Martyn Smith for rechecking the Unamplified Spontaneous Emission measurement and Ivan Karomi for sharing the referencing and calm advice.

Alhamdulillah, My heartfelt thanks to my beloved parents Hj Awg Kasim bin Hj Awg Ibrahim and Hjh Dyg Siti Masni bte Hj Md Salleh, especially my mom for her everyday encouragement, advice and prayer, also my Parents-in-Laws, Hj Mahmud bin Hj Ali Husain and Hjh Saidinah bte Hj Hassan and my brothers and brother-in-law and their families for their prayer, relentless support and encouragement. My beloved wife Hjh Shahdinawati bte Hj Mahmud and my six wonderful children; Awg Muhammad Mahiruddin, Awg Muhammad Mahran, Awg Muhammad Majduddin, Dayang Nurul Syahmina, Awang Muhammad Majdi and Dayang Nurul Syadiyah for their prayers, perseverance, support and love since the beginning of this adventurous, knowledge-enriched, exciting and challenging PhD. Special thanks to Hj Md Ishak bin Hj Ahmad and Dr Md Zamri bin Hj Ismail and their families for their support, encouragement and prayer.

Alhamdulillah, I would like to give my highest commendation to His Majesty the Sultan and Yang Di-Pertuan of Negara Brunei Darussalam, for his generous sponsorship and support to my family and I in venturing into this overwhelmingly live-changing experience of living in the United Kingdom, all throughout the completion of this thesis and PhD. Alhamdulillah, Thank you to all, without your support and encouragement none of this will come to surface.

Allah is the light of the heavens and the earth; a likeness of His light is as a niche in which is a lamp, the lamp is in a glass, (and) the glass is as it were a brightly shining star, lit from a blessed olive-tree, neither eastern nor western, the oil whereof almost gives light though fire touch it not- - light upon light- - Allah guides to His light whom He pleases, and Allah sets forth parables for men, and Allah is Cognizant of all things.

The Quran (24 : 35)

Contents

| | | |
|----------|--|-----------|
| 1 | Introduction | 1 |
| 1.1 | Aims and Motivation..... | 1 |
| 1.2 | Thesis Structure..... | 3 |
| 2 | Principles of Semiconductor Quantum Dot Lasers | 5 |
| 2.1 | Introduction..... | 5 |
| 2.2 | Fundamentals of lasers..... | 5 |
| 2.2.1 | Emission and absorption..... | 5 |
| 2.2.2 | Population inversion..... | 8 |
| 2.2.3 | Laser elements..... | 9 |
| 2.2.4 | Optical feedback..... | 10 |
| 2.2.5 | The threshold condition..... | 10 |
| 2.3 | Semiconductor lasers..... | 11 |
| 2.3.1 | Bandstructure..... | 11 |
| 2.3.2 | Fermi-Dirac distribution..... | 12 |
| 2.3.3 | Density of states in semiconductor..... | 13 |
| 2.3.4 | Quantum confinement..... | 15 |
| 2.3.5 | Optical gain in semiconductor lasers..... | 16 |
| 2.4 | Quantum well structure..... | 19 |
| 2.4.1 | Unstrained Quantum well..... | 19 |
| 2.4.2 | Strained Quantum well..... | 22 |
| 2.5 | Gain requirement..... | 26 |
| 2.6 | Non-radiative recombination and thermal activated leakage..... | 29 |
| 2.7 | Self-Assembled Quantum Dots..... | 31 |
| 2.8 | Carrier Distributions in Quantum Dots..... | 33 |
| 2.9 | Origin of temperature dependent threshold current..... | 34 |
| 2.10 | Summary..... | 38 |
| 3 | Experimental Procedures and Structure Design | 39 |
| 3.1 | Introduction..... | 39 |
| 3.2 | Device Structure and design..... | 39 |
| 3.2.1 | Device materials..... | 40 |
| 3.3 | The wafer structure and photoluminescence..... | 42 |
| 3.3.1. | Wafer structure..... | 42 |
| 3.3.2 | The device sample selection on wafer..... | 42 |
| 3.3.3 | Photoluminescence..... | 43 |
| 3.4 | Computational modelling..... | 43 |
| 3.5 | Experimental techniques..... | 44 |
| 3.5.1 | Mounting and handling of devices..... | 44 |
| 3.6 | Current voltage light temperature characteristics..... | 48 |

| | | |
|----------|---|-----------|
| 3.7 | Near-field measurement..... | 52 |
| 3.8 | Spectrum analyser setup..... | 54 |
| 3.9 | EPVS measurement..... | 55 |
| 3.10 | Segmented contact method and the measurement of absorption and gain spectra... 57 | |
| 3.10.1 | Experimental Setup..... | 58 |
| 3.10.2 | Gain and Absorption measurements..... | 60 |
| 3.11 | Spontaneous Emission..... | 62 |
| 3.11.1 | Spontaneous Emission Spectrum..... | 63 |
| 3.11.2 | Current density at different inversion level..... | 63 |
| 3.12 | Calibration..... | 64 |
| 3.13 | Summary..... | 64 |
| 4 | Temperature-Dependent Threshold Current | 65 |
| 4.1 | Introduction..... | 65 |
| 4.2 | Characteristics of the wafers grown..... | 66 |
| 4.2.1 | Selection of wafer for laser and segmented contact devices..... | 66 |
| 4.2.2 | Threshold current..... | 67 |
| 4.2.3 | Threshold current density..... | 69 |
| 4.2.4 | Threshold current with different lengths..... | 70 |
| 4.2.5 | Comparison of threshold current density..... | 72 |
| 4.3 | Laser energy at different sample lengths..... | 73 |
| 4.4 | Optical Absorption Spectra..... | 74 |
| 4.5 | Comparison of peak energies..... | 76 |
| 4.6 | EPVS results with wavelengths..... | 77 |
| 4.6.1 | Transition energy using EPVS for laser and segmented contact devices..... | 77 |
| 4.6.2 | LGS difference on position on the wafer..... | 79 |
| 4.7 | The net modal gain and absorption with lasing energy..... | 80 |
| 4.7.1 | Measurement at room temperature..... | 81 |
| 4.7.2 | Measurement as a function of temperature..... | 85 |
| 4.8 | Current density match, modal Gain (G) and optical mode loss value (α_i)..... | 86 |
| 4.8.1 | Net modal absorption and modal gain..... | 86 |
| 4.8.2 | The Optical Mode Loss Value..... | 87 |
| 4.8.3 | Net modal gain and laser..... | 88 |
| 4.9 | Gain and Absorption spectra..... | 89 |
| 4.10 | Temperature dependence of threshold current density..... | 92 |
| 4.11 | Current density as a function of temperature at 300 K inversion level..... | 93 |
| 4.11.1 | Current density to achieve the same inversion level as 300K..... | 94 |
| 4.11.2 | Inversion level with current density..... | 95 |
| 4.11.3 | Current density at a fixed inversion level..... | 96 |
| 4.12 | Higher inversion and inversion level at a fixed gain as a function of temperature... 97 | |
| 4.12.1 | Changes in current density to achieve higher inversion level..... | 97 |
| 4.12.2 | Inversion level to achieve a fixed peak net modal gain..... | 98 |
| 4.13 | Gain requirement as a function of temperature..... | 99 |

| | |
|---|------------|
| 4.13.1 Gain requirement at 300 K inversion level..... | 99 |
| 4.13.2 Gain requirement at a fixed inversion level..... | 100 |
| 4.14 Unamplified spontaneous emission..... | 101 |
| 4.14.1 Unamplified spontaneous emission at a fixed peak net modal gain..... | 102 |
| 4.14.2 Unamplified spontaneous emission at a fixed inversion level..... | 103 |
| 4.14.3 Rate of spontaneous emission as a function of temperature..... | 104 |
| 4.15 Summary..... | 106 |
| | |
| 5 Comparison of Three Growth Series | 108 |
| 5.1 Introduction..... | 108 |
| 5.2 Threshold current density comparison..... | 108 |
| 5.3 Absorption spectrum comparison..... | 109 |
| 5.3.1 Absorption spectrum energy..... | 109 |
| 5.3.2 Comparison of growth temperature..... | 111 |
| 5.3.3 Comparison of dot large ground state energies..... | 112 |
| 5.4 QW and QD transition energies..... | 112 |
| 5.5 Summary of the transition energies of three growth series..... | 114 |
| 5.6 Optical mode loss comparison..... | 117 |
| 5.7 Summary..... | 120 |
| | |
| 6 Conclusion and Future Work | 121 |
| 6.1 Introduction..... | 121 |
| 6.2 Conclusions for Chapter 4 and 5..... | 121 |
| 6.3 Future work..... | 124 |
| | |
| References | 125 |
| | |
| Publications | 131 |

Chapter 1

Introduction

1.1 Aims and Motivation

The study of quantum dots as the active medium in a semiconductor laser was proposed by Arakawa and Sakaki (1982). The most studied quantum dot laser is the InAs grown on GaAs (Tatebayashi et al. 2003; Jin et al. 2006; Seerkumar et al. 2011), emitting in the 1 - 1.35 μm wavelength range, which have been shown to have extremely low threshold current density down to 10.4 Acm^{-2} operating at 300 K for CW laser diode (Deppe et al. 2009). Similarly, InP quantum dots (QDs) grown on GaAs substrates are of interest because they can address wavelengths in the 650-780 nm range (Zundel et al. 1998; Ryou et al. 2001; Walter et al. 2001; Smowton et al. 2005) and have potential applications in photodynamic therapies, as multi-wavelength sources and for biophotonic sensing (Smowton et al. 2009). However, to make these devices practical further improvements are required in threshold current at elevated temperature.

At relatively high temperature of 300 K and above, the main source of threshold current temperature dependency in all semiconductor lasers originates from carriers that do not contribute to the lasing transition (Asryan and Luryi, 2003). In previous work by Smowton et al. (2011), it has been shown that the reduction in gain caused by thermal carrier spreading over the inhomogeneously broadened quantum dot states has a significant effect on the temperature dependence of threshold current density in InP QD lasers. It was also shown that such effects are not significant in quantum well lasers operating in a similar part of the wavelength spectrum and fabricated from similar materials but are important in InAs QD lasers operating at telecom and datacom wavelengths (Smowton et al. 2005).

The carrier distribution is determined by the temperature and the injection level, and carrier recombination contributes to temperature-dependent threshold current (Smowton et al. 2011). Even high performance low threshold current semiconductor lasers have significant non-radiative recombination, such as Auger recombination, and at least in part is made up from defect-related recombination, thus more improvement in performance through growth optimisation is still needed (Sayid et al. 2010). The concepts underlying the carrier distribution effects are readily understood. At elevated temperatures the population of states producing gain is governed by overall system charge neutrality and Fermi-Dirac statistics (Smowton et al. 2007). For nearly all III-V semiconductors there is an asymmetry in the conduction and valence density of states (Yablonovitch and Kane 1986; Adams 1986), which means that the probability of occupancy of a hole state is relatively small, whereas the electron states can be almost fully occupied. In self assembled QD systems where small numbers of dot states are in close proximity to large numbers of quantum well and bulk states this can lead to severe gain saturation (Matthews et al. 2002) and increases in temperature tend to exacerbate the effect. Modifying the composition and thickness of the layer above the QDs produces changes in strain and state distribution (Ahopelto et al. 1994; Nishi et al. 1999; Seravelli et al. 2007) and can reduce the asymmetry in the quantum well states close to the dot states. In InP dot structures increasing the Gallium content in the layer above the dots – the upper confining layer (UCL) - has resulted in improved threshold current and temperature dependence of threshold current density (Elliott et al. 2012).

The aim of this study is to understand the underlying principles of InP quantum dot lasers in terms of threshold current temperature dependence by varying the Ga composition in the upper confining layer (UCL) of the quantum dots. This also includes obtaining a range of lasing wavelengths, absorption and gain spectra, and studying the effect on these of the difference in Ga composition and growth conditions. By comparing the development of two

previous growth series, we demonstrated further reductions in high temperature threshold current density using strain in the UCL. A detailed experimental study to determine the major factors contributing to the performance was undertaken. In doing this, the aim to reveal the intrinsic performance allowing optimization of future designs will be realised.

1.2 Thesis Structure

Chapter two gives a general overview of the physical principles of semiconductor quantum dot lasers starting by introducing some concepts of semiconductors, the fundamentals of lasers, and some physical properties of semiconductor lasers. It describes the quantum dot systems and recombination in quantum dots. It finishes by discussing the threshold current temperature-dependence in quantum dot systems.

Chapter three presents the device structures which were used for measurements in this thesis beginning by introducing the materials used to construct these structures, then describing the device preparation to transform these structures into working devices, and finally illustrating how these devices can be mounted in order to make them suitable for experimental measurements. The chapter also presents the experimental procedures and equipment used in this thesis to obtain the data presented in the following chapters.

Chapter four presents the data taken from several experiments using four structures, which vary in Ga composition in the upper confining layer of the quantum well, to study the threshold current temperature dependence on the optoelectronic properties of InP/AlGaInP quantum dot laser diodes.

Chapter five compares three growth series with varying Ga composition in the upper confining layer of the quantum well. A summary of the different transition energies of the layer structures, including the quantum well, quantum dots and cladding layers from several experiments is used to illustrate the comparison.

Chapter six outlines the conclusions obtained from the last two chapters and ends by describing some possible future work.

CHAPTER 2

Principles of Semiconductor Quantum Dot Lasers

2.1 Introduction

In this chapter, a general overview of the physical principles of semiconductor quantum dot lasers is discussed. First the fundamentals of lasers such as emission and absorption, population inversion, the laser elements with optical feedback and threshold condition are introduced. Next in this chapter, a description of some concepts of semiconductors including bandstructure, the Fermi-Dirac distribution, density of states, quantum confinement and optical gain will be outlined. The quantum well structure will be described next with unstrained and strained features, followed by the gain requirement. Next are the explanations for the recombination in semiconductor lasers, including modal gain, absorption, spontaneous emission and non-radiative recombination including carrier leakage over the heterobarrier. The formation of the self-assembled QD system, broadening of spectra and the carrier distributions in quantum dots. Lastly, factors relating to the temperature dependence of threshold current are described.

2.2 Fundamentals of lasers

First, I will introduce the fundamentals of lasers such as emission, absorption, population inversion, the feedback process and threshold conditions.

2.2.1 Emission and absorption

When an electron in an atom goes through transitions between two energy states or levels it either emits or absorbs a photon. Conservation of energy requires that the frequency ν

of the photons satisfies $h\nu = E_2 - E_1$ where E_2 is the energy of level 2 and E_1 is the energy of level 1 (Wilson and Hawkes 1998). This can be observed by considering the electron transitions which may occur between the two energy levels of an imaginary atomic system shown in Figure 2.1. Using simplified analysis based on the Einstein coefficients we can work out the electronic transition. In Figure 2.1(a) the electron is in the level E_2 and it may return to E_1 or ground state through a downward process with the emission of a photon called the spontaneous emission. Spontaneous emission is ruled by the Einstein A coefficient. This gives the probability per unit time that the electron in level 2 will come down to level 1 by emitting a photon. The spontaneous photon emission rate, R_{spon} , can be written down as $R_{\text{spon}} = A_{21}N_2$, where the A_{21} coefficient denotes transition from level 2 to level 1 and N_2 is the number of atoms in the excited state (Wilson and Hawkes 1998).

In Figure 2.1(b) the electron is in the lower level E_1 then in the presence of a photon of energy $(E_2 - E_1)$ it may be excited to the upper level E_2 by the stimulated absorption of this photon. The absorption rate between levels 1 and 2 is ruled by the Einstein B coefficient. As mentioned above, the process must be stimulated by the incoming photon. Following the Einstein rule, we write the rate of absorption transition as $R_{\text{abs}} = B_{12}N_1\rho(h\nu)$, where N_1 is the number of atoms in the ground level and B_{12} is the Einstein coefficient for the transition. The $\rho(h\nu)$ is the photon energy density of the electromagnetic wave in J m^{-3} at frequency ν . The $\rho(h\nu)$ clearly stating that only photon with the right frequency ν will be able to induce the absorption transition.

According to Einstein's analysis, the spontaneous emission and stimulated absorption was not complete, so he introduced the third emission. The incoming photon with frequency ν not only can stimulate upward absorption transition but also stimulate downward emission transition. This can be seen in Figure 2.1(c) where the incoming photon with frequency ν stimulates the electron in the upper energy level E_2 to move down to the lower energy state E_1

and simultaneously, two photons of the same frequency ν are emitted. The stimulated emission transition rate R_{sti} is ruled by the Einstein B coefficient and can be written as $R_{sti} = B_{21}N_2\rho(h\nu)$, where B_{21} is the Einstein downward coefficient (Wilson and Hawkes 1998). The three Einstein coefficients are related to each other. In a steady state situation the rate of absorption process equals the sum of the spontaneous and stimulated rates, the relation

$$B_{12}N_1\rho(h\nu) = A_{21}N_2 + B_{21}N_2\rho(h\nu) \quad (2.1)$$

The photon energy density $\rho(h\nu)$ can be determined from Planck's blackbody radiation (Wilson and Hawkes 1998) given as

$$\rho(h\nu) = \frac{8\pi n^3 (h\nu)^3}{h^2 c^3} \frac{1}{e^{\frac{h\nu}{kT}} - 1} \quad (2.2)$$

where n is the refractive index and c the speed of light. The Einstein coefficients A and B can be related to each other by comparing Equation (2.1) and (2.2). It can be shown that $B_{12} = B_{21} = B$ and

$$A = \frac{8\pi n^3 (h\nu)^3}{h^2 c^3} B \quad (2.3)$$

A situation can be created whereby increase of the stimulated emission rate will cause an amplification of light within the cavity of the laser medium (Wilson and Hawkes 1998). This can be done by increasing the photon energy density which makes the stimulated emission rate greater than the spontaneous emission rate. Simultaneously, having more number of electrons in the higher states, N_2 than the lower energy states, N_1 can also increase the probability of the

stimulated emission rate compared to the stimulated absorption rate. This situation is called population inversion.

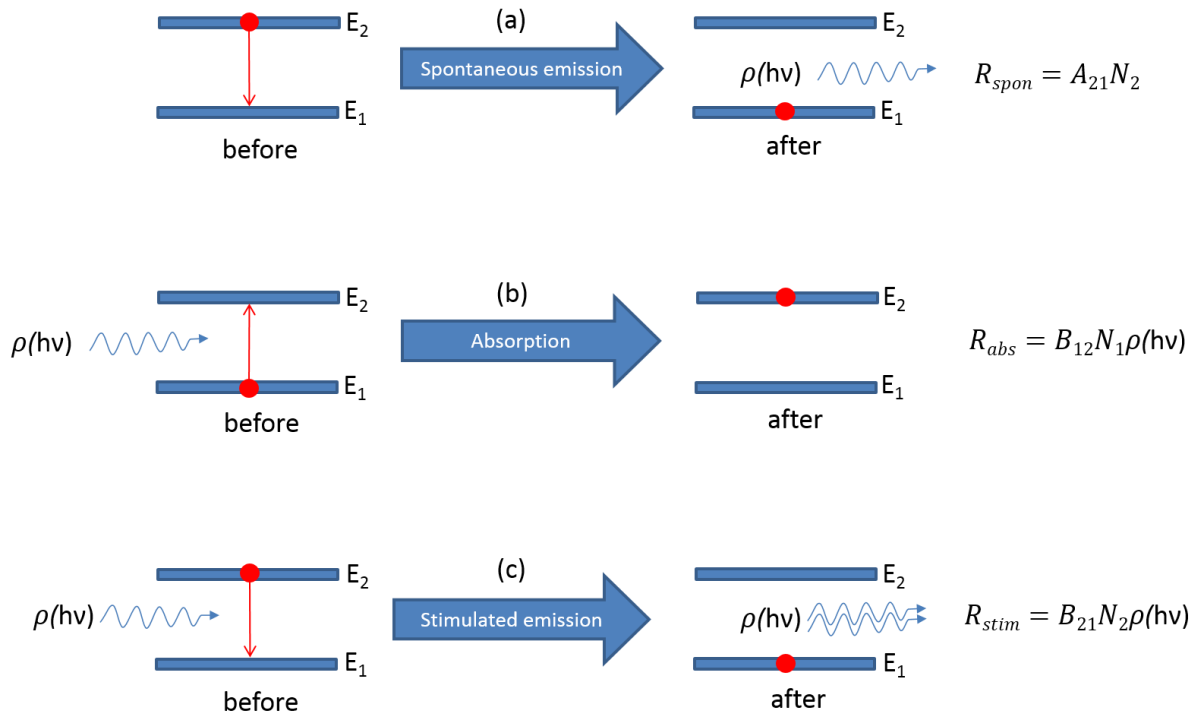


Figure 2.1: Energy level diagram showing (a) spontaneous emission, (b) absorption and (c) stimulated emission. The red dot indicates the state of the electron before and after the transition. The E_1 and E_2 represent lower energy and the upper energy levels, respectively, figure adapted from Wilson and Hawkes (1998, p.170).

Optical gain, G can be defined as the difference between the rate of stimulated emission and absorption in

$$G = B_{21}\rho(h\nu)(N_2 - N_1) \tag{2.4}$$

2.2.2 Population inversion

The population inversion can be created when the number of electrons in the upper energy level surpasses the number of electrons in the lower energy level. This also means that rate of stimulated emission mentioned in section 2.2.1 is higher than the rate of absorption. In relation to semiconductors the two energy levels E_1 and E_2 in Figure 2.1 are replaced by valence

and conduction energy bands. Population inversion in the semiconductor occurs when the number of electrons in the conduction band increases and the number of electrons in the valence band decreases and this is done by forward biasing the p-n junction (Blood 1991). When the p-n junction is forward biased with a voltage that is equal or greater than the voltage corresponding to the energy gap, E_g/e , the electron and holes are injected across the junction in sufficient numbers to create a population inversion in the narrow zone called the active region. Once the population inversion is achieved, the rate of stimulated emission must be increased beyond that of the spontaneous emission and to do this optical feedback is required (Blood 1991).

2.2.3 Laser elements

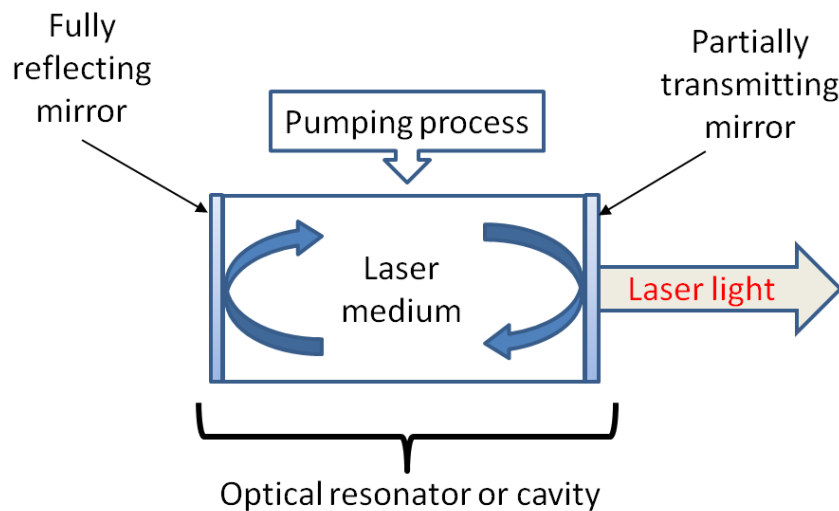


Figure 2.2: Simplified schematic of a typical laser, figure adapted from Silfvast (1996, p.1).

A laser is a device that amplifies light. There are three essential parts to a laser as shown in Figure 2.2. First is the laser medium where the population inversion and amplification will occur and this part can be any material: solid, liquid or gas, but in this case, it is the semiconductor material. The second part is the pumping process which is an energy input requirement to place the electrons in a higher energy level. The third part is the optical feedback

requirement where the light produced in the laser medium is bounced back into the laser medium with the help of two mirrors for amplification (Silfvast 1996).

2.2.4 Optical feedback

Stimulated emission rate has to be greater than the spontaneous emission rate and the way to achieve this condition is by amplification of the light within the laser medium by a method called optical feedback as mentioned in section 2.2.3 and this is done by using two mirrors, one at each end of the laser cavity. In a semiconductor laser a mirror can be formed by a different refractive index between the laser medium and the air interface. The reflectivity of the mirror, R is defined as the fraction of the incident intensity reflected by the mirror and can be shown to be given by the simplified equation (Wilson and Hawkes 1987)

$$R = \frac{(n_1 - n_2)^2}{(n_1 + n_2)^2} \quad (2.5)$$

for light of normal incidence, where n_1 is the refractive index of the laser medium and n_2 is the refractive index of the air which is usually taken as unity.

2.2.5 The threshold condition

The laser action in the semiconductor laser medium is reached when the rate of amplification or gain is balanced by the rate of loss. The cavity loss within the system (Wilson and Hawkes 1998) is due to the following reasons:

- a. Transmission at the mirrors
- b. Absorption and scattering at the mirrors
- c. Diffraction losses at the mirrors
- d. Internal loss, the coefficient α_i

Therefore, all the total cavity losses must be compensated by the amplification of the optical gain before lasing can take place to sustain oscillation.

2.3 Semiconductor lasers

Before describing the balance of loss with gain in more detail, this section will describe band structures, Fermi-Dirac distribution, density of states, quantum confinement and optical gain in the semiconductor laser.

2.3.1 Bandstructure

Atoms in semiconductor materials are connected by covalent bonds. When considering two atoms with a single covalent bond near each other, the outer valence electron of one atom can arrange itself either into lower-energy bonding or high-energy anti-bonding charge distributions.

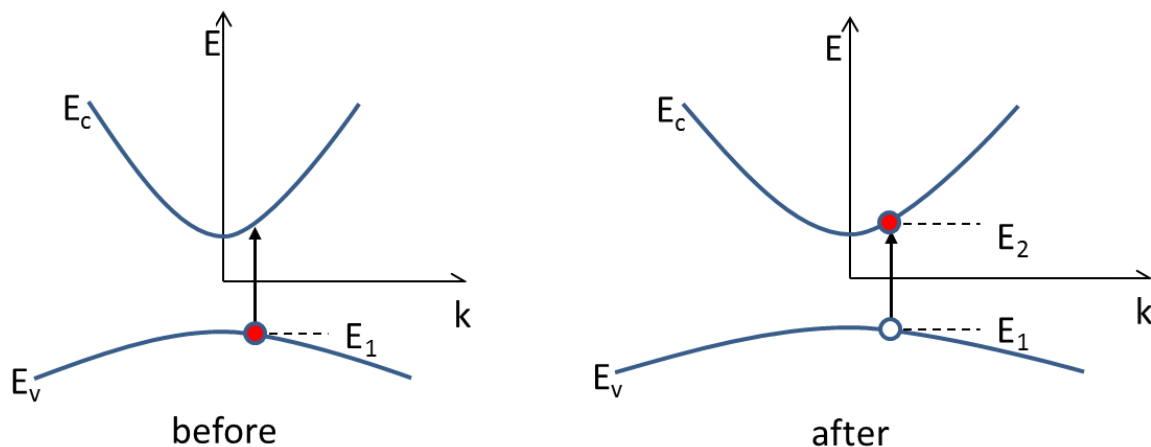


Figure 2.3: Electron energy against wave number in a semiconductor. The transition of an electron from a bound state in the valence band (E_1) to a free carrier state in the conduction band (E_2). The before and after diagrams show the transition of the electron to the conduction band (E_c) leaves a hole in the valence band (E_v), figure adapted from Coldren et al. (2012, p.7).

The two electrons within these atoms can occupy same the lower-energy bonding level (having opposite spin), while the higher energy anti-bonding level remain empty. When a third atom is also considered, a third energy level charge distribution is possible. When N atoms are covalently bonded, bands of energies are formed between the lowest-energy bonding state and the highest-energy anti-bonding state (Coldren and Corzine 1995). The most significant bands of the lower and higher band are called the valence and conduction bands, respectively as shown in Figure 2.3. At 0 K, the bound state of the valence band will be full of electrons while the free state of the conduction band will not have any electrons. As temperature increases the electrons will be excited to move from the valence band to the conduction band leaving a hole behind in the valence band as seen in Figure 2.3.

The energy and momentum of the system is conserved in the transition of electrons as shown in the E - k curve. When the incident photon interacts with an electron, the momentum of the collision is negligible compared to the momentum of the electron's transition (Coldren and Corzine 1995). It is considered that the conduction band and the valence band have the same wave number vector, k during these transitions which is the vertical transition as shown in Figure 2.3. Semiconductor material having the valence band maximum occurring at the same k value as the conduction band minimum is also known as a direct band-gap semiconductor (Wilson and Hawkes 1998).

2.3.2 Fermi-Dirac distribution

In the case of understanding how the carriers fill the energy states in a semiconductor, first we need to know the state occupation probability $f(E)$ at a given energy E which will allow us to relate the carrier density to the ranges of energies that must be occupied. The Fermi-Dirac distribution (Coldren and Corzine 1995) is the appropriate function for electrons in solids such as semiconductors

$$f(E) = \frac{1}{e^{(E-E_f)/kT} + 1} \quad (2.6)$$

Where E is the energy of the carrier, E_f is the Fermi energy, k is the Boltzmann constant and T is the temperature. The value of the probability distribution is equal to one-half, when $E = E_f$.

2.3.3 Density of states in semiconductor

The density of states $\rho(E)$ at any particular energy E is defined as the number of electronic states per unit volume per unit energy (Coldren and Corzine 1995). It is an important requirement for calculating the distribution of electrons and holes in the conduction and valence bands when it is multiplied by the states occupation probability (equation 2.7) as shown in Figure 2.4. This is important in understanding some fundamental properties of the photon-matter interaction such as absorption and gain (Thompson 1980). The carrier density, N , as the integral over energy of the density of electrons in the conduction band will evaluate the total electron density N_e (Coldren and Corzine 1995) as follows

$$N_e = \int \rho_e(E) f_e(E) dE \quad (2.7)$$

where $\rho_e(E)$ represents the density of states in the conduction band. Likewise, the integral over the energy of the density in the valence band will evaluate the total hole density N_h (Coldren and Corzine 1995) as follow

$$N_h = \int \rho_h(E) f_h(E) dE \quad (2.8)$$

where $\rho_h(E)$ representing the density of states in the valence band. A plot of density of state function versus carrier density and Fermi function is shown in Figure 2.4 for bulk semiconductor under forward bias under non-equilibrium conditions at $T = 0$ K and 300 K. Figure 2.4 shows schematic representations of (a) density of states of electrons and holes in the conduction and valence bands, (b) the Fermi-Dirac occupational probability and (c) shows the Fermi-Dirac distribution with respect to the density of states (Coldren and Corzine 1995).

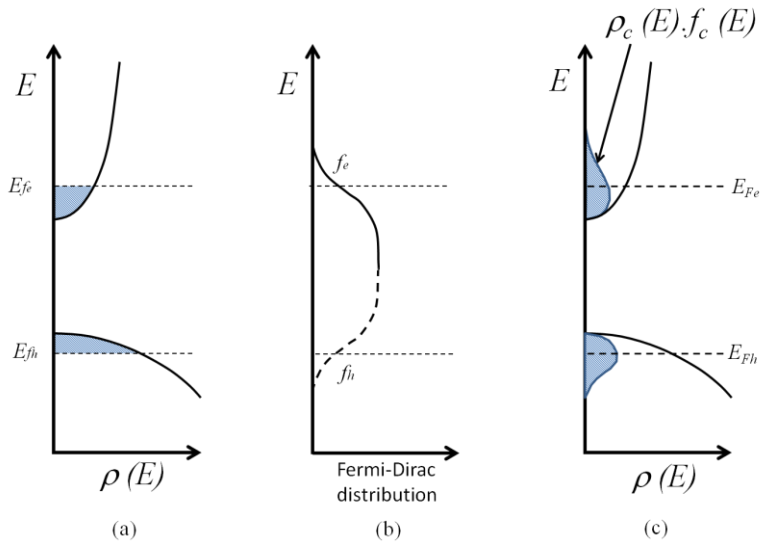


Figure 2.4: Schematic representation of density of state of a bulk semiconductor at (a) $T = 0$ K and (b) Fermi-Dirac distribution and (c) $T = 300$ K, adapted from Blood (1991, p.234).

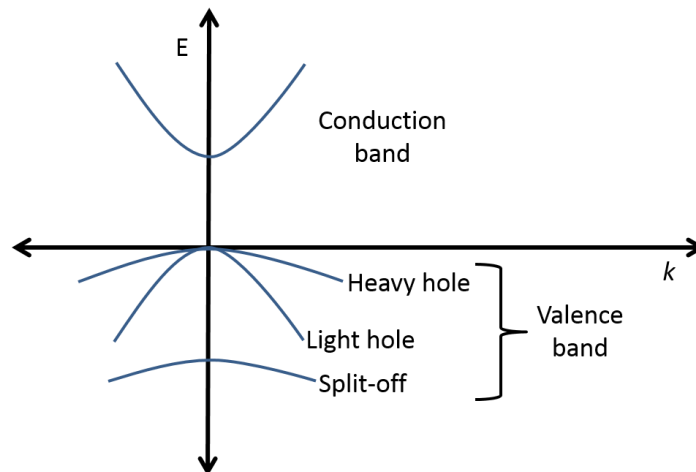


Figure 2.5: Schematic diagram of the heavy-hole (hh), the light-hole (lh) and the split-off (SO) sub-bands of the valence band and the conduction band, figure adapted from Coldren et al. (2012, p.612).

The valence band has three sub-bands, the heavy-hole (hh), the light-hole (lh) and split-off (so) bands. Only the hh and lh bands tend to be important under normal operating conditions, since the split-off band is suppressed by the other two band by the spin-orbit splitting energy (Coldren and Corzine 1995). The light hole-band has an effective mass almost equal to that of an electron, which is a fraction of the heavy-hole effective mass (Thompson 1980; Coldren and Corzine 1995; Wilson and Hawkes 1998). Figure 2.5 shows the schematic

representation of the heavy-hole, light-hole and split-off sub-bands of the valence band and the conduction band.

2.3.4 Quantum confinement

Quantum confined semiconductor structures confine the electrons and holes in one or more directions. These artificial structures are generally in the size of nanometres. A bulk crystal usually does not change its optical properties no matter how small you try to cut it as long as the dimension is still large, but once it is cut down to microscopic level then that is totally a different situation. The size dependence of optical properties of the very small crystals is the result of the quantum confinement effect (Fox 2010).

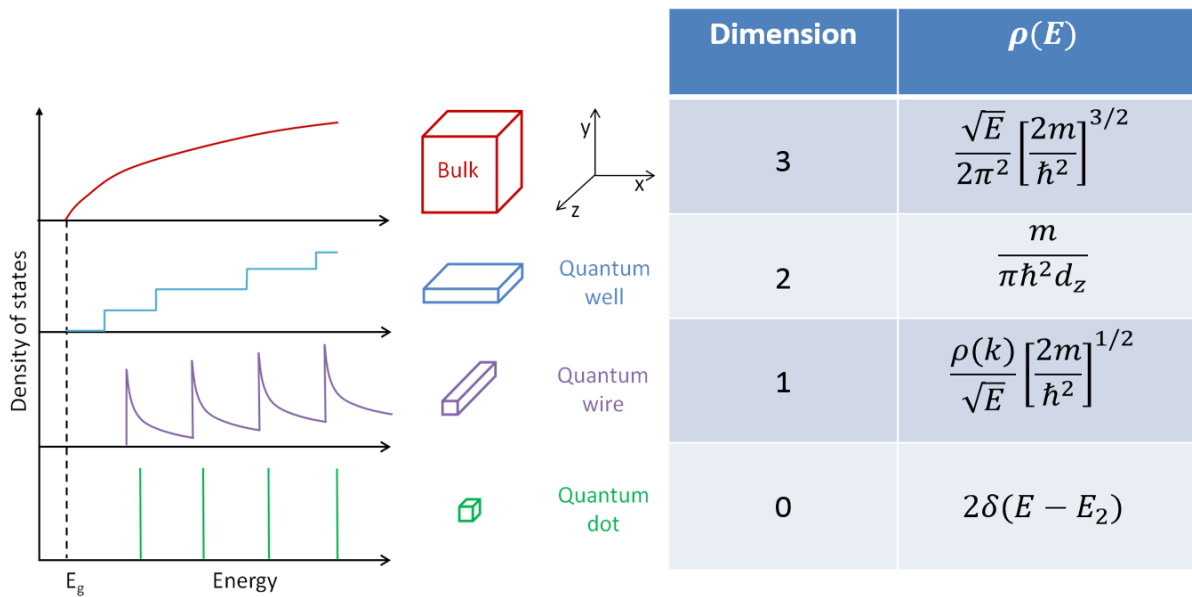


Figure 2.6: Schematic representation of quantum wells, wires and dots [adapted from Fox 2010, p. 143]. The generic shape of the density of states function for electrons in the conduction band of a semiconductor with gap E_g is shown for each type of structure. Table showing dimension and density of states of each quantum confinement, table reproduced from Coldren et al. (2012, p.612).

Figure 2.6 shows the different types of structures from the bulk material to the quantum confined structures of quantum well, quantum wire and quantum dot with their individual density of states. The electrons and holes in bulk semiconductor materials are free to move in

their respective bands in all three dimensions which means that they have three degrees of freedom. The electrons and holes in a quantum well however are confined in one direction, and thus have two degrees of freedom in the other 2 directions (2-Dimensions). In the same situation, the quantum wire has 1-Dimension and quantum dot has 0-Dimension of freedom. In the case of the quantum dot, the motion of electrons and holes is restricted in all three dimensions, rendering the electrons and holes in one location only in the structure. In short the confinement of motion of the charge carriers lead to two situations. One is that the energy of a particle at rest is increased by the quantum confinement and second is that the functional form of the density of states is changed (Fox 2010). This is good because, in general, recombination will occur throughout the density of states of the different structures as determined by the Fermi-Dirac population function, but the amount of recombination will decrease as the density of states is reduced from the bulk material to the quantum dots.

2.3.5 Optical gain in semiconductor lasers

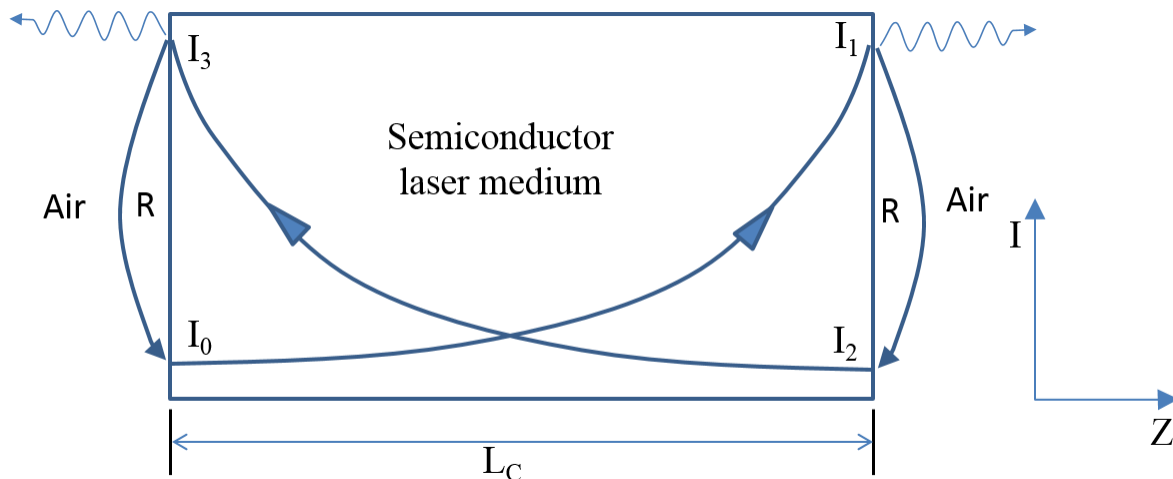


Figure 2.7: The schematic diagram of the light amplification through the laser medium with the cavity length and reflectivity R , adapted from Blood (1991, p.234).

In a semiconductor, gain can only occur when the stimulated emission rate is greater than the absorption rate i.e. when a population inversion exists. When this stimulated emission

rate is higher than the spontaneous emission within the cavity length of the laser, coherent emission will occur. Moreover, the threshold conditions must be met before any lasing can occur (Blood 1991).

In Figure 2.7 the spontaneous emission, I_0 at the beginning or the initial intensity of light is travelling towards the first edge of the laser medium, will have an intensity of I_1 which is given by the relation (Blood 1991),

$$I_1 = I_0 e^{(G_{th} - \alpha_i)L_c} \quad (2.9)$$

where G_{th} is the modal gain at threshold, α_i is the internal loss per unit length and L_c is the cavity length. Then when the light is reflected from the mirror at the first edge of the laser medium it will have an intensity of I_2 which is given as

$$I_2 = RI_1 = RI_0 e^{(G_{th} - \alpha_i)L_c} \quad (2.10)$$

where R is the mirror reflectivity. When the light reaches the second edge of the laser medium it will have an intensity of I_3 which is given as

$$I_3 = I_2 e^{(G_{th} - \alpha_i)L_c} = RI_0 e^{2(G_{th} - \alpha_i)L_c} \quad (2.11)$$

When the light is then reflected from the mirror at the second edge of the laser medium it will have an intensity of I_4 which is given as

$$I_4 = RI_3 = R^2 I_0 e^{2(G_{th} - \alpha_i)L_c} \quad (2.12)$$

Conserving the emission, $I_4 = I_0$, the equation (1.2) can be written as

$$1 = R^2 e^{2(G_{th} - \alpha_i)L_c} \quad (2.13)$$

Rearranging equation (1.6), the modal gain at threshold can be written as

$$G_{th} = \alpha_i + \frac{1}{L_c} \ln(R^{-1}) \quad (2.14)$$

The local gain at threshold g_{th} can be obtained from this relation

$$\Gamma g_{th} = G_{th} \quad (2.15)$$

where Γ is the optical confinement factor (Blood 1991). Γ is defined as the percentage of the intensity of light which has been confined by the semiconductor laser medium (Coldren and Corzine 1995).

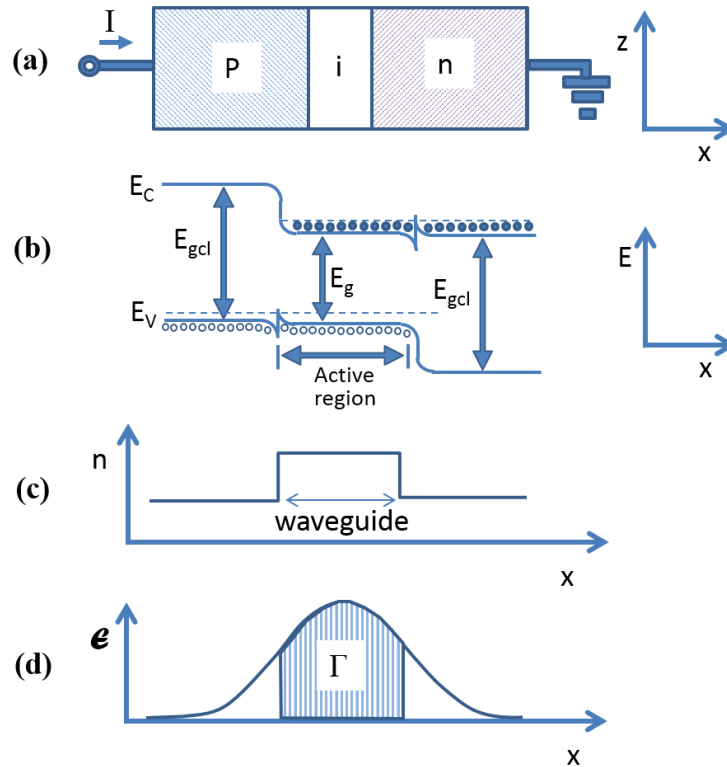


Figure 2.8: Aspects of the DH diode laser: (a) a schematic of the material structure; (b) an energy diagram of the conduction and valence bands vs transverse distance; (c) the refractive index profile; (d) the electric field profile with the confinement factor Γ , figure adapted from Coldren et al. (2012, p.11).

Figure 2.8 (a) shows a double-heterostructure (DH) diode laser. The thin slab of the active medium of the undoped material is sandwiched between p- and n-type cladding layer, which have a higher conduction-valence band energy gap. Since the band gap of the cladding layer is large, light generated in the active region will not have enough photon energy to be absorbed in cladding layer, which is $E_{2l} = h\nu < E_{gcl}$ (Coldren and Corzine 1995). Population inversion is produced in the thin active region. Figure 2.8(b) shows the energy profile that confines the injected charge carriers, which is forward biased and this increases the chances of the electrons and holes recombining. Figure 2.8(c) shows that the active region has a higher

index than the cladding layers, which ensures the formation of an optical waveguide. Cleaving the facet of the laser perpendicular to the z-direction will form the necessary resonant cavity for optical feedback. The Figure 2.8(d) shows the area under the optical field intensity used in calculating the optical confinement factor Γ in the semiconductor laser medium (Blood 1991; Silfvast 1996).

2.4 Quantum well structure

The III-V quantum well semiconductor structure will be discussed in this section. First, the unstrained quantum well, then followed up with the strained quantum well.

2.4.1 Unstrained Quantum well

Before threshold condition for gain is achieved, the Bernard-Duraffourg condition (1961) must be satisfied, which requires that the quasi-Fermi level separation energy must be higher than the band-gap energy, where $F_c - F_v > h\nu$. This creates a population inversion as mentioned in Section 2.2.2., which is used for achieving stimulated emission for lasing in a semiconductor laser. This condition is satisfied and further explained in the following figures. Figure 2.9(a) shows an ordinary semiconductor in which the very light conduction band mass and the heavy valence band mass cause asymmetry in their effective mass (Yablonovitch and Kane 1986). Figure 2.9(b) shows Fermi-Dirac distribution as a function of the total density of electrons and holes of the ordinary semiconductor, adapted from Wu (2008) where $m_h^* > m_e^*$.

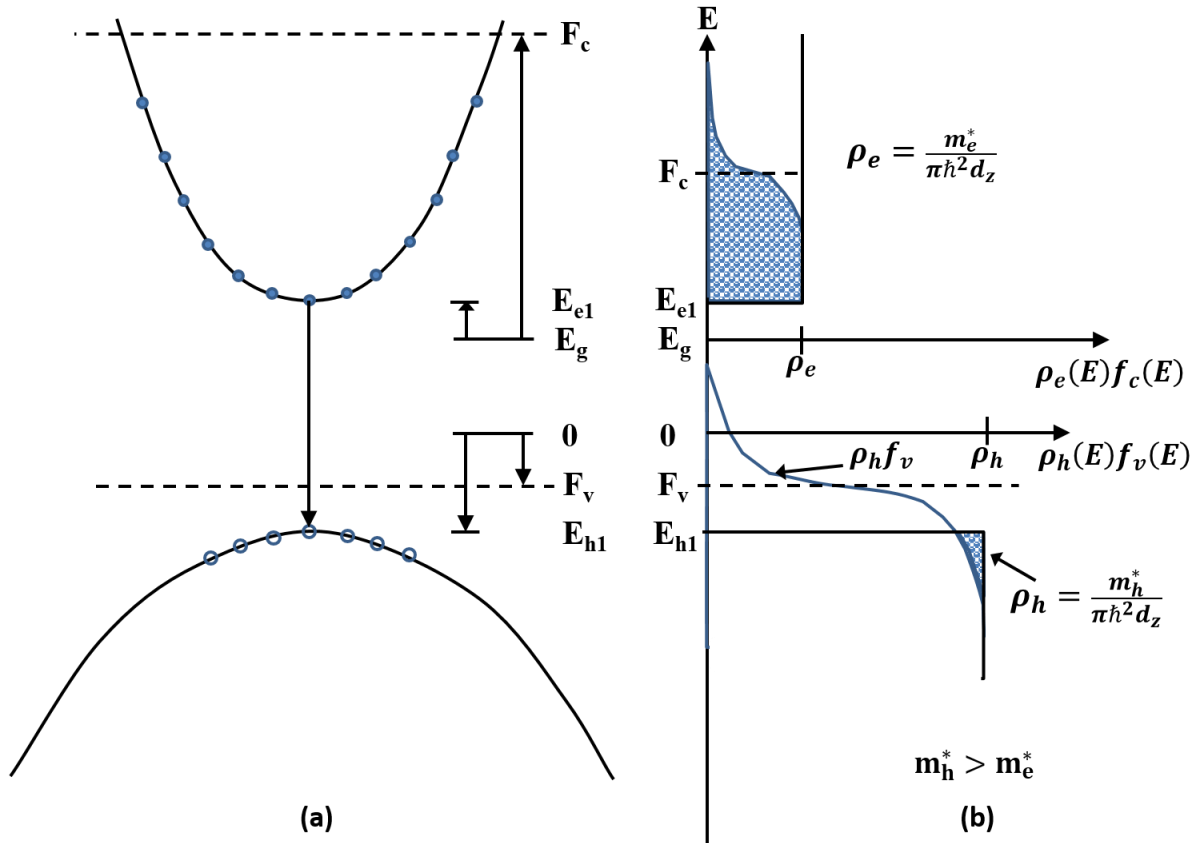


Figure 2.9: (a) An ordinary semiconductor in which the conduction band carrier density is degenerate and the valence band carrier density is non-degenerate due to the effective mass non-symmetry, at gain threshold, adapted from Yablonovitch & Kane (1986, p.504). (b) Fermi-Dirac distribution as a function of the total density of electrons and holes of the ordinary semiconductor $m_h^* > m_e^*$, adapted from Wu (2008, p.3).

The upper lasing level of the conduction band is filled with degenerate electrons, while the lower lasing levels of the valence band were not actually empty (Yablonovitch and Kane 1986). This situation shows that the hole density of states (ρ_h) at the top of the valence band is almost full with electrons, which means that it is lasing down from a filled state to an almost filled state. This is far from the ideal situation. The more ideal situation is based on equal conduction and valence band effective masses as shown in Figure 2.10. Figure 2.10(a) shows a symmetrical conduction and valence band (Yablonovitch and Kane 1986; Wu 2008). Figure 2.10(b) shows Fermi-Dirac distribution as a function of the total density of electrons and holes of the idealised semiconductor, with lower carrier injection density at gain threshold

(Yablonovitch and Kane 1986; Wu 2008). This ideal situation is known as the Bernard-Duraffourg (1961) condition or the transparency condition, where $F_c - F_v = E_{e1} - E_{h1}$, which will be useful in the coming section.

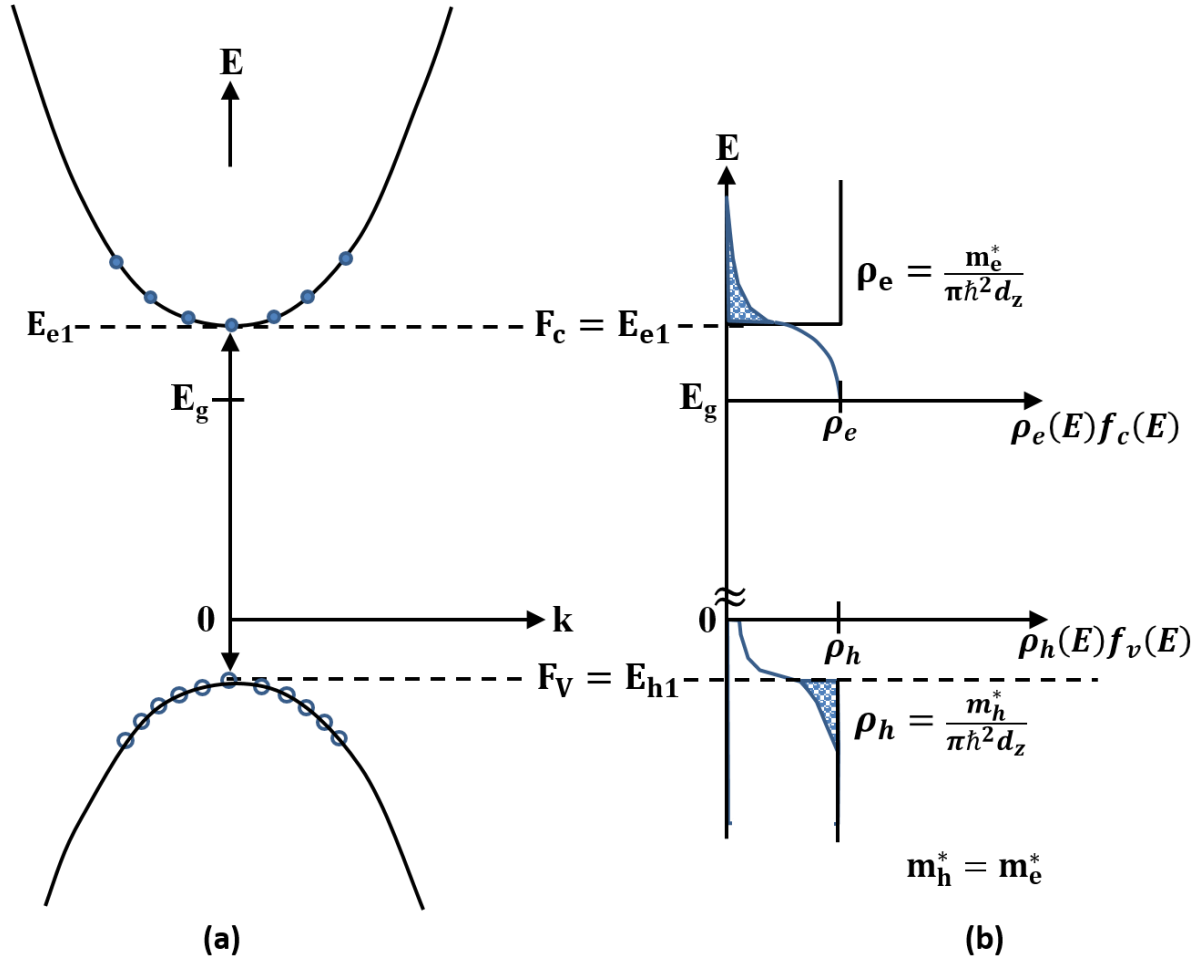


Figure 2.10: (a) An idealised semiconductor with lower carrier injection density at gain threshold, which shows equal effective masses, adapted from Yablonovitch & Kane (1986, p.504). (b) Fermi-Dirac distribution as a function of the total density of electrons and holes of the idealised semiconductor, where $m_h^* = m_e^*$, adapted from Wu (2008, p.3).

The ideal semiconductor with $m_h^* = m_e^*$ has a certain advantage for the application of semiconductor lasers. With the reduced hole effective mass, it allows the Bernard-Duraffourg (1961) condition for population inversion to be fulfilled at a lower carrier density (Ghiti 1988). If this can be achieved, threshold current J_{th} in a semiconductor laser, which must overcome the losses such as spontaneous emission, non-radiative surface recombination on the two faces

of the active region and the non-radiative Auger recombination can be reduced (Yablonovitch and Kane 1986). The reduction of the effective mass of the valence band can be achieved by introducing strain in the quantum confined layer of a quantum well laser. Next, let us look at the effect of strain in quantum well lasers.

2.4.2 Strained Quantum well

Figure 2.11 shows the band gap and lattice constant for various III-V semiconductors at room temperature. The direct band gap $\text{Ga}_{0.52}\text{In}_{0.48}\text{P}$ which is lattice matched to the GaAs is emphasised in the Figure 2.11. The position of the bandgap energy shown in Figure 2.11 will be changed in accordance with the change in strain and the Ga composition later in this section. When strain is added, by varying the Ga composition (x) in the $\text{Ga}_x\text{In}_{(1-x)}\text{P}$, this will create a mismatch of the lattice constant. The lattice parameter will vary between that of GaP to InP, creating tensile and compressive strain, respectively. The effect of strain on the bandgap and the band structure can improve the performance of strained quantum well lasers compared to unstrained quantum wells as mentioned in the previous Section 2.4.1. Pikus and Bir (1959) devised the basic theory needed to explain the effect of mismatch or deformation on the valence bands: heavy hole (hh), light hole (lh) and split-off (so) bands. Background knowledge and details of the strain Hamiltonian by Pikus and Bir (1959) which is extensively discussed in Coldren and Corzine (1995), has been studied previously by Mogensen (1996) and can be found there.

The relevant understanding for this study is the effect of changing the strain and material composition on the strained band energy shift and its magnitude as shown in Figure 2.12. Figure 2.12 shows two situations, first is the effect of tensile and compressive strain on the qualitative band edge shifts in the conduction and valence band (top red and blue diagrams). The obvious effect is the shifting of the lh above the valence band in the tensile strain region

and the shifting of the hh above the valence band in the compressive strain region. Secondly, Figure 2.12 (lower black diagram) shows the qualitatively the effect of shift in the bulk material as Ga composition is varied in $\text{Ga}_{(x)}\text{In}_{(1-x)}\text{P}$ between the binary constituent endpoints of GaP and InP without the effect of strain as mentioned in Figure 2.11 in this section. By looking only at the tensile region of the top diagram in Figure 2.12, one can see that the tensile strain ($\text{Ga}_{(x)}\text{In}_{(1-x)}\text{P}$) produces a reduction in the energy gap.

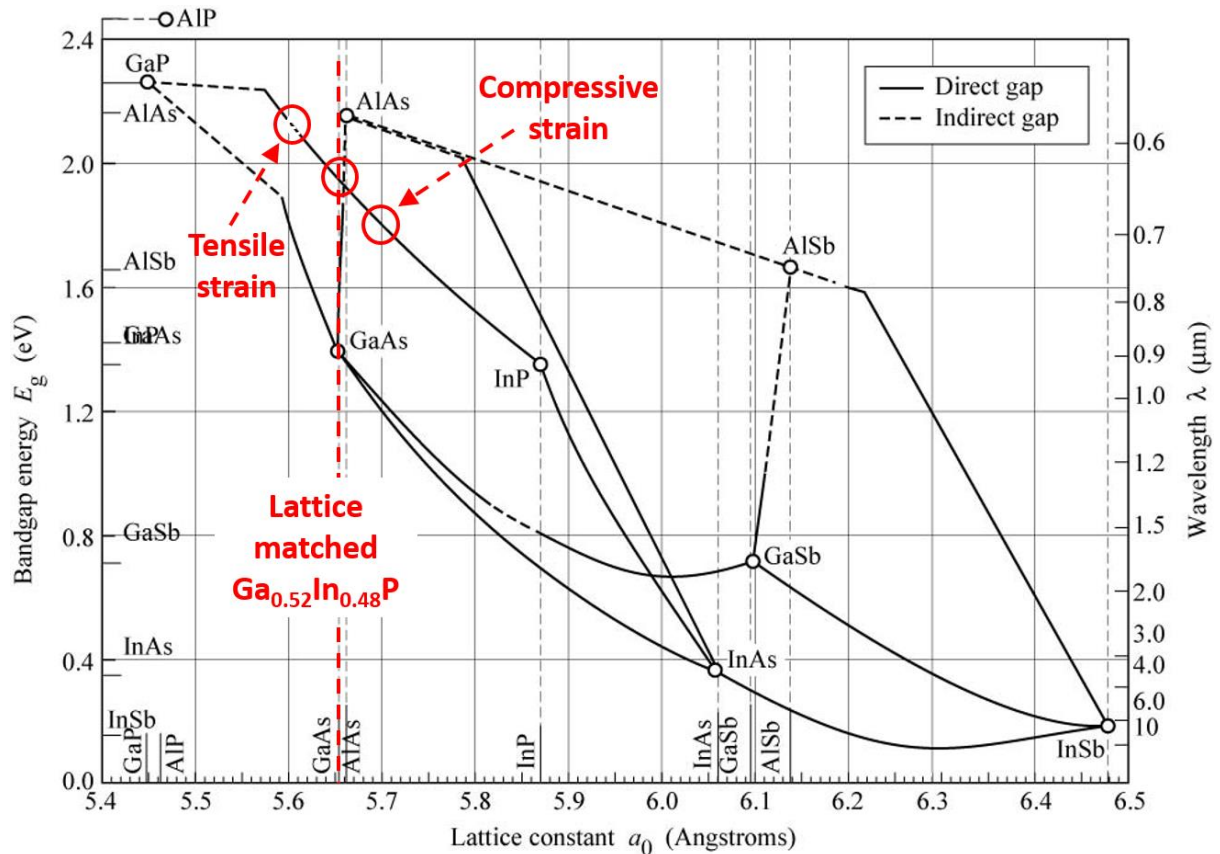


Figure 2.11: Bandgap energy and lattice constant of various III-V semiconductors at room temperature, reproduced from Tien (1988) cited in Wu (2008, p.7). Lattice matched $\text{Ga}_{0.52}\text{In}_{0.48}\text{P}$ with lattice constant 5.653 Å, reproduced from (Ioffe, 2001).

However, looking at the lower part of Figure 2.12 at the same tensile strain region, varying the Ga composition of the $\text{Ga}_{(x)}\text{In}_{(1-x)}\text{P}$ resulted in an increase in bandgap which is greater than that due to the tensile strain effect (Smowton and Blood, 1996). Therefore, the overall bandgap magnitude in the strained layer caused by both situations will increase and this

has the opposite effect at the compressive strain region. It is important to maintain a distinction between effects due to changes in composition and changes due to strain in this study.

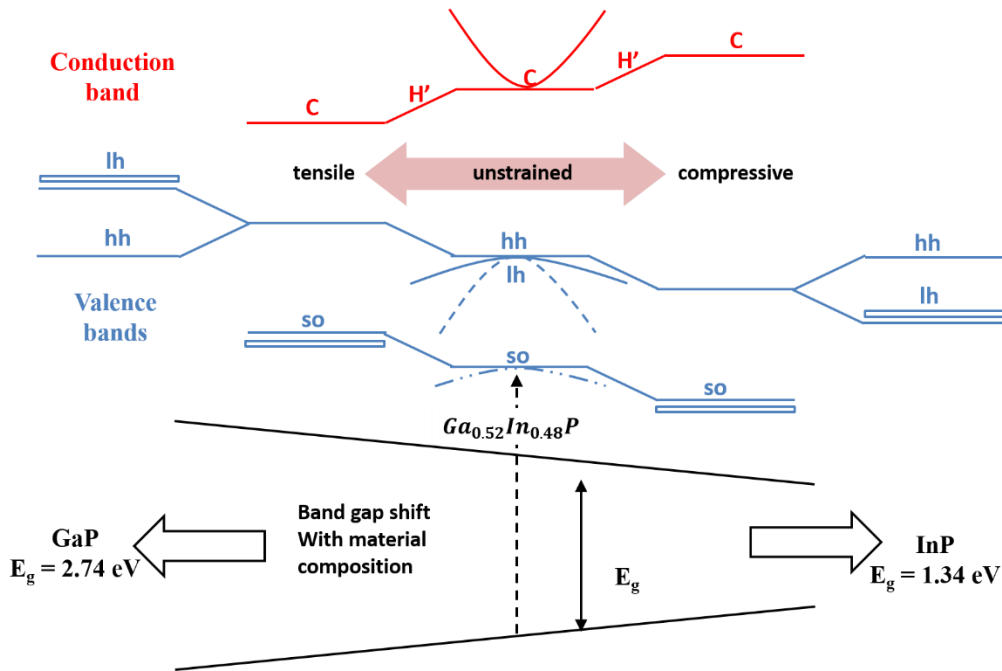


Figure 2.12: The qualitative band edge shifts in the conduction (in red) and valence (in blue) bands with the limit of the tensile and compressive strains, adapted from Coldren et al (2012, p.652); Wu (2008, p.8) and additional drawing of the related conduction c band and valence: lh, hh and so bands. The bottom diagram (in black) shows the bandgap variation for $Ga_{(x)}In_{(1-x)}P$ as a function of Ga composition, adapted from Mogensen (1996, p.42).

In addition to the active material, layers of $(Al_xGa_{1-x})_{0.52}In_{0.48}P$ are included as barriers and waveguides. The bandgap of $(Al_xGa_{1-x})_{0.52}In_{0.48}P$ is given by $E_g = 1.91 + 0.61x$, taken from Bour (1993). Table 2.1 shows structure values of importance in this study, which will be useful in the results chapter later.

| Symbol | Structure | Bandgap (E_g) | Value (eV) |
|-----------------------------------|---------------------------------------|--|------------|
| InP | quantum dots (QD) | Measurement of QD large ground state (LGS) | 1.719 (*) |
| $Ga_xIn_{1-x}P$ | quantum well (QW) | $1.35 + 0.76y + 0.63y^2$ at $x = 0.52$ | 1.916 |
| $(Al_xGa_{1-x})_{0.52}In_{0.48}P$ | Lower confining layer (LCL) waveguide | $1.91 + 0.61x$ at $x = 0.30$ | 2.093 |

Table 2.1: Bandgap (E_g) for strained quantum dots in Quantum well structure. InP QD large ground state (LGS) measured value (*) taken from Elliott et al. (2012, p.4), $Ga_xIn_{1-x}P$ formula taken from

Smowton and Blood (1997, p.440) with $y = x$ to match with the study [33] and $(Al_xGa_{1-x})_{0.52}In_{0.48}P$ formula taken from Bour (1993), cited in Smowton and Blood (1997, p.440).

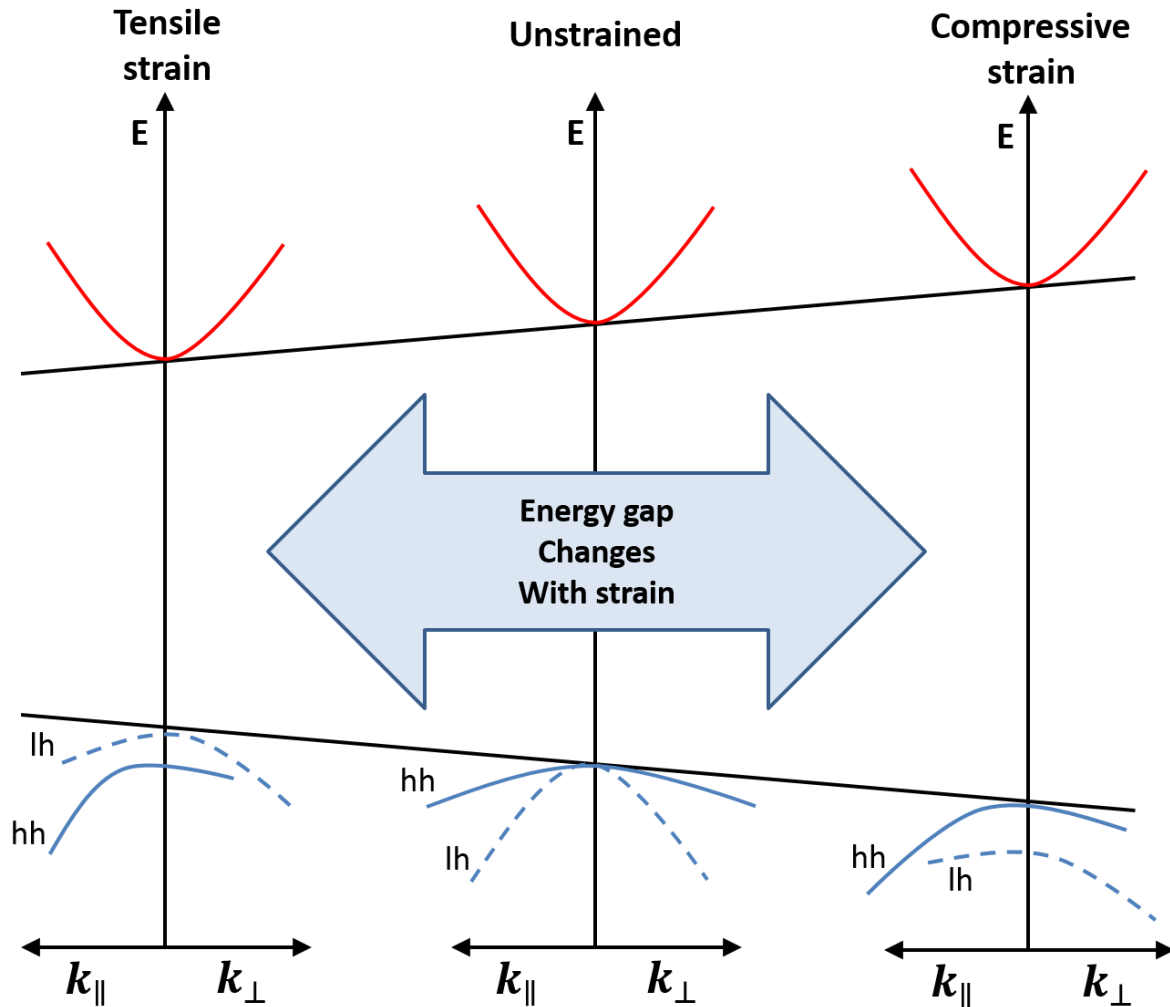


Figure 2.13: The effect of strain on the parabolic band structure of a direct band gap semiconductor, which results in different effective masses, adapted from Coldren et al (2012, p.627) and Mogensen (1996, p.45). \parallel to the xy-plane of quantum well and \perp to the growth plane in z-direction as in Figure 2.7.

Valence band engineering incorporates strain to change the crystal lattice structure and will also have an effect on the band energy curvature as mentioned previously (Mogensen 1996). This can be shown in Figure 2.13 where a schema of the effect of strain on the parabolic band structure is drawn. The strain splits the valence bands as it changes the effective masses

in the xy -plane of the quantum well (parallel, \parallel) and in the growth direction z of the structure (perpendicular, \perp), causing the different curves of the valence band dispersion ratio (Coldren et al. 2012). Looking at the tensile strain, the highest lying valence band (1h), which forms the lowest energy gap with the conduction band, has a lighter effective mass in the perpendicular direction (growth direction) and a correspondingly heavier mass in the parallel direction (in the plane of the quantum well). The reverse is true for the compressive strain region. Next, we discuss the gain requirement for semiconductor lasers.

2.5 Gain requirement

This section is based on the approach of Blood (1991) to the semiconductor laser gain requirement. In III-V semiconductors, population inversion can be achieved directly by injecting a high density of carriers (electrons and holes) in the region close to the active region.

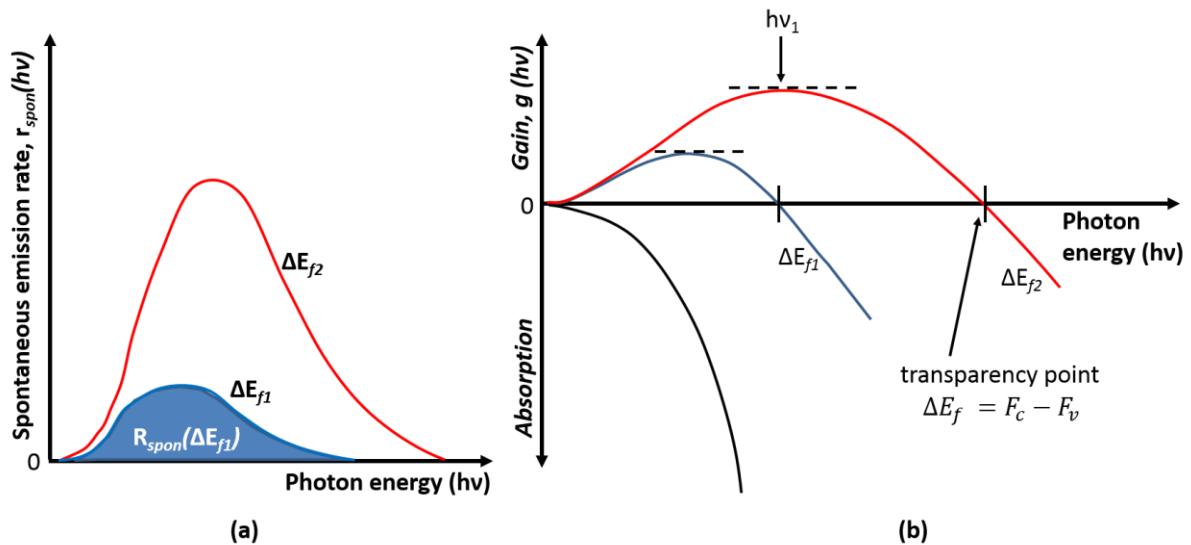


Figure 2.14: (a) Spontaneous emission spectra and (b) absorption/gain spectra (inverted for the use in this study) for a semiconductor pumped to two different quasi-Fermi level separations ΔE_{f1} and ΔE_{f2} , adapted from Blood (1991, p.235).

In calculating the optical characteristics of a semiconductor under high carrier density conditions, we must consider all allowed radiative transitions between occupied electron and

holes states within the respective density of states distributions, $N_c(E)$ and $N_h(E)$, where the occupancy is specified by the respective quasi-Fermi levels $F_c(E)$ and $F_v(E)$ as illustrated in Figure 2.4(c). The spontaneous and stimulated emission rates are both obtained at a photon energy $h\nu$, which leads to (a) the spontaneous emission rate spectra and (b) absorption/gain spectra for a semiconductor laser pumped to two different quasi-Fermi level separations, $\Delta E_f = \Delta E_{fe} - \Delta E_{fh}$ as shown in Figure 2.14. Figure 2.14(a) shows that as the ΔE_f is increased from ΔE_{f1} to ΔE_{f2} , the bands are filled with more carriers and this is accompanied by the expansion of the $r_{spont}(h\nu)$ spectrum on the high energy side (Blood 1991). As ΔE_f is increased as shown in Figure 2.14(b), gain is available over a wider range of photon energies. The crossing point between gain and absorption occurring is considered the transparency point as shown in Figure 2.14(b). The condition for laser action is that the gain provided by the medium should be high enough to overcome the scattering losses at the mirror (α_m) and optical mode loss (α_i) as mentioned in the previous Section 2.3.5. This occurs at ΔE_{f1} , where the stimulated emission and stimulated absorption rate are equal, such that g_{peak} satisfies this condition. A condition called the transparency occurs when, $\Delta E_f = F_c - F_v = E_{c1} - E_{v1}$ (Figure 2.10). This transparency condition can be used to explain the condition for laser action as shown in 2.14(b). Therefore, for a semiconductor laser of certain cavity length (L_C) and reflectivity (R), by pumping the cavity with a high enough current density to the quasi-Fermi level separation ΔE_{f1} , which implies that the gain provided by the medium should be more than sufficient to overcome the internal scattering loss (α_i) and the mirrors loss ($\frac{1}{L} \ln(R^{-1})$), based on equation 2.14, we can write, for gain at ΔE_{f1} , $G_{peak}(\Delta E_{f1})$, we have

$$G_{peak}(\Delta E_{f1}) < \left\{ \alpha_i + \frac{1}{L} \ln(R^{-1}) \right\} \quad (2.16)$$

Thus, for the gain peak at threshold that corresponds to the gain peak of the semiconductor laser, where $\Delta E_{f1} < \Delta E_{fth}$ and $\Delta E_{f2} = \Delta E_{fth}$, we can write the equation 2.16 as

$$G_{th} = G_{peak}(\Delta E_{f2}) = \left\{ \alpha_i + \frac{1}{L} \ln(R^{-1}) \right\} \quad (2.17)$$

where G_{th} is the peak modal gain occurring at ΔE_{f2} .

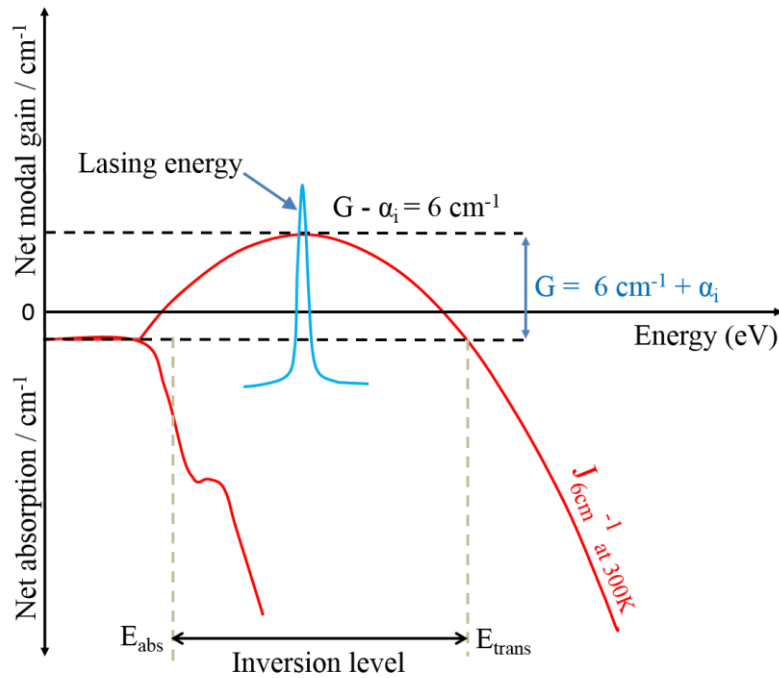


Figure 2.15: Schema of absorption and gain spectra for a 2-mm-long laser taken at 300 K. Inversion level is the difference between the quasi-Fermi level separation (transparency energy (E_{trans})) with the transition energy (E_{Abs}), adapted from Snowton et al (2001, p.1344). Lasing energy of a 2-mm-long laser occurs at the peak net modal gain is added for clarity, Snowton and Blood (2010, p.26).

When this condition is met, the photon density builds up, the threshold gain (G_{th}) can be defined as the difference between the rate of stimulated emission and absorption as in equation 2.4, thus photon-induced stimulated emission rate becomes the dominant recombination process at higher injection levels (Blood 1991). As indicated also in Figure 2.14(b), the peak net modal gain at $h\nu_1$ occurs at the lasing energy of the laser (Snowton and Blood 2010). To understand this further, let us look at the illustration in Figure 2.15 that shows the absorption and gain spectra for a 2-mm-long laser.

In this example, for a 2-mm-long semiconductor laser at 300 K, the threshold condition occurs with peak net modal gain, $G - \alpha_i = 6 \text{ cm}^{-1}$ as illustrated in Figure 2.15. The difference

between quasi-Fermi level separations, ΔE_f at transparency energy (E_{trans}) with the transition energy (E_{Abs}) is defined as inversion level (Smowton 2011). In this example, the lasing energy of a 2-mm-long-laser and the current density to achieve peak net modal of 6 cm^{-1} for this 2-mm-long laser should occur at the same peak energy at 300K (Smowton and Blood 2010).

2.6 Non-radiative recombination and thermal activated leakage

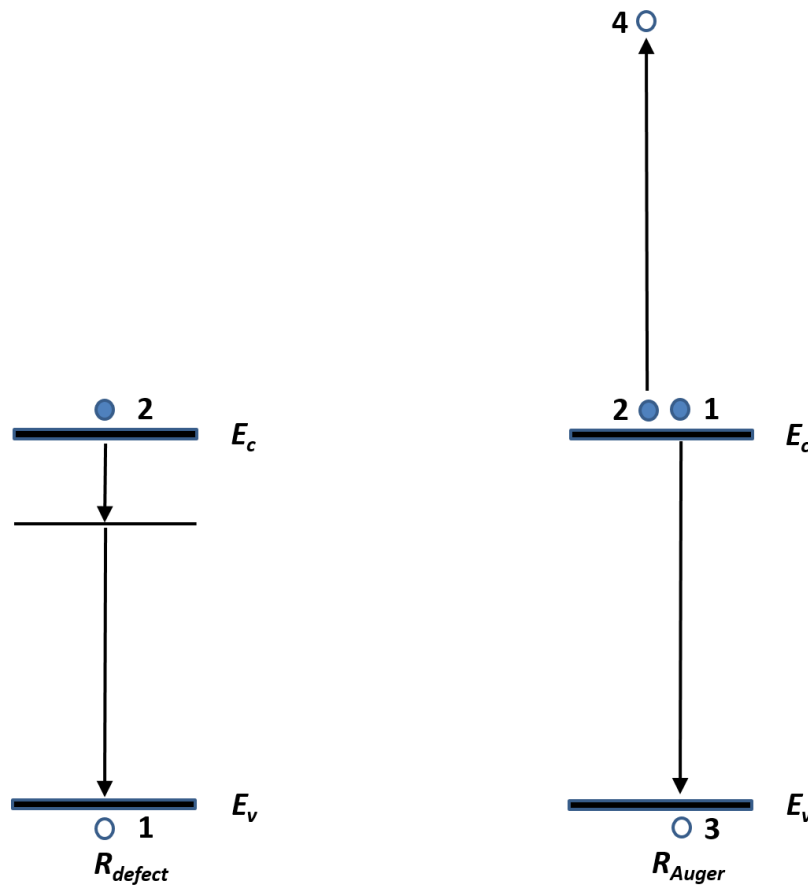


Figure 2.16: Schema of non-radiative recombination processes for impurity recombination (R_{defect}) and Auger recombination (R_{Auger}), adapted from Coldren et al (2012, p.158).

Non-radiative recombination takes place when the carriers in the conduction and valence bands recombine non-radiatively, this means no light will be emitted from this process. This will increase the current needed to achieve lasing. The measurements of the non-radiative recombination cannot be done with a direct method because photons are not emitted. They can

be measured indirectly by different methods such as measuring the spontaneous emission spectra at different temperatures and comparing the rate of change with temperature with the rate of change of threshold current. In general, there are three types of non-radiative recombination, Auger recombination, recombination at defects (Coldren et al. 2012) and thermally activated leakage (Wood et al. 1999; Coldren et al. 2012). In Auger recombination processes as shown in Figure 2.16, the energy which is released from the electron-hole recombination is absorbed by another electron and this electron is excited to a higher energy state. The excited electron loses energy in order to reach thermal equilibrium. The lost energy will be transferred into phonon or lattice vibrations. However, recombination at a defect is due to the capture of carriers at states, created by localized defects, at which the carriers then recombine non-radiatively. Essentially, phonon emission becomes more likely given the smaller energy steps and localised nature of the defect.

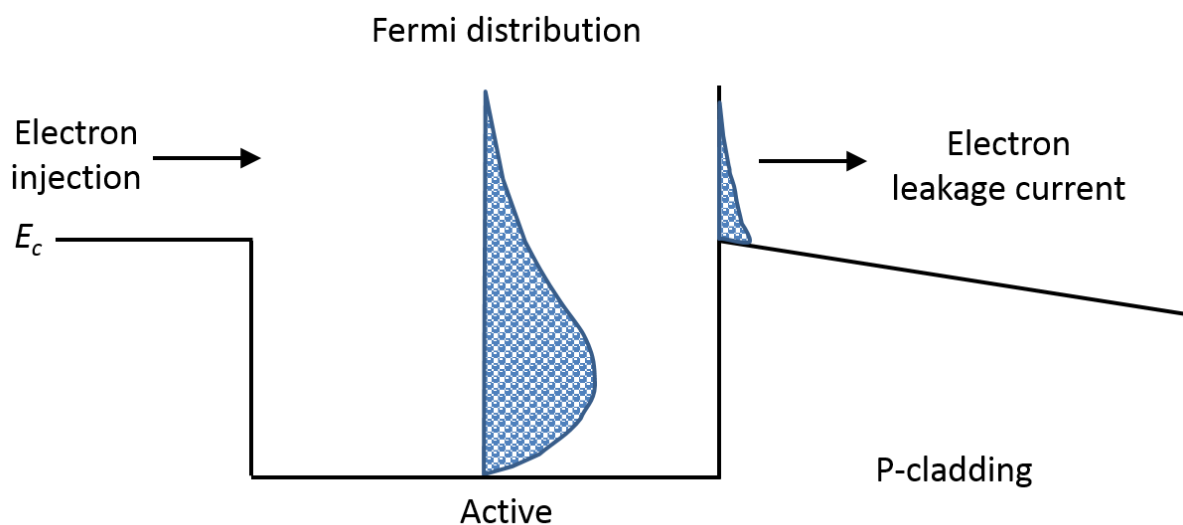


Figure 2.17: Schema of the conduction band edge of a double heterostructure showing electron energy distribution in the active layer and leakage current, adapted from Coldren et al (2012, p.539).

Thermally activated leakage can be understood by considering Figure 2.17. According to Coldren et al (2012) double heterostructures, such as shown in Figure 2.17, are not effective for energies greater than the band offsets between the active and the cladding layers. Carriers

are free to diffuse into the cladding areas once carriers have energy equal or greater to the top of the barrier. At room temperature for instance, the carriers in the high-energy tail of the Fermi-Dirac distribution will extend above the barriers. In practice this will cause carrier leakage out of the active region and at increased temperatures, an increasing fraction of high-energy carriers will have energies in this high energy tail and carrier leakage current associated with it will increase. Some of these high-energy carriers will escape the active region and diffuse into the p-cladding material as illustrated in Figure 2.17.

This is supported by a study by Wood et al (1999) observing the emission from a specially made layer of direct-gap material placed between the p-contact layer and the p-cladding layer of a conventional 670 nm GaInP laser diode at room temperature. They found direct evidence of electron leakage through the p-cladding layer which continued to rise above threshold although Fermi levels were clamped throughout the active region.

2.7 Self-Assembled Quantum Dots

According to Bhattacharya and Mi (2007) self-organized quantum dots have materialised as useful nanostructures that can be epitaxially grown and incorporated in the active region of devices. Self-organised quantum dots are considered the best approach in developing quantum dot devices (Leonard et al. 1993; Madhukar 1994). Bhattacharya and Mi (2007) reported that the use of strain to produce self-organised quantum dot structures has become a well-accepted approach and is widely used in III-V semiconductor devices. They also reported that highly lattice-mismatched Ga(In)As grown on GaAs in the Stranski-Krastanov growth mode (Stranski and Krastanov 1938, cited in Bhattacharya and Mi 2007), formed self-organised islands after a few monolayers growth. Bhattacharya and Mi (2007) reported that for typical growth parameters in the molecular beam epitaxy (MBE) or metal organic vapour phase epitaxy (MOVPE) growth techniques, a selection of near-pyramidal

islands of lateral size about 10 – 40 nm and height of 5 – 8 nm are formed. These growth techniques have the ability to grow a strained layer of semiconductor material on top of another one (Leonard et al. 1993; Madhukar 1994; Grundmann et al. 1996; Zundel et al. 1998). The top semiconductor layer starts to buckle due to the stress of having the lattice constant slightly different in size between the top and the bottom semiconductor materials (Mowbray et al. 2005). Figure 2.18 shows an image of uncapped InP quantum dots grown at temperature of 690°C on AlGaInP taken using Atomic Force Microscopy (AFM) (Smowton et al. 2005). This shows different dot sizes and the difficulty in controlling the sizes of the quantum dots will cause a variation in energy levels between the dots and result in spectral broadening of the gain spectrum.

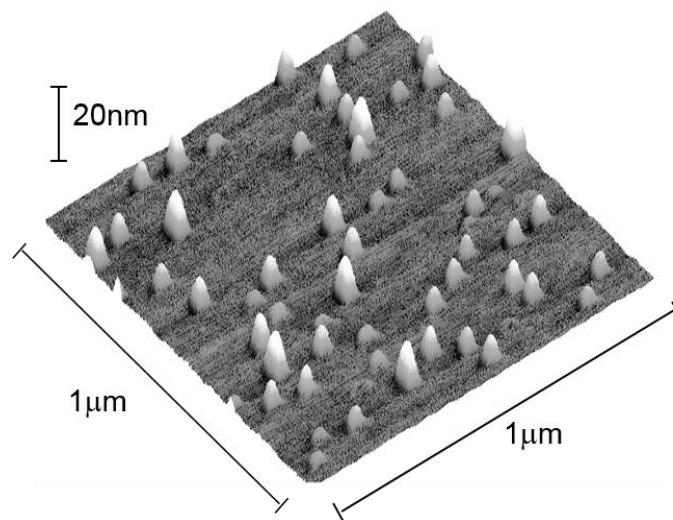


Figure 2.18: Atomic Force Microscopy on uncapped InP on GaAs material shows an occurrence of fluctuation in the growth of self-assemble quantum dots, reproduced from Smowton et al (2005, p.1036).

Broadening mechanisms are classified into two types, inhomogeneous and homogeneous broadening as represented in Figure 2.19. If all of the collection of quantum dots have the same transition energies and lineshapes, the broadening is called homogeneous. Otherwise, in the situation of Figure 2.18, where not all of the quantum dots have the same

transition energy and lineshape, the broadening due to the averaging of these individual quantum dot transition energies is known as inhomogeneous broadening (Wilson and Hawkes, 1998). Inhomogeneous broadening will occur due to the different energy levels in different sized dots (Blood 2009) and this is represented in Figure 2.19.

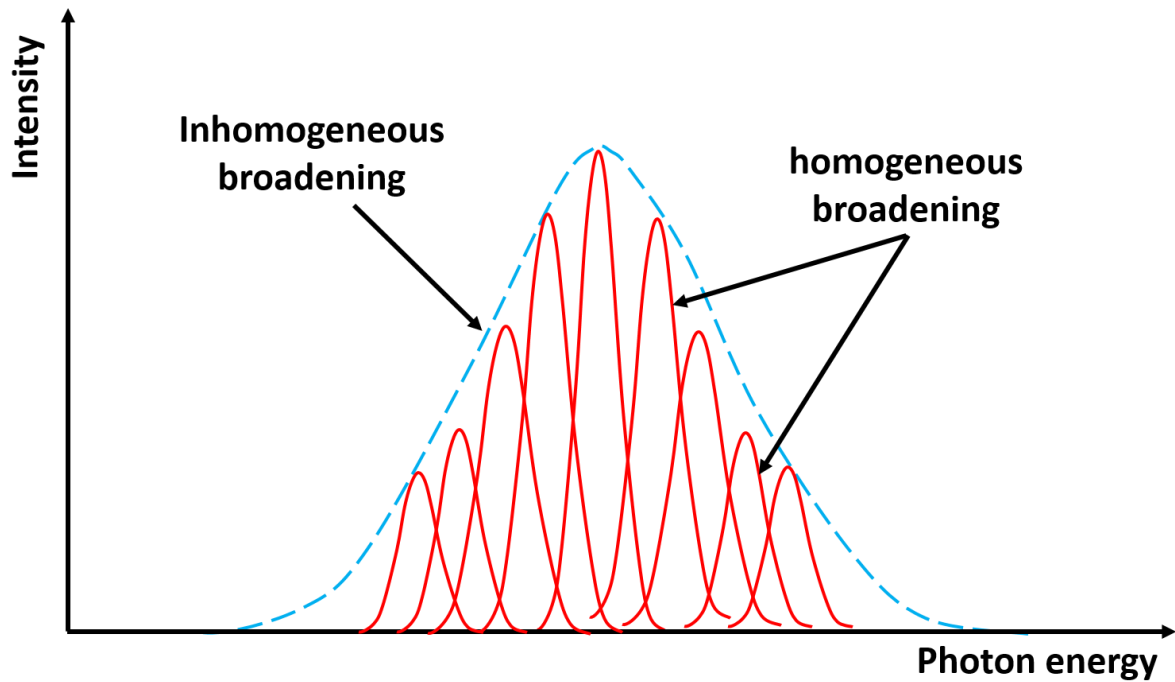


Figure 2.19: Illustration of the broadening in quantum dots for individual dots (red curve) and the overall dots ensemble (blue dashed curve), adapted from Blood (2009, p.811).

2.8 Carrier Distributions in Quantum Dots

The self-assembled quantum dots are separated from each other, therefore the carriers occupying an energy state in one dot cannot occupy an energy state in another dot. The dots in reality form with a distribution of sizes and compositions, therefore their energy levels and conduction band offsets differ (Blood 2009). This will cause an inhomogeneous broadening of the spectral emission as mentioned in the previous section. Riedl (1998) argued that at low temperatures the carriers are confined within the discrete levels of the quantum dots and a slight change in temperature does not significantly affect this situation due to the delta-like density

of states in the QD as mentioned in Section 2.3.4. He believes that towards higher temperatures, the carriers will be thermally excited into the wetting layer, where they recombine radiatively or not. To compensate, the current density has to be increased to reach the threshold carrier density in the dots. Next, we look into the temperature-dependence of threshold current.

2.9 Origin of temperature dependent threshold current

In most applications of a semiconductor laser the ability to deal with elevated temperature is quite important. The device should operate normally even at high temperature. In order to measure the semiconductor laser sensitivity to temperature, we can use the characteristic temperature (T_0). A high value of characteristic temperature means that threshold current density of the device increase less rapidly with increasing temperature (Mobarhan 2014). In other words, the laser is more thermally stable while in operation. The equation (cited in Akahane et al. 2010) outlining the process of finding T_0 is described as

$$J_{th} = J_0 \exp\left(\frac{T}{T_0}\right) \quad (2.29)$$

Where J_0 is a constant. J_{th} is the threshold current density, which varies with temperature T , and T_0 is the characteristic temperature. However, T_0 is an empirical parameter that does not represent any physical process happening in the device.

Lasher and Stern in (1964) stated that the cause of the temperature dependence of threshold current is due to the decrease in the degeneracy of the electron and hole populations as the temperature is increased. They also mentioned that at higher temperatures, the carrier populations are distributed over larger energy ranges, giving larger amounts of spontaneous emission, requiring higher current density for the same degree of population inversion. Arakawa and Sakaki (1982) predicted that by confining the electrons in the active region using quantum dots will result in less threshold current temperature dependence compared to conventional lasers.

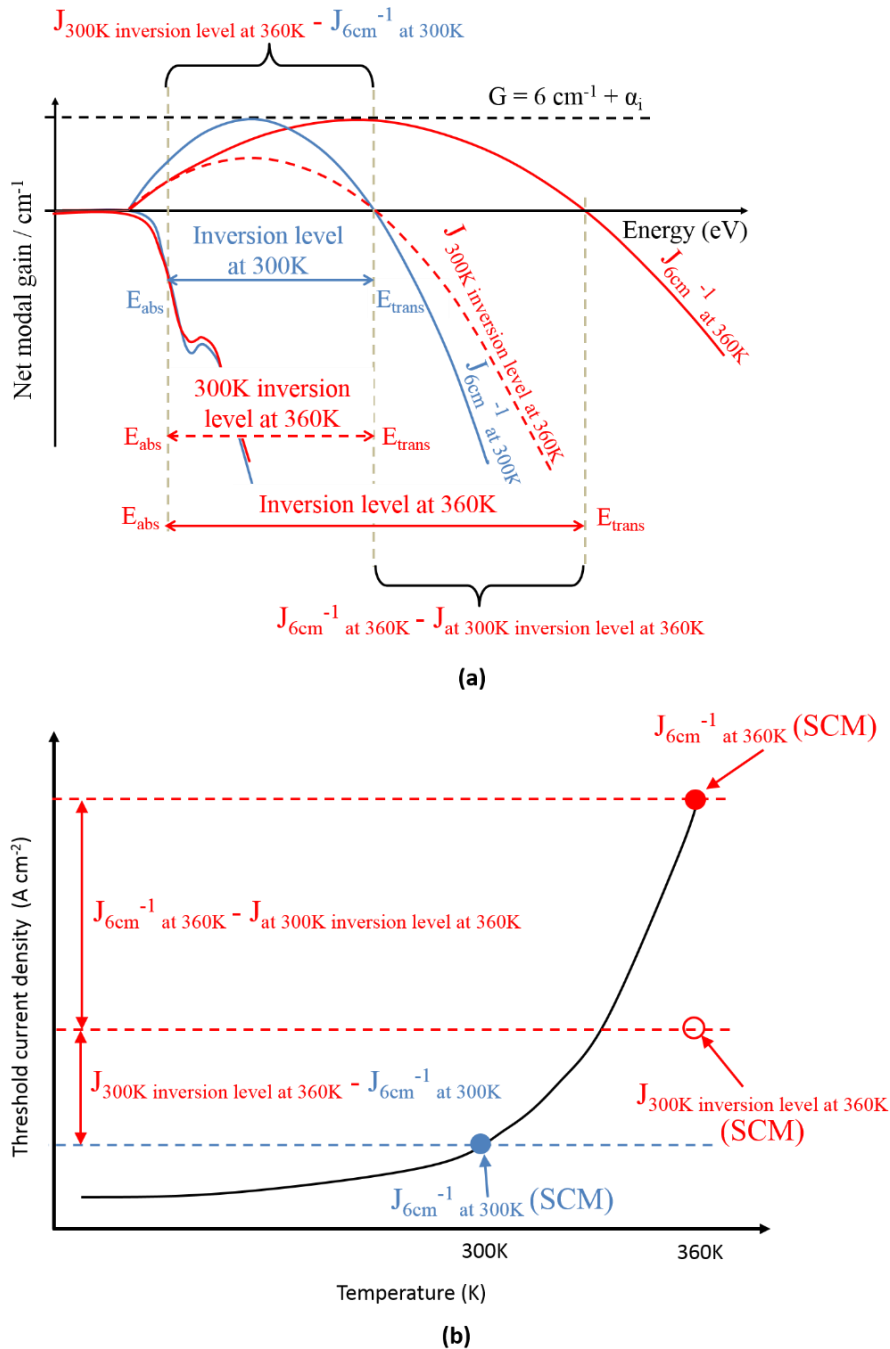


Figure 2.20: (a) Schema of the measured net modal gain spectra measured at a current density necessary to achieve a peak modal gain of $6 \text{ cm}^{-1} + \alpha_i$ solid (blue and red) curves at 300 K and 360 K, respectively. The red dashed curve represents the current density to achieve the inversion level of 300K at 360 K. The red curves at 360K were rigidly shifted by 26 meV to overlap the 300 K blue curves for comparison, adapted from Snowton et al (2011, p.1344). (b) Schema of the threshold current density as a function of current for a 2-mm long laser (black curve). The solid dots (blue and red) represent the current density to achieve peak net modal gain of 6 cm^{-1} for a 2-mm-long laser using the segmented contact method (SCM) experiment at 300 K and 360 K respectively. The open red dot represents the current density to achieve inversion level of 300K at 360K, adapted from Snowton et al (2011, 1345).

Since the initial report of a self-assembled quantum dot semiconductor laser significant progress has been made, with the best reported room temperature threshold current density of 10.4 Acm^{-2} (Deppe et al. 2009). However, even in the best performing structures, Smowton et al (2008) reported that the threshold current increases dramatically just above room temperature. They were able to make use of the segmented contact method (SCM), Blood et al (2003), to experimentally analyse the role of gain and the nonradiative recombination processes which are involved in the threshold current temperature dependence at elevated temperature as shown in Figure 2.20(a).

Smowton et al (2011) were able to separate out the effects of increasing inversion level from 300 K to 360 K and increased current density required to compensate for the increased carrier spreading at 360K using the SCM. Looking at the modified Figure 2.20(a) again, we can see that the inversion level or the difference between the quasi-Fermi level separation and the absorption edge energy (as described in Section 2.5) changes with the change with temperature. In the case of a 2-mm-long laser, a corresponding change in current density required to reach a peak net modal gain of 6 cm^{-1} as a function of temperature is seen, as indicated in Figure 2.20(b) at 300 K (blue dot). We start by taking the absorption and gain curves at 300 K (blue curves) and then at elevated temperature, in this case 360 K in Figure 2.20(a). As the electrons and holes are distributed over more states at elevated temperature, two scenarios will take place, either the peak gain decreases for a given carrier density ($J_{300\text{K}}$ inversion level at 360K – red dashed curve) or by keeping a constant peak gain as shown in Figure 2.20(a), a higher total carrier density is needed to achieve the same peak gain ($J_{6\text{cm}^{-1}}$ at 360K - red curve). The internal mode loss (α_i), does not change within the experimental uncertainty with temperature (Smowton et al. 2011). The schema of threshold current density as a function of temperature in Figure 2.20(b) shows the position of the related inversion levels with respect to Figure 2.21(a).

The current densities in both graphs, i.e. the current density used in the SCM that is necessary to achieve a peak modal gain of 6 cm^{-1} and the corresponding inversion level are in agreement as expected. The value of this SCM is that we can separate out the effect of the increased inversion level ($J_{6\text{cm}^{-1}} \text{ at } 360\text{K} - J_{300\text{K inversion level}}$) from the increased current density ($J_{300\text{K inversion level at } 360\text{K}} - J_{300\text{K inversion level at } 300\text{K}}$) due to the non-radiative recombination and carrier spreading (Smowton et al. 2011) as previously mentioned in Section 2.6.

Figure 2.20(a) shows a simple rigid shift of the 360 K gain and absorption spectra (red curves) to overlap the gain and absorption spectra of the 300 K (blue curves) of about 26 meV. The almost exact overlap of the shifted 360 K onto the 300 K absorption spectra, emphasises the rigid shift of the energy state of the system with the change in temperature (Smowton et al. 2011). Thus, to monitor the progress of the energy band gap at any temperature T , one can calculate the changes in absorption edge as a function of temperature by using an empirical equation (Varshni 1967) which applies to both direct and indirect band gap energies

$$E_g(T) = E_g(0) - \frac{\alpha T^2}{B+T} \quad (2.28)$$

where $E_g(T)$ is the energy gap at temperature T , $E_g(0)$ is the energy gap at $T = 0\text{K}$ and α and β are adjustable parameters. This Varshni equation (1967) will be used later in the coming chapters.

2.10 Summary

In this chapter, the general overview of the physical principles of semiconductor quantum dot lasers was discussed. It started with the introduction of the fundamentals of lasers such as emission and absorption, population inversion, the laser elements with optical feedback and threshold condition. We moved on to the description of some concepts of semiconductors including bandstructure, the Fermi-Dirac distribution, density of states, quantum confinement and optical gain. Next, the quantum well structure was described with unstrained and strained features, followed by the gain requirement. After that was the explanation of the recombination in semiconductor lasers, including modal gain, absorption, spontaneous emission and non-radiative recombination which included the thermally activated leakage. The quantum dot system of self-assembled formation and broadening of spectra was explained and followed by the carrier distributions in quantum dots. Lastly, the temperature dependence of threshold current was described and approaches to quantify contributions to this were also described. Next, I will explain the experimental procedures and structure design of this study in Chapter 3.

Chapter 3

Experimental Procedures and Structure Design

3.1 Introduction

In this chapter the device structures which were used for measurements in this thesis are described. First the materials structure and the wafer used in this study are introduced. Next, I will look into the device preparation to transform these structures into working laser or segmented contact devices. Illustrations are shown on how these devices can be mounted and tested, and which criteria are used to ensure they are suitable for the experiments.

Following this presentations of the experimental procedures and equipment used to obtain data for the following result chapters in this thesis are shown. These include experiments for measuring the threshold current and spontaneous emission spectra using laser devices, edge-photovoltage spectroscopy for transition energies, and optical gain and absorption using segmented contact devices. The way the data is treated to obtain the inversion level (or the difference between the quasi-Fermi level separations with the absorption edge) at different temperatures is also shown.

3.2 Device Structure and design

The device structures were designed by Prof. Peter M. Smowton in the School of Physics and Astronomy, Cardiff University. The designs were grown by Dr. Andrey B. Krysa in the EPSRC National Centre for III-V Technologies, The University of Sheffield. The structure consists of an active region of QWs and QDs and the growth method used was Metal Organic Chemical Vapour Deposition (MOCVD) or Metal Organic Vapour Phase Epitaxy (MOVPE) for arsenides and phosphides. MOCVD has been the leading procedure for the manufacturing of

semiconductor devices (EPSRC 2011). The samples are grown in an old reactor which does not rotate the substrate during growth.

3.2.1 Device materials

| Layer no. | Reps | Material | X | Thickness (nm) | T (°C) | Dopant type |
|---------------|------|---|-----------|-------------------|--------|----------------|
| Cap | 1 | GaAs | | 300 | 690 | P |
| intermediate | 1 | GaInP | | 100 | 690 | P |
| Barrier | 1 | (Al _(x) Ga _(1-x))InP | 0.3 | 100 | 690 | P |
| cladding | 1 | AlInP | | 900 | 690 | P |
| cladding | 1 | AlInP | | 100 | 690 | ud |
| Barrier | 1 | (Al _(x) Ga _(1-x))InP | 0.30 | 84 | 730 | ud |
| Barrier (LCL) | 5 | (Al _(x) Ga _(1-x))InP | 0.30 | 16 | 730 | ud |
| QW (UCL) | 5 | Ga _(x) In _(1-x) P | 0.52-0.58 | 8 | 730 | ud |
| QD | 5 | InP | | 0.78 | 730 | ud |
| Barrier | 1 | (Al _(x) Ga _(1-x))InP | 0.30 | 100 | 730 | ud |
| cladding | 1 | AlInP | | 1000 | 730 | n |
| intermediate | 1 | GaInP | | 200 | 710 | n |
| Buffer | 1 | GaAs | | 500 | 710 | n |

Table 3.1: Details of the structure Design.

In the standard device structure, the buffer and cap are made of n- and p-doped GaAs, respectively. The structure as shown in Table 3.1 was grown at temperatures of 690°C to 730°C. The waveguide core consists of an active region in between 100 nm thicknesses of (Al_{0.3}Ga_{0.7})_{0.52}In_{0.48}P. The QD structure in the active region is formed from 3 monolayers of InP quantum dots grown on a (Al_{0.3}Ga_{0.7})_{0.52}In_{0.48}P as the lower confining layer (LCL), covered

by 8 nm thick $\text{Ga}_x\text{In}_{(1-x)}\text{P}$ as the upper confinement layers (UCL) with $x = 0.52$ to $x = 0.58$ and separated by 16 nm thick $(\text{Al}_{0.3}\text{Ga}_{0.7})_{0.52}\text{In}_{0.48}\text{P}$ of the LCL, which are the barriers. These active region layers are repeated 5 times. The schema of the structure is shown in Figure 3.1. The cladding layers consist of a 1000 nm thick $\text{Al}_{0.52}\text{In}_{0.48}\text{P}$ on the top layer which is p-doped, and a 1000 nm thick $\text{Al}_{0.52}\text{In}_{0.48}\text{P}$ bottom layer which is n-doped. The two $\text{Ga}_x\text{In}_{(1-x)}\text{P}$ intermediate layers are grown to reduce the high difference in energy gaps between the cladding layer with the cap and the cladding layer with the buffer. The cap and buffer are formed to decrease the contact resistance of the ohmic contacts, which are added during device fabrication.

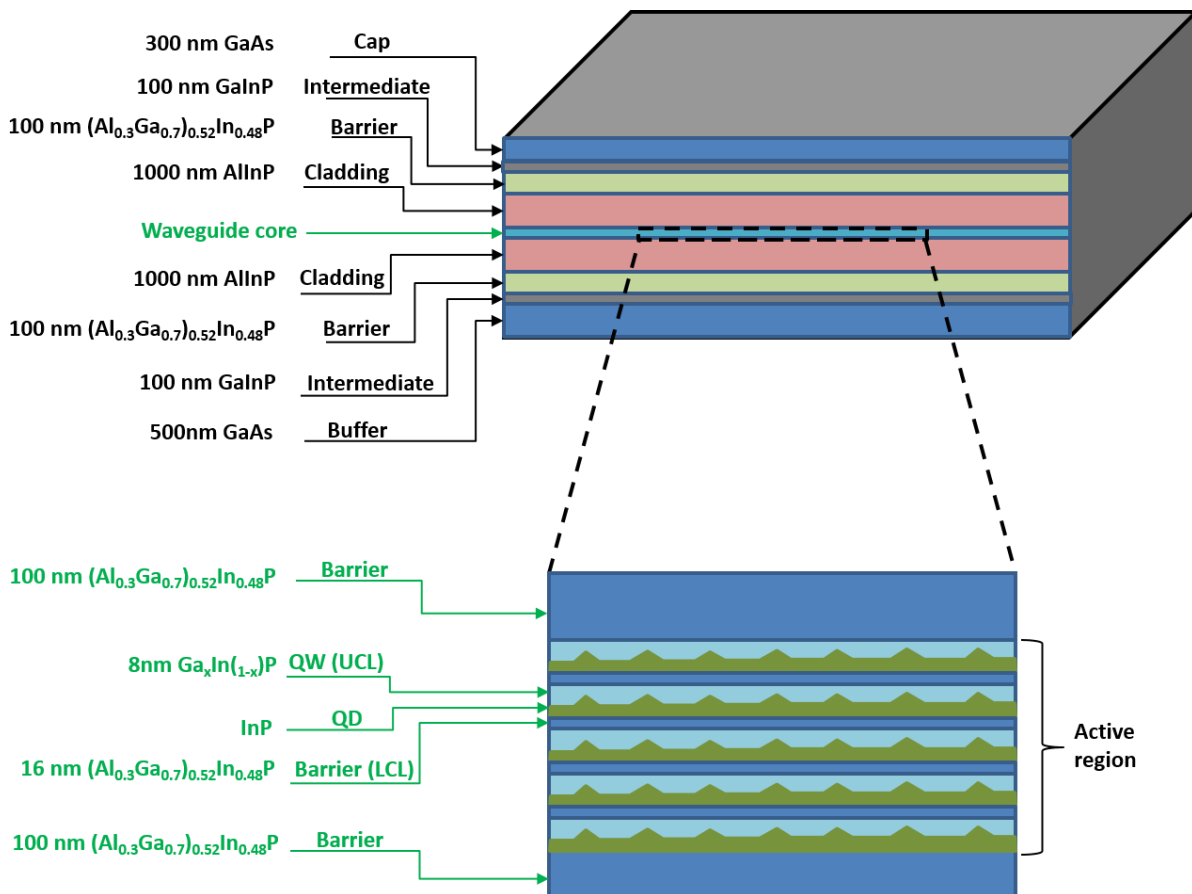


Figure 3.1: Schematic diagram of the structures with layers and thicknesses.

3.3. The wafer structure and photoluminescence

This section is divided into three parts. First part is the wafer structure, cut-section of devices and lastly the data given for photoluminescence (PL).

3.3.1. Wafer structure

The wafer disks were grown using the general orientation as described in Figure 3.2. The diagram shows the direction in which the material that is deposited as the wafer flows during growth. Only the main wafer with the major flat section was used in this experiment.

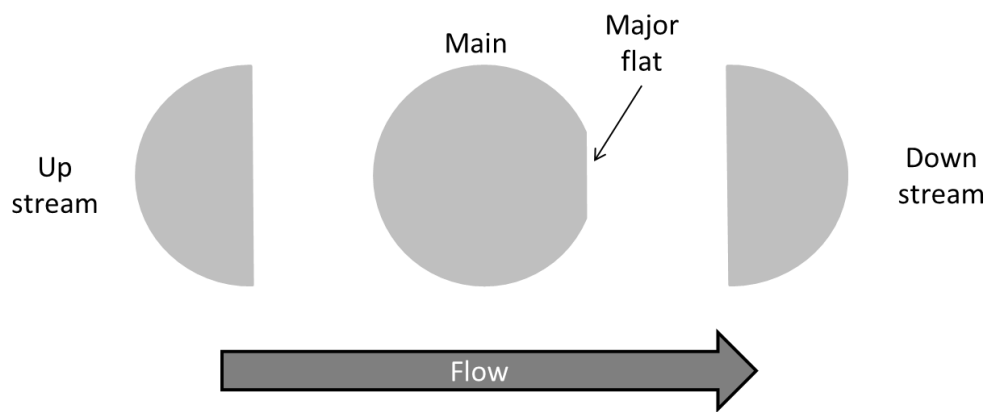


Figure 3.2: General orientation of either half-wafer or a full disc schema. The orientation of main wafer shows the major flat is down-stream with respect to flow (courtesy of Dr. A. B. Krysa).

3.3.2 The device sample selection on wafer

The grown samples are processed into laser and segmented contact test chips in the Cardiff University cleanroom by Karen Barnett. Each processing run uses only a part of the 2 inch diameter wafer to produce many chips of each type. The area selected was based on availability of material from each wafer (Figure 3.3). The distribution of the cut section based on laser or segmented contact should be close to each other. In theory, the laser and the segmented contact should be placed side by side perpendicular with respect to the growth flow, for example $Ga = 0.52$ on the RHS of the dotted line (or down-stream) of the wafer near the major flat, where we can see the laser and segmented contact pieces. A recent development in the cleanroom was processing the sections into half as laser and half as segmented contact and

this was done on the $Ga = 0.56$ as can be seen on the RHS of the dotted line (or down-stream) of the wafer near the major flat of Figure 3.3. We will return to this topic later on to explain the significance of it in Chapter 4.

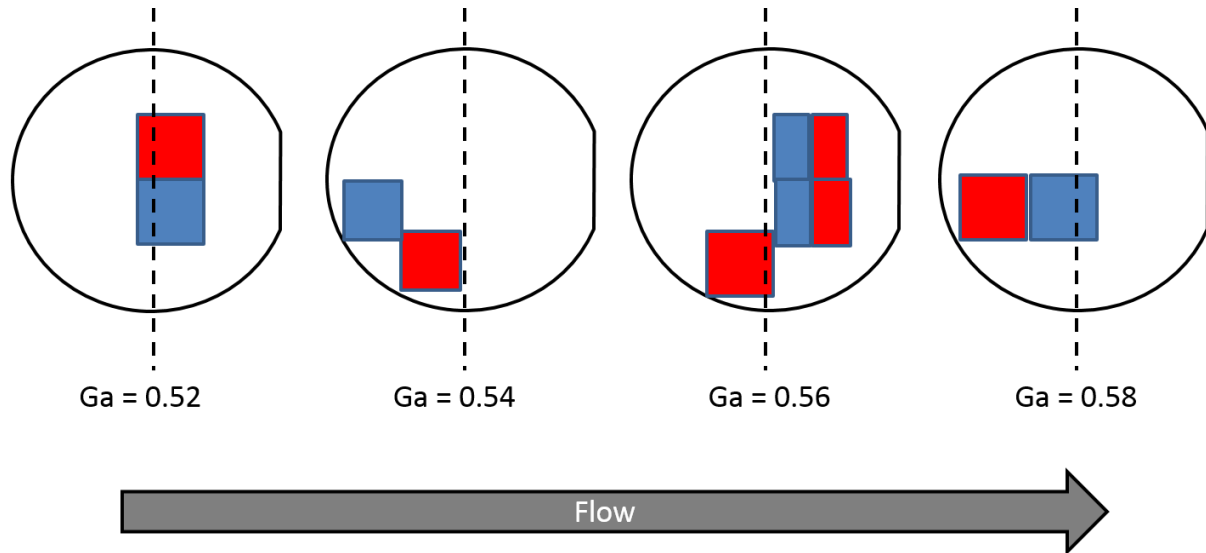


Figure 3.3: Schema of orientation of each gallium composition with respect to flow. The red box signifies the location of lasers and blue box segmented contact devices. On $Ga = 0.56$, a new technique using half and half for laser and segmented contact was developed.

3.3.3 Photoluminescence

The Photoluminescence data was obtained from the EPSRC National Centre for III-V Technologies. The PL technique uses laser-induced photoluminescence to produce wavelength spectra from different parts of the wafer either upstream, downstream or centre.

3.4 Computational modelling

The computational model software used was originally developed by Dr Berry (1996) and uses a transfer function method to calculate propagation constants and field profiles for multi-layer slab waveguides. Several modifications and inputs were made to generate near-field profiles. First, the optical waveguide mode is solved for by inserting input parameters such as thickness and refractive indices of layers. By using the transfer function method to

solve Maxwell's equations, the near-field intensity as a function of distance across the layers as well as the confinement factor Γ , in each layer can be calculated. The software optical mode solver also calculates the far-field from the calculated near-field amplitude using a Fourier transformation (Berry 1996). The reflectivity value (R) defined as the fraction of the incident intensity reflected by the mirror as mentioned in equation 2.5 in Chapter 2 is calculated by inserting the refractive index values found in the calculation. The reflectivity value is used in finding the net peak modal gain ($G - \alpha_i$) of any length of laser. Next I will describe the experimental techniques used in this study.

3.5 Experimental techniques

The experiments described in this thesis make use of the oxide isolated stripe devices. The mounting and handling of devices, measurement of current, voltage, light and temperature characteristics (IVLT), near-field measurement, spectrum analyser measurement of lasing wavelength, absorption edge-photovoltage spectroscopy (EPVS) measurement, obtaining absorption and gain spectra using spectrometer and difference between quasi-Fermi level separation energy with band edge energy or inversion level will be described in the following sections.

3.5.1 Mounting and handling of devices

The separate oxide isolated stripe laser devices were prepared and cleaved in the clean room by technical staff. There were two different devices processed for this study, a laser device and a segmented contact device as shown in Figure 3.4. The laser devices were 300 μm in width and in lengths of 1000 – 4000 μm . The oxide isolated stripe itself is 50 μm wide. The segmented contact device was divided into 7 or more equal sections with a width of 300 μm ,

each section is 300 μm long with a 4 μm micro-channel in between section. Careful selection of devices was carried out prior to the measurement.

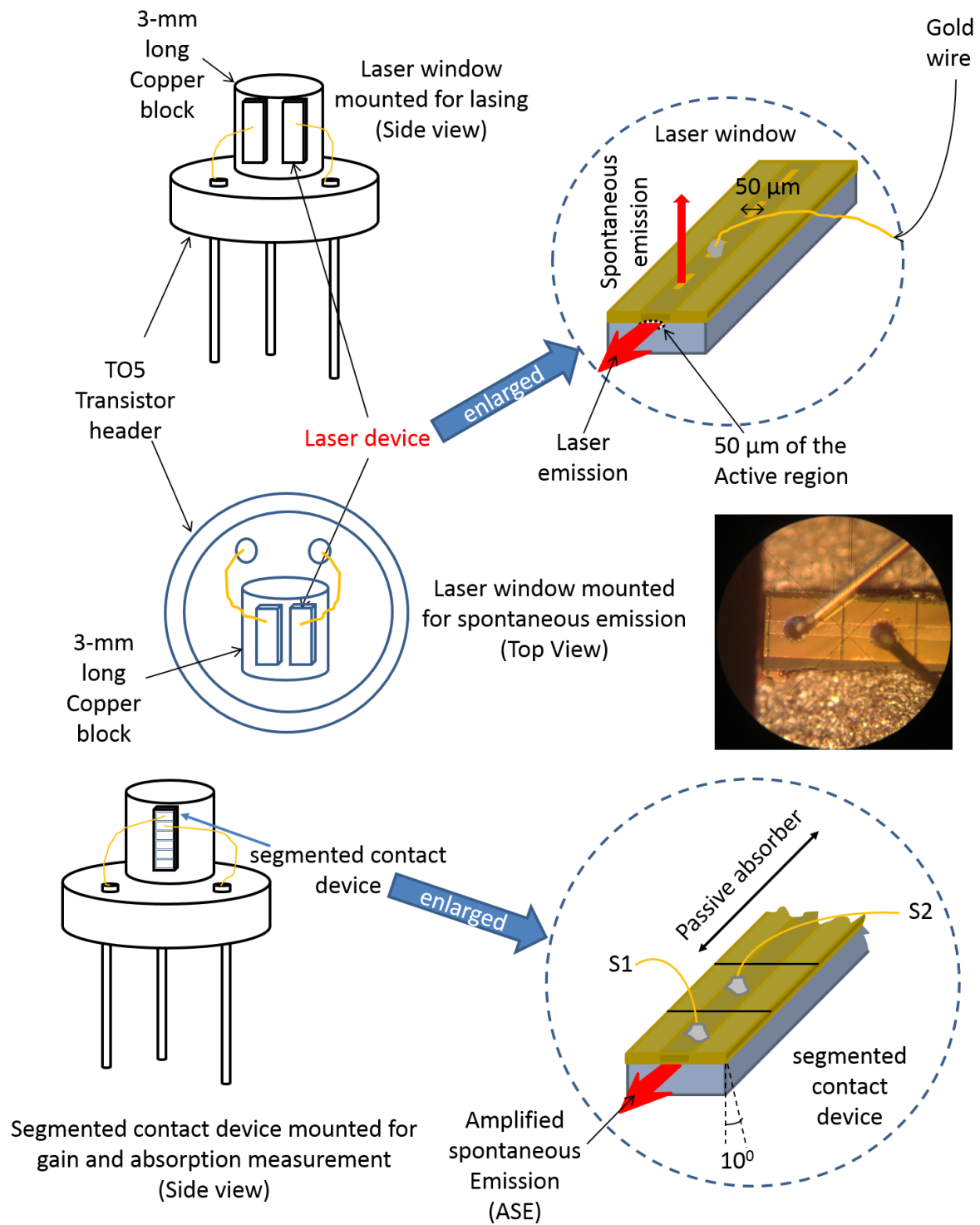


Figure 3.4: Diagram of two devices mounted on a transistor header. The enlarged part of the active region is shown as an illustration.

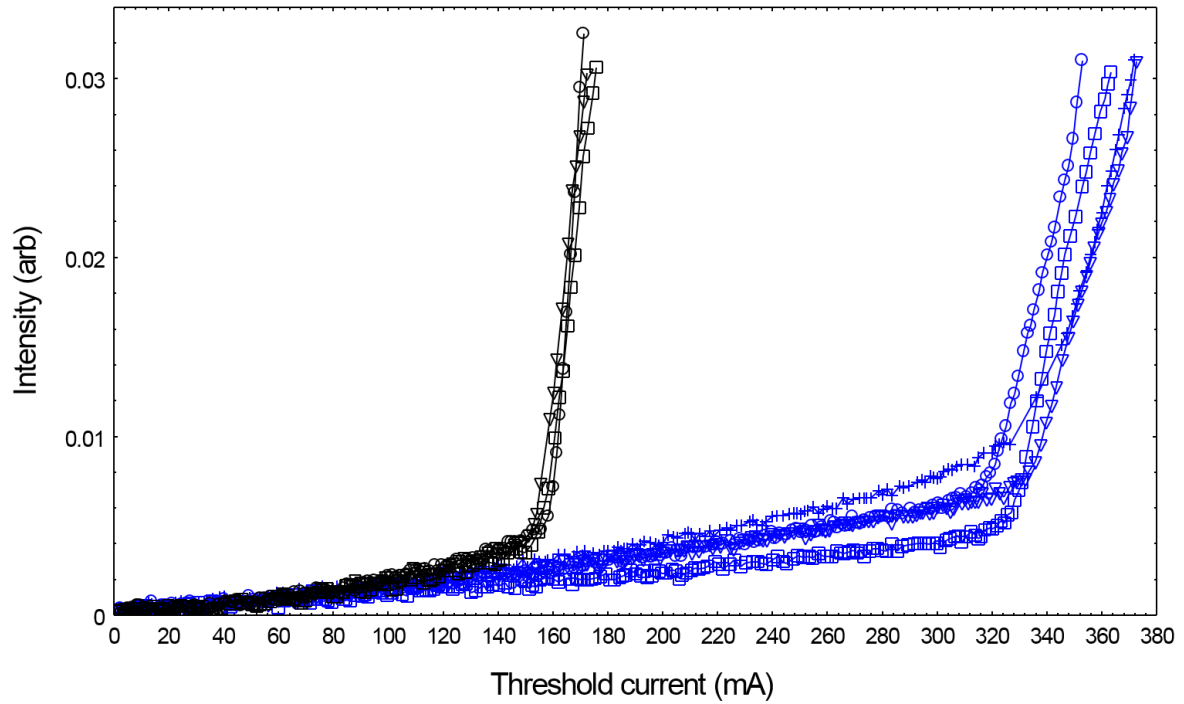


Figure 3.5: Intensity as a function of threshold current for $Ga = 0.52$ (blue curves) and $Ga = 0.56$ (black curves).

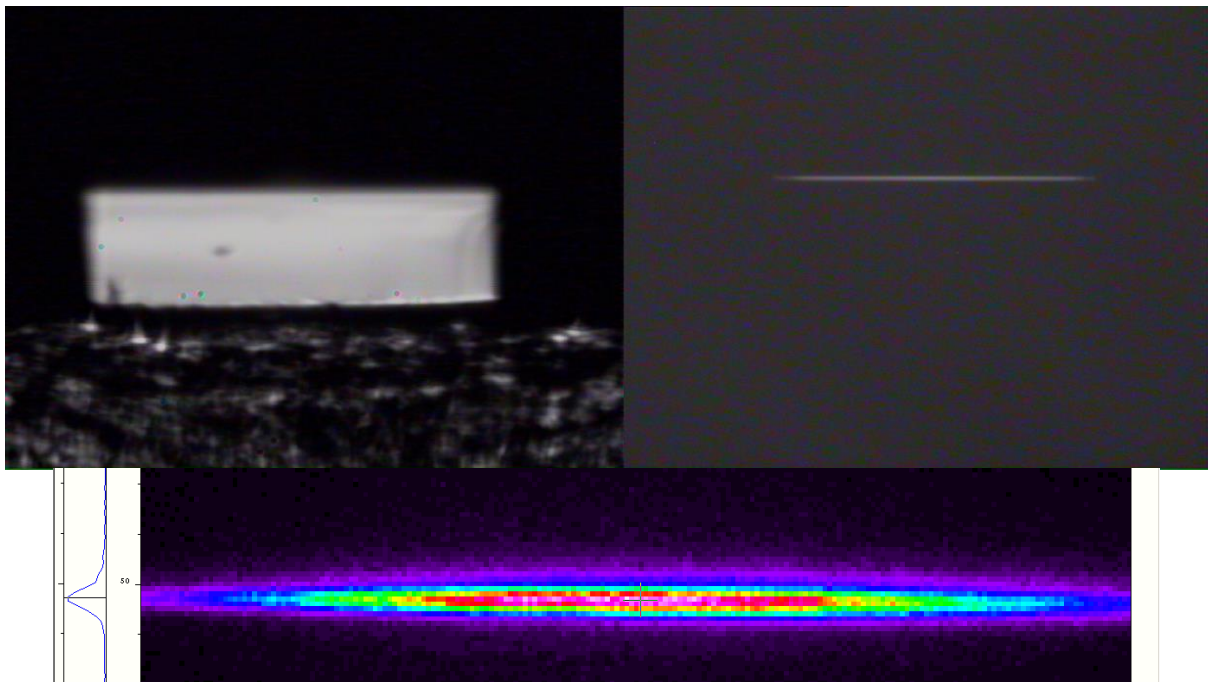


Figure 3.6: The left picture shows an example of an illuminated facet, on the right shows the ASE from the device and the picture below shows the image captured using the ICCD camera.

Samples are checked to ensure that all the device facets are clean and damage free on both sides of the facets especially around the 50 μm stripe region of the facet. The device was then mounted on the 3 mm copper block which had been attached earlier to a T05 transistor header as shown in Figure 3.4. All the parts including the gold wire were attached using metal containing conductive epoxy which was heated at 175°C for at least 45 seconds to harden it. In general, the requirements for laser devices are as follows:

- at least 2 good devices for comparison with consistent results as in Figure 3.5,
- clean, undamaged reflective facet as in Figure 3.6,
- and near-field taken using neutral density filter and spectral filter (670 nm) to ensure only the ASE wavelength is allowed to pass through, not the lasing wavelength,

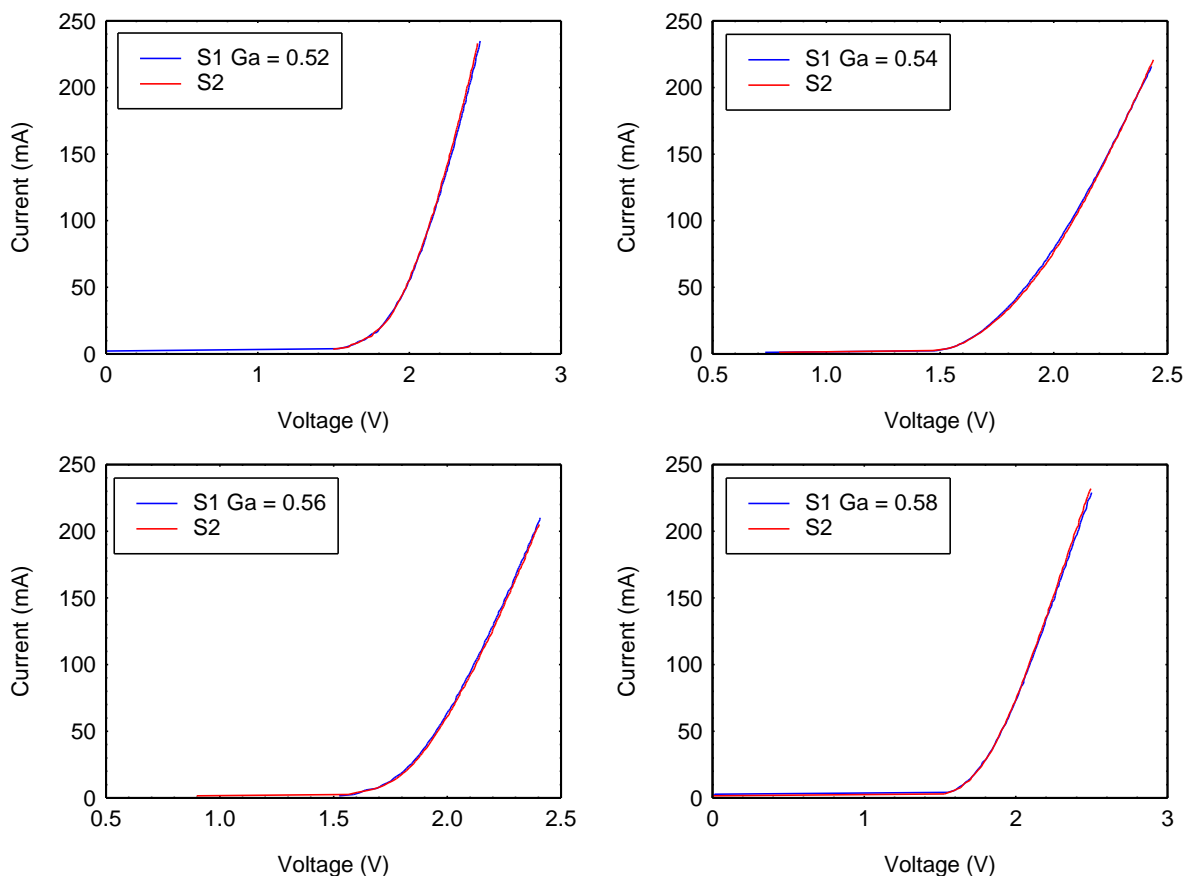


Figure 3.7: Matching current and voltage characteristics of Section 1 and 2, <5% difference between Section 1 and 2 for all the Ga compositions in the UCL.

For segmented contact devices:

- matching current and voltage characteristics of Section 1 (S1) and Section 2 (S2), an acceptable sample was defined as having $< 5\%$ difference in voltage between S1 and S2, examples shown in Figure 3.7,
- clean, undamaged reflective facet,
- little or no evidence of filamentation in the ASE,
- the lasing energy of a 2-mm-long-laser and the current density to achieve peak net modal gain of 6 cm^{-1} for this 2-mm-long laser should occur at the same peak energy as mentioned in Section 2.5 in Section 2,
- and near-field taken using the neutral density filter and the spectral filter (670 nm) same as the laser device measurement,

which will determine the success of the whole measurement. Other examples of these requirements will be shown in each device section as we move on.

3.6 Current voltage light temperature characteristics.

Measurements of the threshold current density are made using the experimental setup for the current-voltage-light-temperature (IVLT) measurement as shown in figure 3.8. The mounted laser devices were placed inside the vacuum chamber with the emission directed through a neutral density filter window. The neutral density filter is used to ensure the linear region of the photodiode detector used in this setup is not exceeded and also to reduce any background noise. The photodiode detector used to detect any emission from the device is placed above this window, which fits exactly in order to block any outside light from entering the window. Before attempting any measurement on the current-voltage-light-temperature kit, the boxcar integrator must be set to a pulsed signal of 1000 ns with a repeated frequency of 1 kHz from the pulse generator through the current controller.

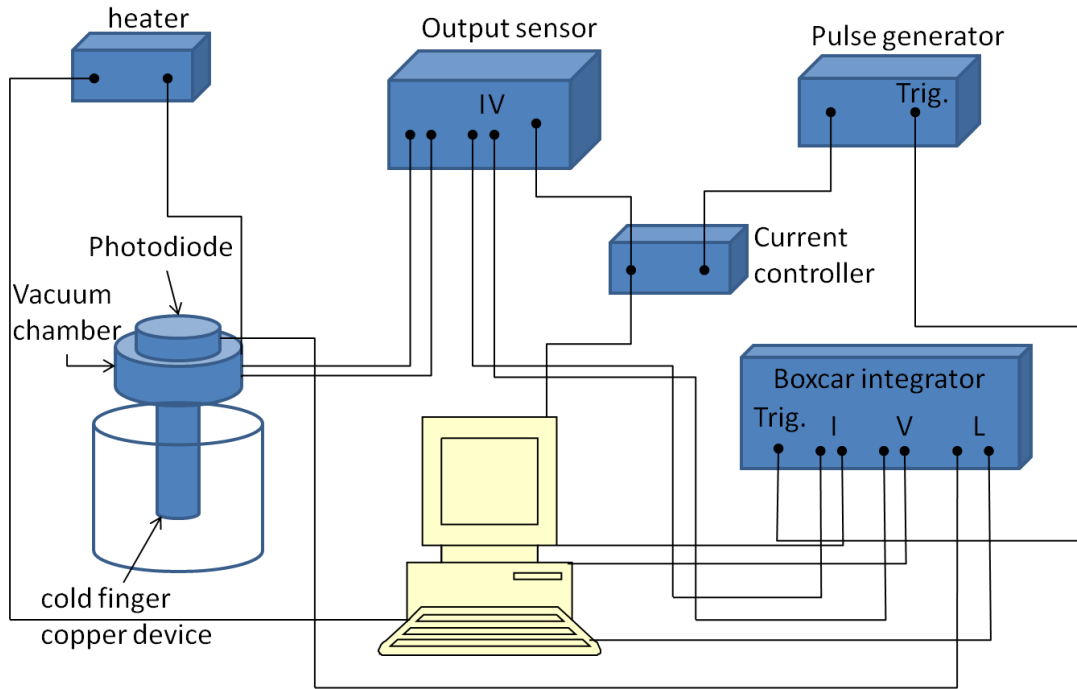
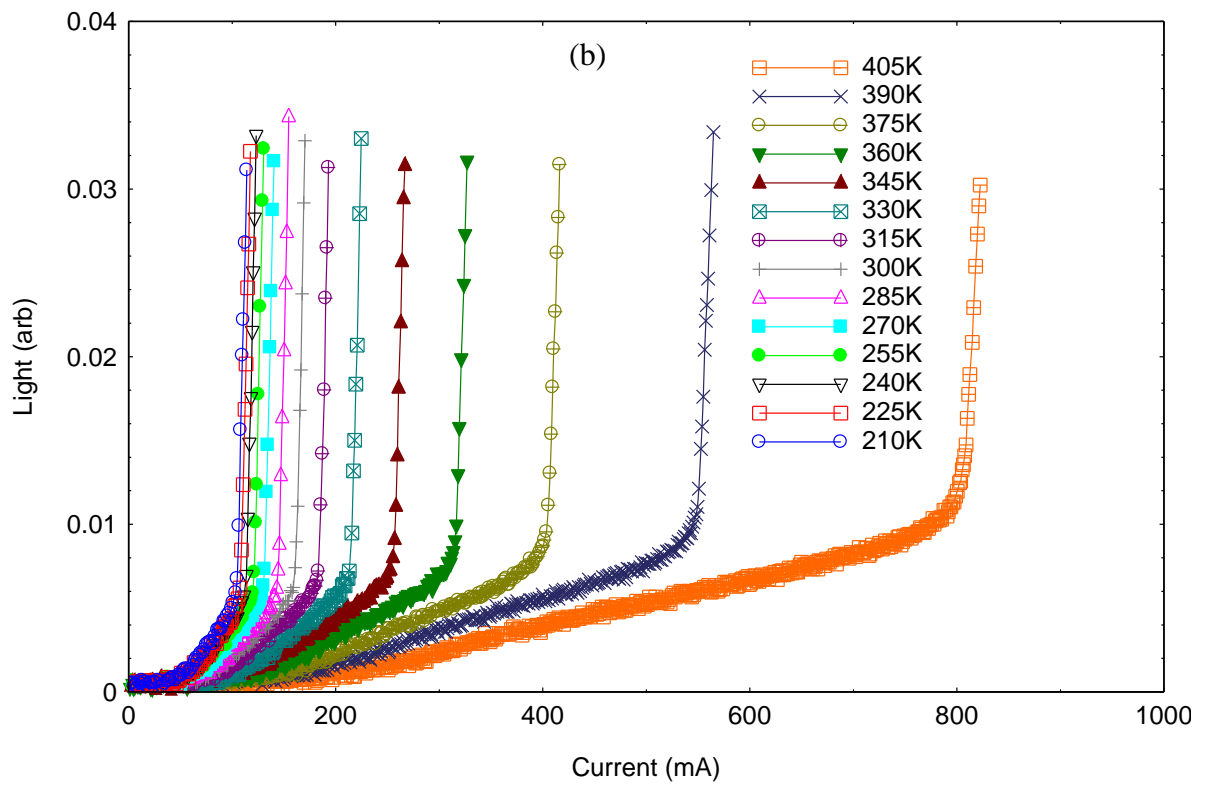
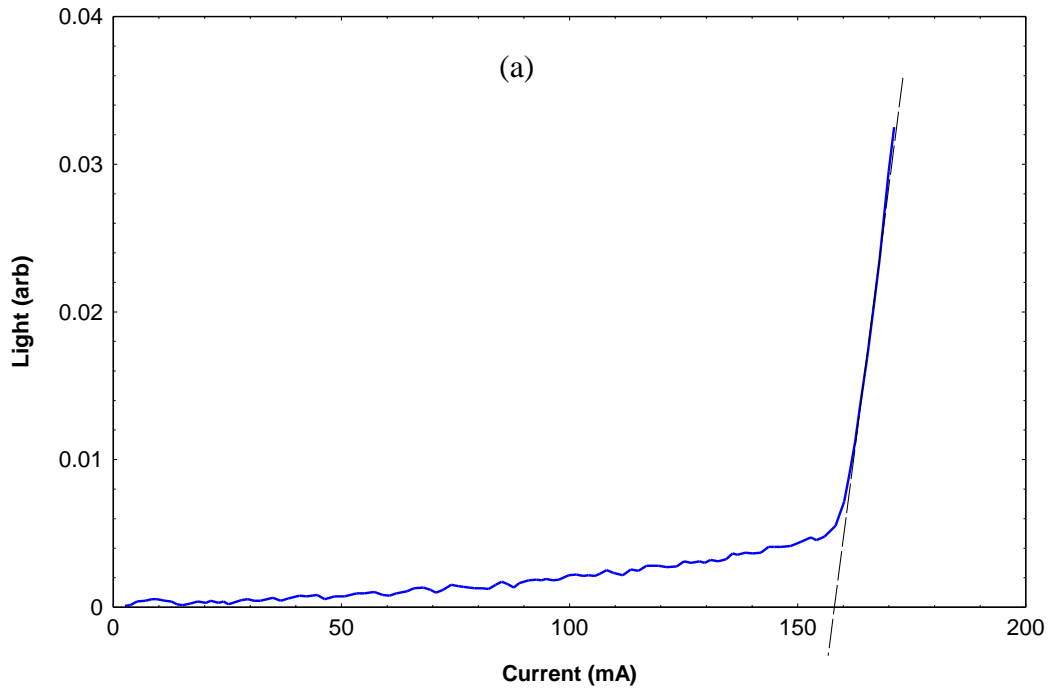


Figure 3.8: The Current voltage light and temperature (IVLT) measurements kit schema.

This pulsed mode is set to avoid any heating effects on the device during measurements. All the gates from the voltage, current and light output of the boxcar were aligned within a stable signal coming from the pulsed device on the CRO display.

The program from the IVLT kit (Griffiths 1992) can be used for several measurements such as finding the light-current and current-voltage characteristics curves at room temperature or in a temperature run. In this case it was the measurement of the devices at a varied temperature ranging from 140 – 400 K. Liquid nitrogen was used to lower the temperature. In the vacuum chamber, the laser devices were placed on an apparatus made of copper called the Cold Finger. The extended part of the Cold Finger, which is outside of the vacuum chamber was directly dipped into the liquid nitrogen. Once the temperature reached below the 140 K, the container of nitrogen liquid was emptied into the cold trap of the pump to stop any oil coming into the vacuum chamber. The emission of light was taken every 15 K until it reached 400 K. The temperature was taken at 5 K interval between each laser devices.



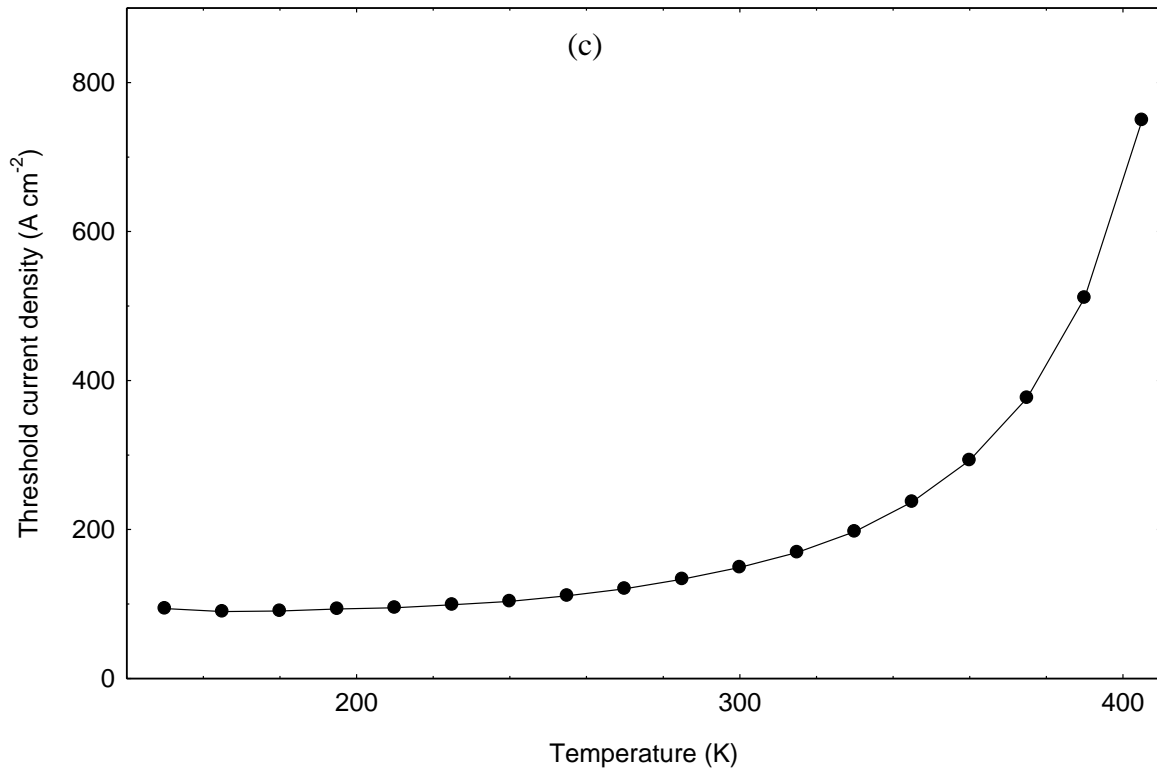


Figure 3.9: (a) Ga = 0.56 composition laser device of length 2000 μm taken at 300 K with $I_{\text{th}} = 157$ mA used as an example. (b) Ga = 0.56 composition laser device of length 2000 μm taken at different temperatures. (c) Threshold current density as a function of temperature for 2-mm-long laser (Ga = 0.56).

Once the temperature was reached for each step, the program will run until 0.03 arbitrary light units which was the cut-off value of the QD laser device. This specific light limit is set to ensure the linearity of the photodiode detector is not breached and also not to overheat the device. Within this period of about 6 seconds the program will take the I-V and L-I characteristics curves of the lasing device. The program saved the interval of temperature runs in two separate files for each device. An example of an L-I characteristics is shown in Figure 3.9(a). The Figure 3.9(a) shows the measured light intensity of the Ga = 0.56 laser device as a function of current input or injection current for a 2-mm-long laser device at 300 K. The horizontal part of the curve which is at low light intensity is due to spontaneous emission.

Once the optical gain in the laser medium matches the optical losses, the lasing starts to occur which is shown by the abrupt increase of the light intensity. By extrapolating the linear part of the curve beyond the threshold point backwards with a straight line, a point will intersect with the x-axis of the graph and this point is called the threshold current, I_{th} as shown in Figure 3.9(a). The value of the threshold current is 157 mA for this device at the temperature of 300 K. This procedure can be applied for threshold current as a function of temperature as shown in Figure 3.9(b). A better representation of the underlying properties is by finding the threshold current density of this device which is the threshold current per unit area (Wilson and Hawkes 1987)

$$J_{th} = \frac{I_{th}}{A} \quad (3.1)$$

The area A is the product of the device length and the pumped stripe width. The device length and total width of the facet can be measured under the travelling microscope. The measurement of the pumped stripe width can be explained later in the near-field section. Figure 3.9(c) shows a representation of threshold current density as a function of temperature.

3.7 Near-field measurement

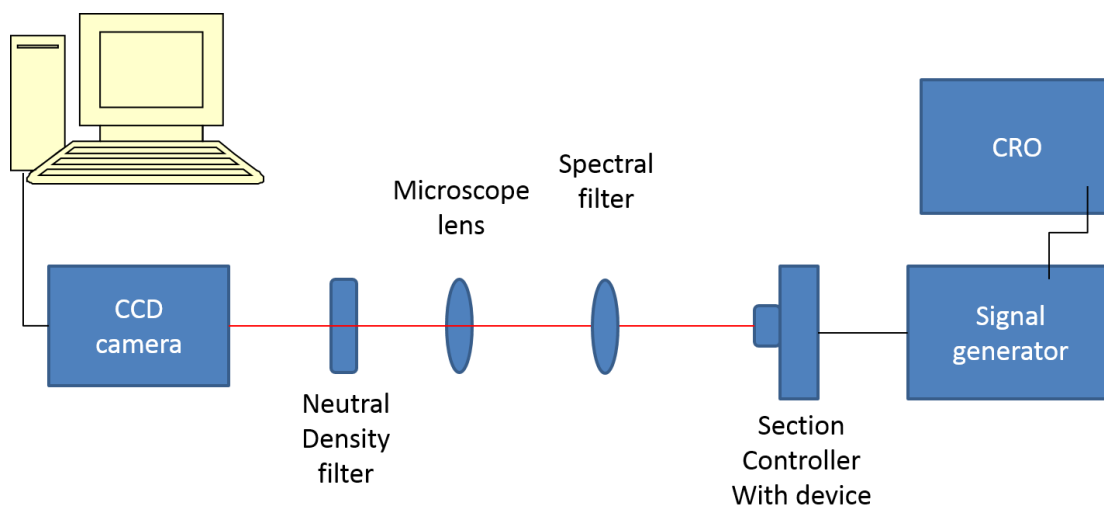


Figure 3.10: The near-field experimental setup schema.

The light emitted from the laser waveguide that is coming out of the facet is called the near-field. Figure 3.10 shows the experimental set up of the near-field measurement. Measurement of the near-field is crucial in determining the current spreading at the stripe of the facet and beam quality of the device. The image of the device was focused using the lens onto the CCD camera front lens. As seen on Figure 3.10 the signal generator was set to a pulsed current of 1000 ns at 1kHz and in this experiment, three set of currents were taken, the threshold current and the two currents 5% above and below the I_{th} value.

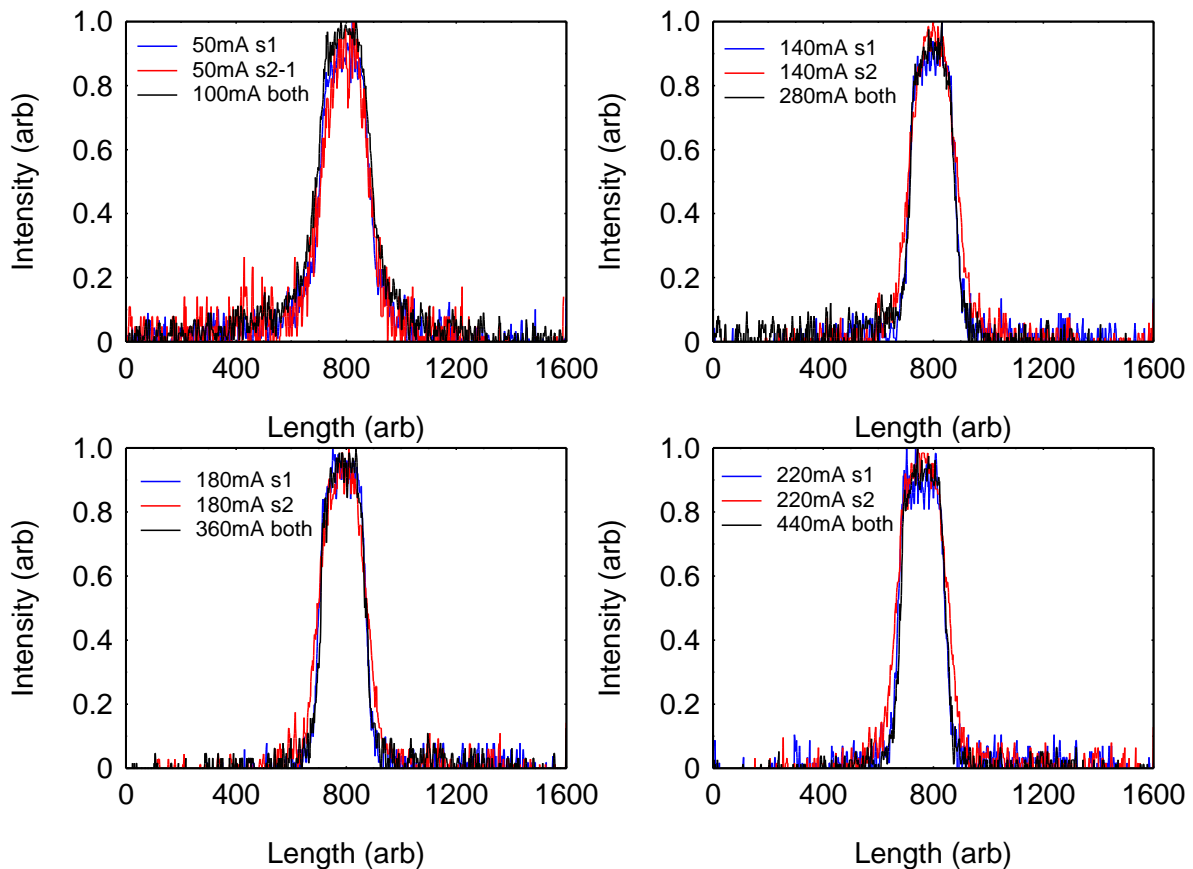


Figure 3.11: The near-field profiles at different input currents.

Before switching on the current, neutral density filters were placed between the lens and the CCD camera to reduce the light intensity entering the CCD camera and this is done to

avoid saturation. A bandpass spectral filter at 670 nm was placed before the CCD camera to allow wavelength 670 ± 10 nm to pass through, hence blocked any stray lasing wavelength from entering. The light intensity from the active region of the facet was picked up by the CCD camera which was shown in real time on the computer. An unsaturated profile of the laser light, in this case the spontaneous emission indicating the extent of the current spreading was recorded. The image in pixels was later compared to the measured facet width using the travelling microscope for calibration.

3.8 Spectrum analyser setup

The experimental setup which was used to measure the wavelength of the laser device is shown in Figure 3.12.

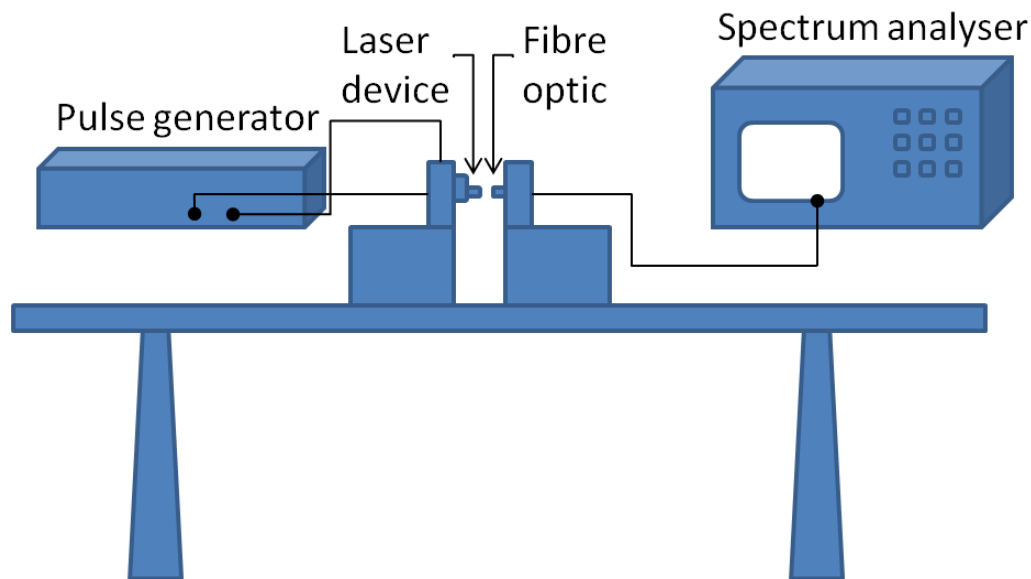


Figure 3.12: The spectrum analyser setup schema.

The pulse generator was applied at 1000 ns time pulse with 1 kHz frequency to the laser device. The aligned laser light enters the optical fibre which transmits the light signal to the spectrum analyser. The measurement was shown in the display of the spectrum analyser in the form of output power as a function of wavelength in nanometres. The resolution of the spectrum

analyser was 0.5 nm. Figure 3.13 shows examples of a normalised lasing wavelength peak of a sample with Ga = 0.58 at 713.8 nm which was pumped at threshold current at 300K.

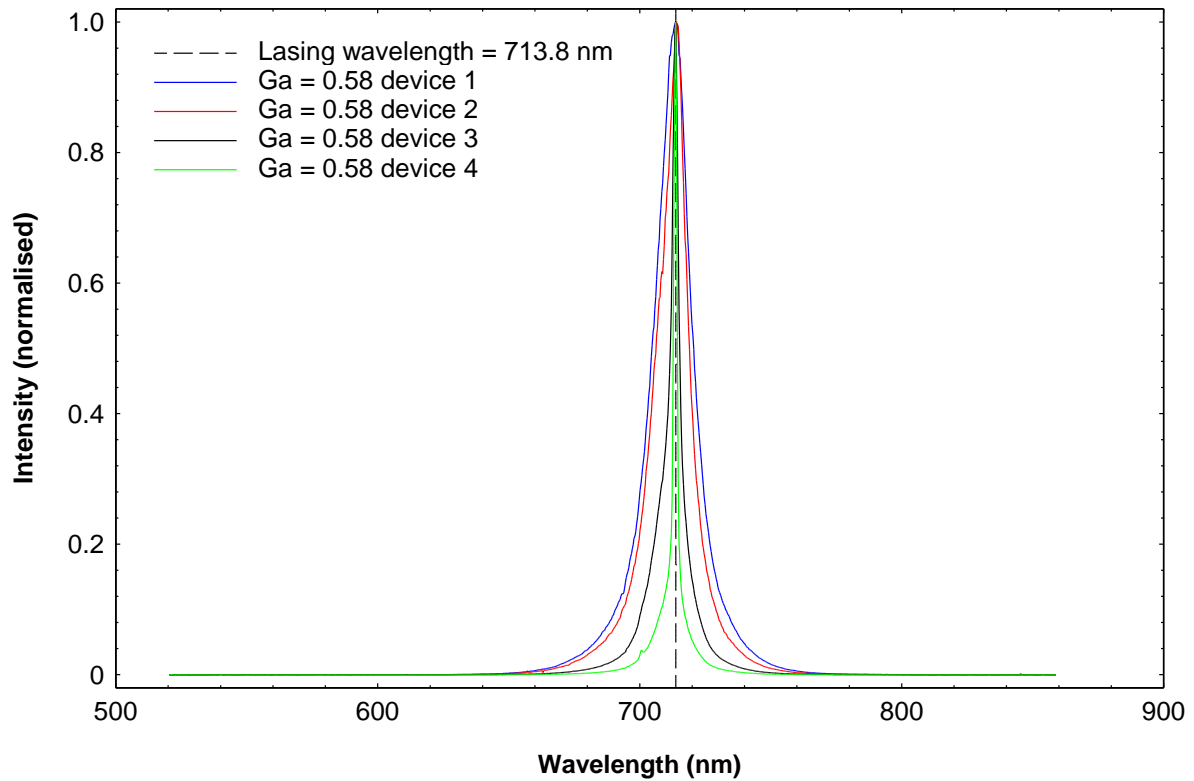


Figure 3.13: Normalised intensity as a function of lasing wavelength at 300K. The 2 mm Ga = 0.58 samples were pumped at threshold current and produced several lasing peak wavelengths around 713.8 nm.

3.9 EPVS measurement

The Edge-Photovoltage Spectroscopy (EPVS) measurement is used to characterise a semiconductor laser using a TE or TM polariser to filter the incoming spectrally resolved white light to the epitaxial layer structure. The light entering the device is used to separate the photo-generated electrons and holes with the built-in p-n junction. Figure 3.14 shows the set up for the EPVS measurement. The light from a halogen lamp goes through the chopper, is passed through a polariser and a monochromator and focused using a lens on to the edge of the facet of the laser or segmented contact device sample and within the waveguide inside the structure.

The TE or TM light is absorbed when the incident photon energy exceeds the transition energy of the layers.

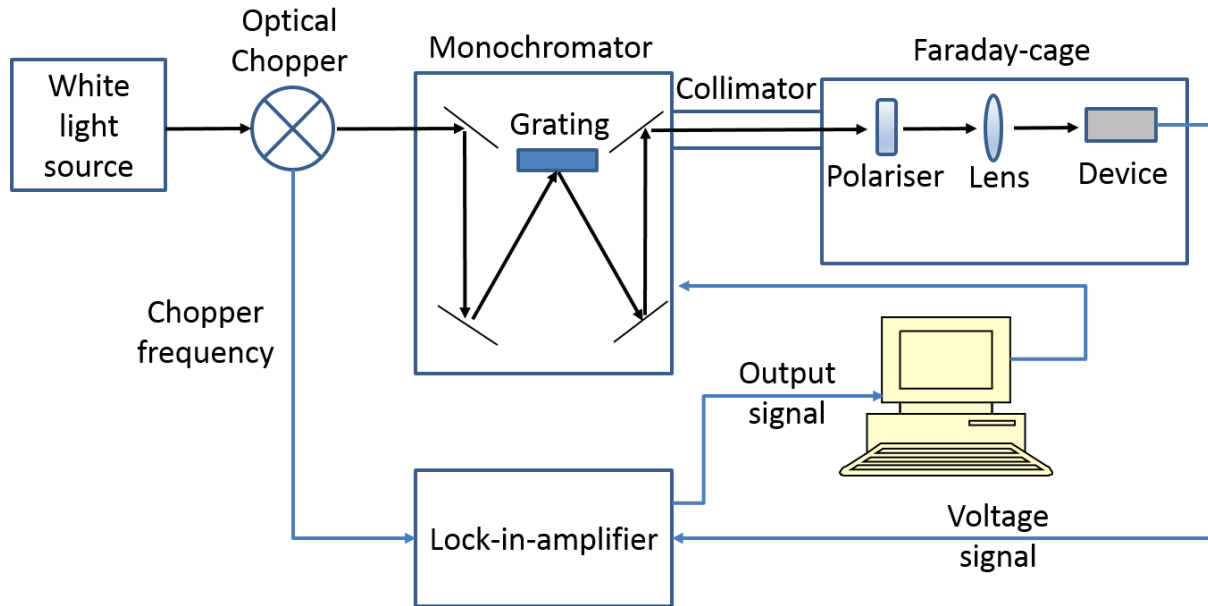


Figure 3.14: EPVS setup schema.

The absorbed incident photon energy is converted to photo-generated electron-hole pairs and these are separated within the junction electric field, producing an external photovoltage, which is later amplified by a phase-sensitive detector. In such a fashion the absorption of incident light, modified by the extraction efficiency of the photo-generated carriers, is measured as a function of wavelength. An example of a TE and a TM absorption curve is shown in Figure 3.15. The signal measured by this system is not the true absorption spectrum due to several factors; firstly the system recorded spectra in arbitrary units because the magnitude varies with alignment and the signal will also be affected by the various optical components. Also some of the photo-generated carriers will recombine in the device before they are extracted and measured; therefore the absorption may not be fully measured, hence the use of the arbitrary units in terms of the absorption magnitude. The wavelength calibration

of the monochromator was performed using a HeNe laser with 632.8 nm wavelength using the spectrum analyser by Peter Rees.

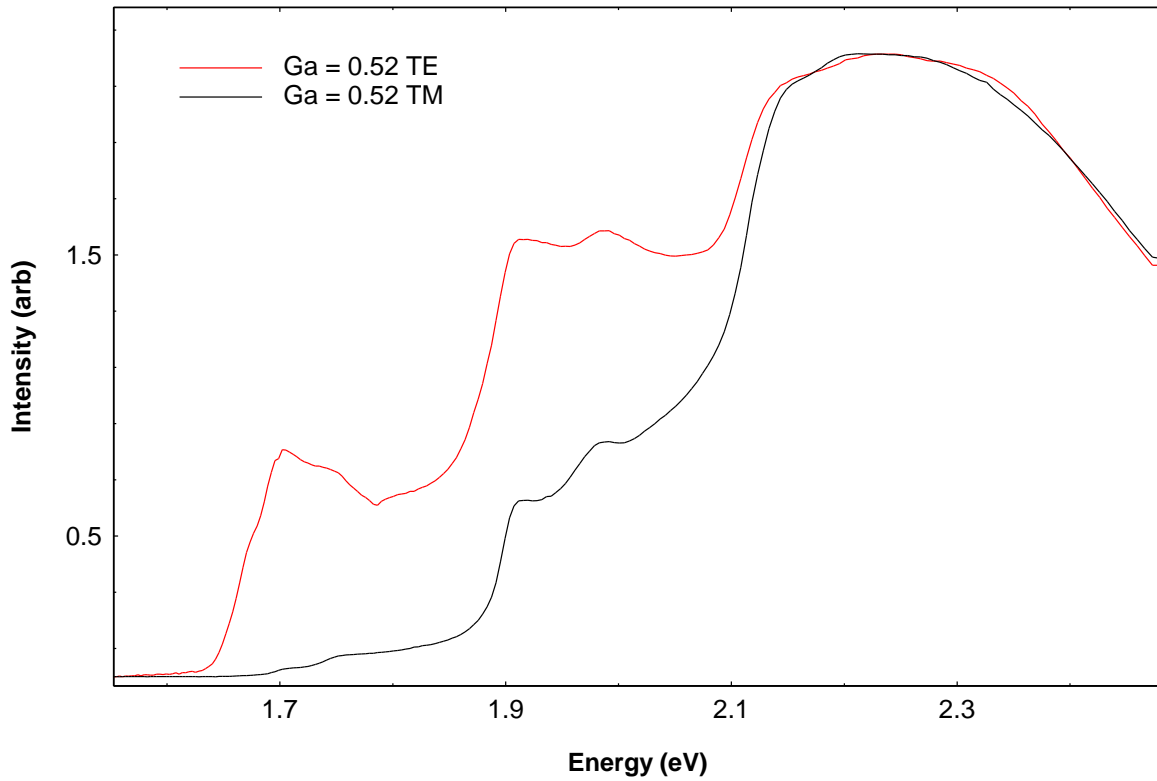


Figure 3.15: Absorption intensity as a function wavelength for EPVS measurement of a sample with $Ga = 0.52$ at 300 K.

3.10 Segmented contact method and the measurement of absorption and gain spectra

The segmented contact processing method is used for fabricating a cut section of the grown wafer into devices required for experimental measurements as mentioned in Section 2.9.1 in Chapter 2. The segmented contact device produces absorption and gain spectra needed to characterise the laser device. Figure 3.4 shows a typical segmented contact device, the processing was done in the cleanroom in a similar way to an oxide isolated stripe laser processing except for the use of $4\ \mu\text{m}$ channel mask instead of the window masks as mentioned previously. There are at least 7 sections created on the pumping area of the segmented contact and each section can be pumped separately. Each length of the section is $300\ \mu\text{m}$ long with a $50\ \mu\text{m}$ wide contact stripe of Au-Zn along the section.

Figure 3.16 shows a typical system used to measure absorption and gain spectra of the segmented contact device. In order to determine the gain and absorption spectra, the measurement of single-pass amplified spontaneous emission (ASE) is required. The ASE is the single-pass light emission which is amplified by electrically pumping the isolated section. The segmented contact device is specifically designed with a passive section at the back of the used section and 10° angle facets with respect to the normal of the mode propagation to avoid multiple-passes of the feedback process of a typical in-plane semiconductor laser.

3.10.1 Experimental Setup

The experimental setup in Figure 3.16 as mentioned earlier is used to measure the ASE spectra of the segmented contact device.

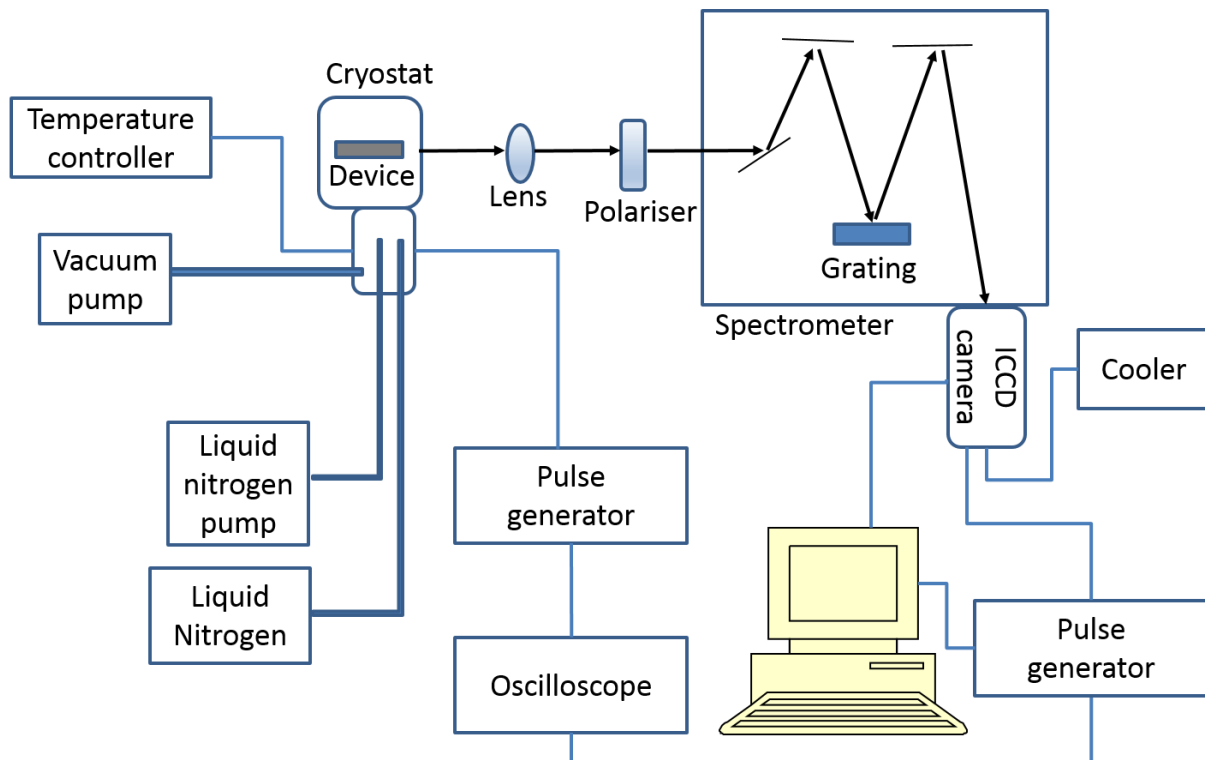


Figure 3.16: The schema of the setup of the gain and absorption experimental measurement using a spectrometer.

The device is placed inside an evacuated cryostat which is mounted on a device holder with six degrees freedom of movement. The cryostat has 4 connections that are used to control the temperature, vacuum, electrical and nitrogen circulation for the cryostat environment. The output light emission from the segmented contact device is collimated using a microscope lens of 5x magnification placed close to the cryostat window to collect ASE which is first filtered using a polariser before entering the slit of the spectrometer. Inside the spectrometer chamber the ASE is split up into wavelength spectrum diffracted from a grating of 1200 lines. The specific wavelengths were then detected by a temperature controlled ICCD camera that can maintain temperature stability and low noise to signal ratio.

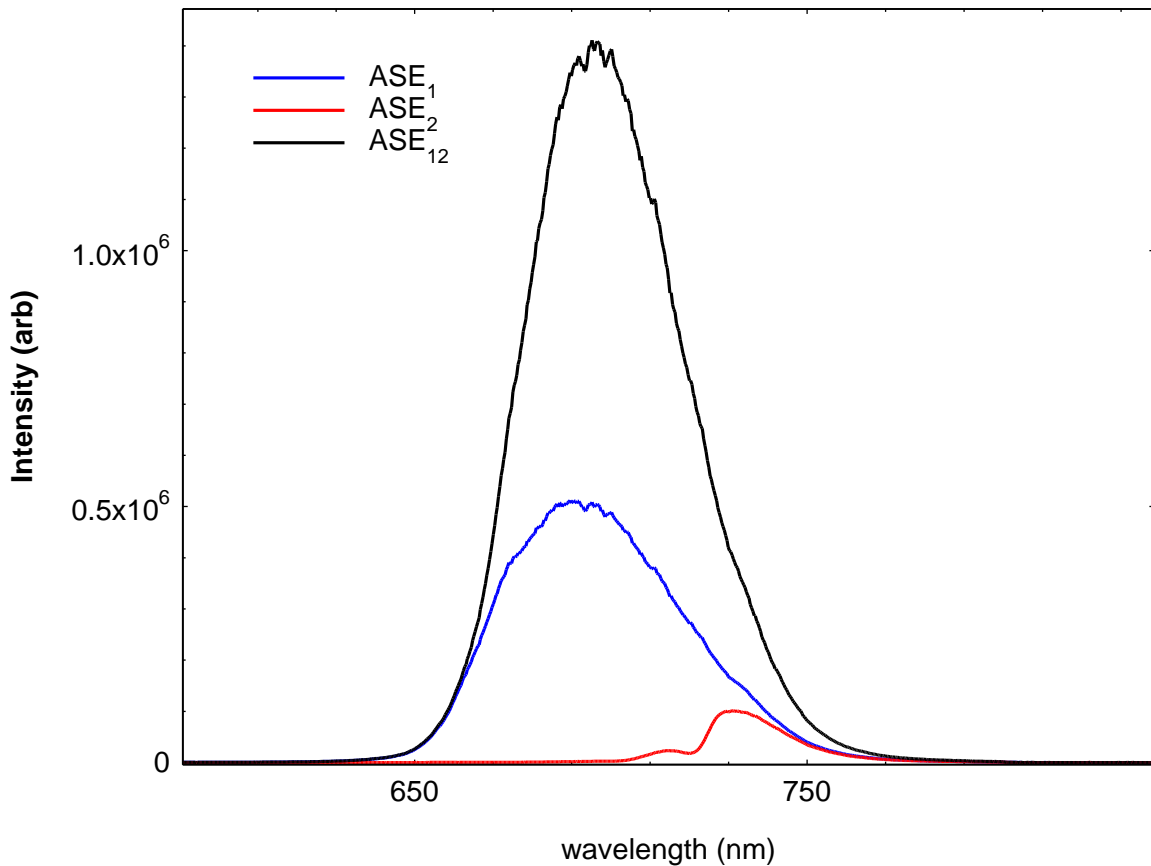


Figure 3.17: Amplified spontaneous emission (ASE) as a function of wavelength for Section 1, Section 2 and Section 1 & 2.

The temperature can be controlled using an automatic temperature controller and the liquid nitrogen pumped from the tank via the transfer tube to the cryostat. The main pulse generator supplies a 1000 ns pulse length with a repetition of 1 kHz frequency to each section of the segmented contact device, while a second pulse generator set to 500 ns pulse length is used to control the ICCD camera and to match its signal with the signal from the main generator. These specifically aligned signal pulses were then transformed by the computer program as ASE profiles for gain and absorption spectra. An example of an ASE spectrum is shown in Figure 3.17. Next we will look into the calculations used in the Segmented Contact Method (Blood 2003) mentioned in Chapter 2.

3.10.2 Gain and Absorption measurements

The gain and absorption measurement approach as described by Al-Ghamdi (2009) using the Segmented Contact Method (Blood et al. 2003) is a standard procedure. The absorption and gain spectra characteristics as mentioned in Section 2.6 in Chapter 2 are determined by using the amplified spontaneous emission (ASE) spectra, which was detected by the ICCD camera. There are several steps needed in measuring the specified amplified emission as shown in Figure 3.17. The pumping area is divided into section 1 and section 2, where the rest of the sections are rendered passive to avoid optical feedback as shown in the previous Figure 4.3. The intensity of the ASE spectrum at the end of the pumping section of length L can be seen (Blood et al. 2003) in equation

$$I_{ASE} = \frac{I_{spon}(e^{(G-\alpha_i)L} - 1)}{G - \alpha_i} \quad (3.2)$$

Where I_{spon} is proportional to the spontaneous recombination rate $I_{spon} = CR_{spon}$, C is the coupling coefficient which represents the photon collection geometry of the measurement

equipment, stripe width, spectrometer resolution and the overall calibration factor of the measurement system.

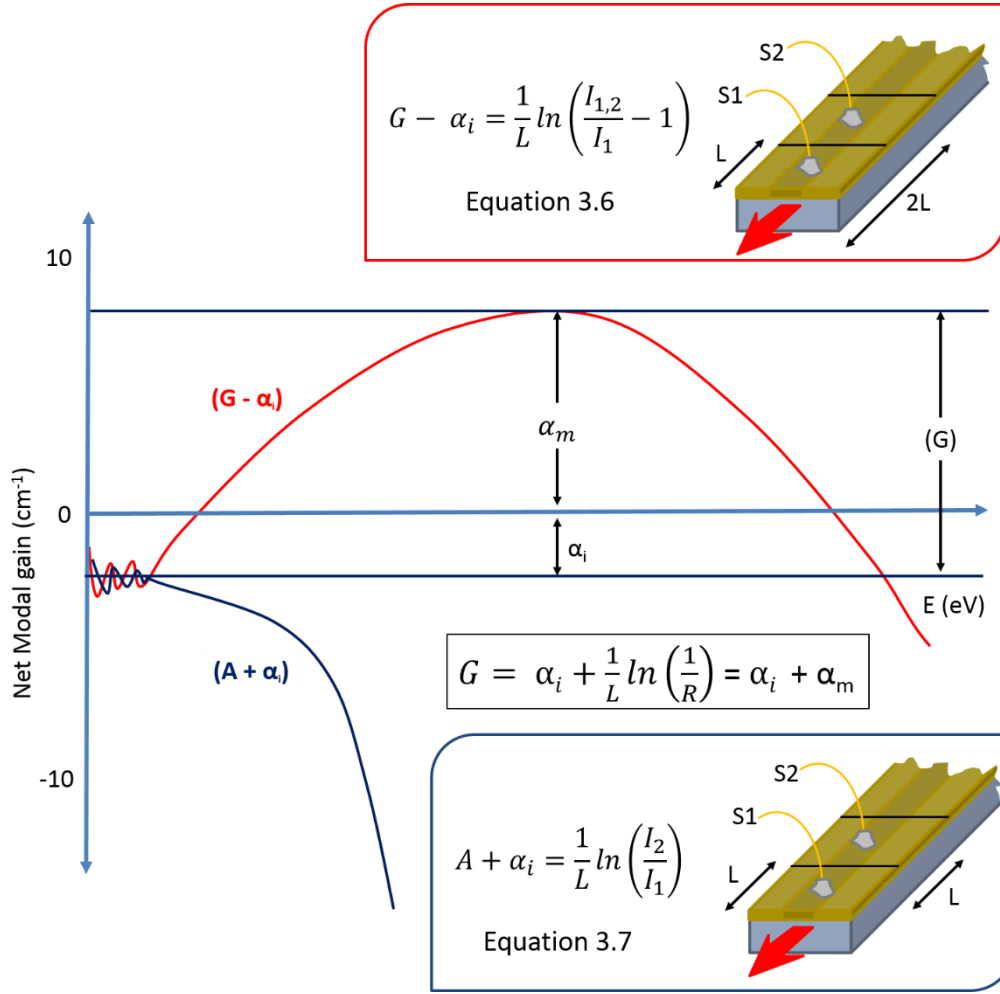


Figure 3.18: Schema of gain and absorption spectra with related equations.

The modal gain and absorption profiles can be determined by comparing the ASE spectra when pumping section 1 or/and section 2 as shown in Figure 3.18. The intensity of these ASE_1 in Figure 3.17, originates from pumping section 1. ASE_2 originates from pumping section 2. Lastly, ASE_{12} originates from pumping both sections. The Equation 3.2 can be used (Blood et al. 2003) to derive the following

$$I_{ASE_1} = \frac{I_{spont} (e^{(G-\alpha_i)L} - 1)}{G - \alpha_i} \quad (3.3)$$

$$I_{ASE_2} = \frac{I_{spont}(e^{(G-\alpha_i)L} - 1)}{G - \alpha_i} e^{(A-\alpha_i)L} \quad (3.4)$$

$$I_{ASE_{12}} = \frac{I_{spont}(e^{(G-\alpha_i)2L} - 1)}{G - \alpha_i} \quad (3.5)$$

The net modal gain is given by dividing equation 3.5 with equation 3.3 as follows (Blood et al. 2003):

$$G - \alpha_i = \frac{1}{L} \ln \left(\frac{I_{ASE_{12}}}{I_{ASE_1}} - 1 \right) \quad (3.6)$$

And the net modal absorption of passive section 1 is given by dividing equation 3.4 with equation 3.3 as follows (Blood et al. 2003):

$$A - \alpha_i = \frac{1}{L} \ln \left(\frac{I_{ASE_2}}{I_{ASE_1}} \right) \quad (3.7)$$

The profiles of the net modal gain and absorption for a segmented contact measurement with the appropriate equations are shown in Figure 3.18. These profiles were determined by substituting the data shown in Figure 3.17 in equation 3.6 and 3.7. The band gap energy between the conduction band and the valence band in semiconductor device can be determined from the absorption spectrum.

3.11 Spontaneous Emission

The spontaneous emission, as explained in Section 2.6 in Chapter 2, is defined as the process whereby carriers in the excited state spontaneously relaxed into the ground state and simultaneously emit a photon. The measurement of the spontaneous emission is obtained from the top window of the laser device as shown in Figure 3.4. It can be used to analyse the studied structures, particularly when it plotted against wavelength. It could give information about the carriers and how they are distributed in the structure during current injection. Next, I will look into the spontaneous emission spectrum experiment.

3.11.1 Spontaneous Emission Spectrum

The intensity of the spontaneous emission is in arbitrary units because an unknown fraction of the emission is collected in the experiment. However it can be normalised to a certain level in order to compare these measurements for various structures. The experimental set up used to measure the spontaneous emission spectra of laser devices is similar to the setup shown in Figure 3.16.

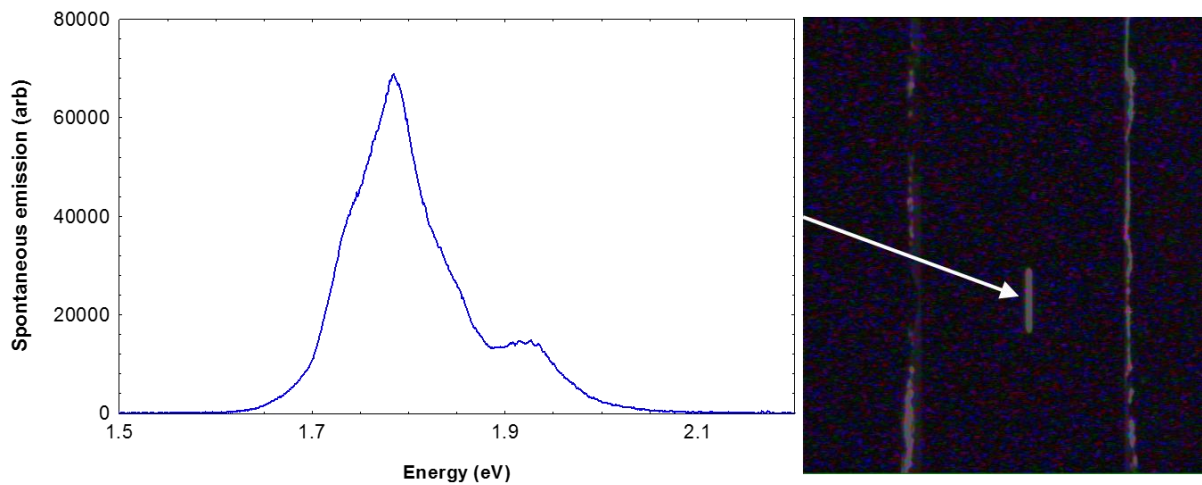


Figure 3.19: Spontaneous emission versus photon energy from the top window of a 2-mm-long laser at room temperature at 154 mA at 300K (left). The spontaneous emission from one of the laser windows in the middle of the device (right).

The laser devices are placed with window part towards the detector as specified in the Figure 3.4 of the mounting section. Different injection current can be applied to achieve the required measurements. The procedure for this measurement in setting the varying temperature is as written in the previous Section 3.10.1. A sample of the output signal is shown in Figure 3.19 for a typical 2-mm-long laser with top window emission at 300K.

3.11.2 Current density at different inversion level

While it is very difficult to determine the carrier density in a working laser device or test structure, we can determine a parameter known as the inversion level (Smowton et al.

2011) as described in Section 2.9.1 in Chapter 2. Inversion level is defined as the difference between the absorption edge energy and the quasi-Fermi level separation energy. The inversion level measurements will be explained in more detail, together with the results in the Chapter 4.

3.12 Calibration

The wavelength calibration of the EPVS experiment was conducted using the HeNe laser and detected with the spectrum analyser. The IVLT experiment and the absorption and gain system were temperature calibrated using a calibrated diode. The same current-probe device was used in calibrating the input current of IVLT experiment and the absorption and gain system. The absorption and gain system were wavelength calibrated using the 632.8 nm wavelength of the HeNe and using a calibrated Hg lamp with its spectral lines provided by the lamp manufacturer. An intensity versus wavelength calibration was also performed on the system using a continuum source with a known intensity versus wavelength spectrum.

3.13 Summary

In this chapter the device structures which have been used for measurements in this thesis were presented. The device preparation for transforming these structures into working laser or segmented contact devices was described. The experimental procedures and equipment used in this study were also described. These were used to measure and evaluate the data presented in the following chapters. These include experiments for measuring the threshold current, transition absorption energies, spontaneous emission from a laser device, the optical gain and absorption by using a segmented contact device and the inversion level at different temperatures. Next in Chapter 4, we will find out about results and analysis of the above mentioned experiments.

Chapter 4

Temperature-Dependent Threshold Current

4.1 Introduction

In this chapter, the temperature-dependent threshold current in InP quantum-dot (QD) lasers is investigated, using samples with $\text{Ga}_{(x)}\text{In}_{(1-x)}\text{P}$ upper confinement layers (UCL) with $x = 0.52$ to $x = 0.58$. All samples were grown at 730°C on a $(\text{Al}_{0.3}\text{Ga}_{0.7})_{0.52}\text{In}_{0.48}\text{P}$ lower confining layer (LCL) as described in Section 3.2.1 in Chapter 3.

This chapter contains a description of several preliminary measurements before going through the main experiment on the temperature-dependent threshold current. These include the selection of the wafer position from which laser and segmented contact devices were obtained, data on threshold current and threshold current density for different lengths and comparison of threshold current density for different Ga composition in the Upper Confining Layer (UCL). I also present results of measurement of gain and absorption spectra as a function of temperature to determine the temperature dependent effects and to obtain the optical mode loss per unit length.

Then I look at the current density to achieve peak net modal gain of 6 cm^{-1} for a 2-mm-long laser and current density to achieve the inversion level (as described in Chapter 3) of 300 K at different temperatures. This is followed by measurement of current density as a function of temperature at a fixed inversion level to find out how these measurements are affected by non-radiative recombination processes. Next I will look at the current density to achieve higher inversion and inversion level to achieve peak modal gain at different temperature to look into non-radiative recombination and carrier spreading into high energy states. Then I will look at the gain achieved at the inversion level required to achieve a gain of 6 cm^{-1} at 300 K and at a fixed inversion level and how the gain varies with temperature at these fixed points. Lastly, I

will look into how the unamplified spontaneous emission measurement as a function of temperatures can demonstrate the distribution of carriers within the quantum dots and well states, and how this may affect the non-radiative recombination processes.

4.2 Characteristics of the wafers grown

The wafers used in this study are grown by MOCVD in a reactor without rotating the substrate during growth as mentioned in Section 3.2 in Chapter 3. There may therefore be a dependence of performance on the location on the wafer from which the samples are taken. Thus, the beginning of this study is to explore whether such differences are significant compared to differences between different wafers.

4.2.1 Selection of wafer for laser and segmented contact devices

An investigation of the wafer structure mentioned in Section 3.3 in Chapter 3 was carried out. During growth material is deposited by vapour flowing across a substrate, for non-rotating substrates there is a concern that the deposited material can be non-uniform across the wafer. Therefore, at the beginning of this chapter, the size of differences in threshold current and wavelength for samples from different locations is investigated before looking into the effect different gallium concentration in the upper confining layer (UCL) has on the characteristics of these devices.

This batch of wafers is part of an ongoing investigation of wafers grown by Sheffield University with processing done in Cardiff University, therefore the selection of sample is limited on the basis of its availability at that time, since this wafer is shared amongst the group. The sample was selected based on the photo- and electro-luminescence (PL and EL) results that showed the best possible area and orientation and the best possible selection for a sample is at the centre of the wafer as described in Chapter 3. Figure 4.1, shows the cut-sections used

for each wafer. Since the largest variation is expected in the direction of flow, the optimum location for samples is side by side towards the centre of the wafer.

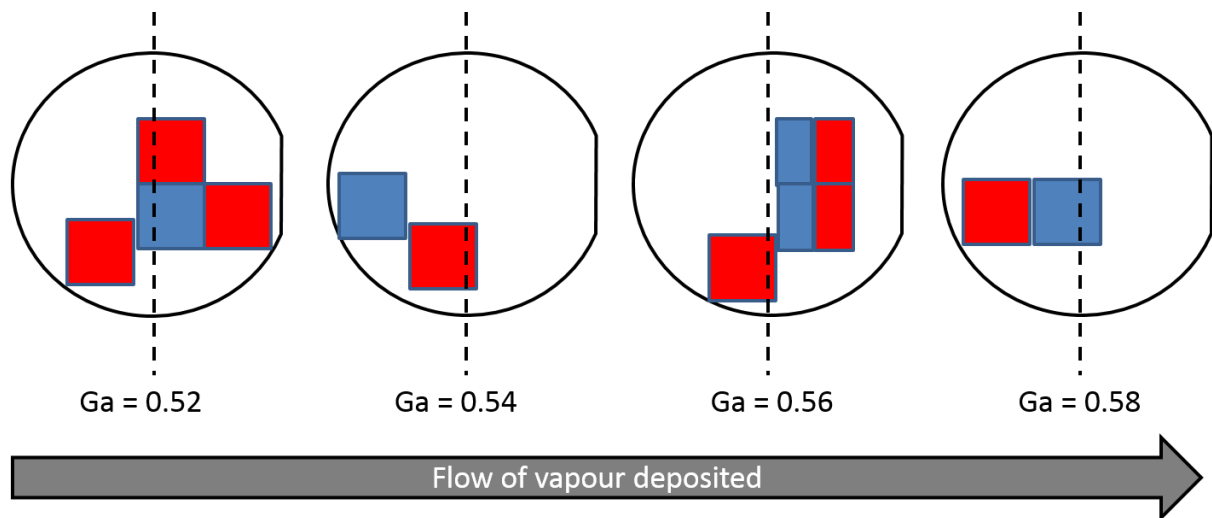


Figure 4.1: Schema of orientation of the position of each cut-section with respect to flow. The red box represents laser and blue box is for segmented contact devices. Ga indicates the content in the UCL. On Ga = 0.56, a new technique using half and half for laser and segmented contact was used.

More recently samples are processed with the same cut-section, half laser and the other half segmented contact, as shown on the Ga = 0.56 at the RHS of the dotted line (or downstream) of the wafer near the major flat in Figure 4.1. This reduces the distance between the laser and the corresponding segmented contact. Initially measurements are taken on Ga = 0.52 and Ga = 0.56 samples from different locations to evaluate the scale of any differences.

4.2.2 Threshold current

The light-current characteristics mentioned in Section 3.6 in Chapter 3 were measured for lasers from different positions of the same wafer, for 2 wafers, Ga = 0.52 and Ga = 0.56. 2-mm-long laser devices were chosen for this investigation.

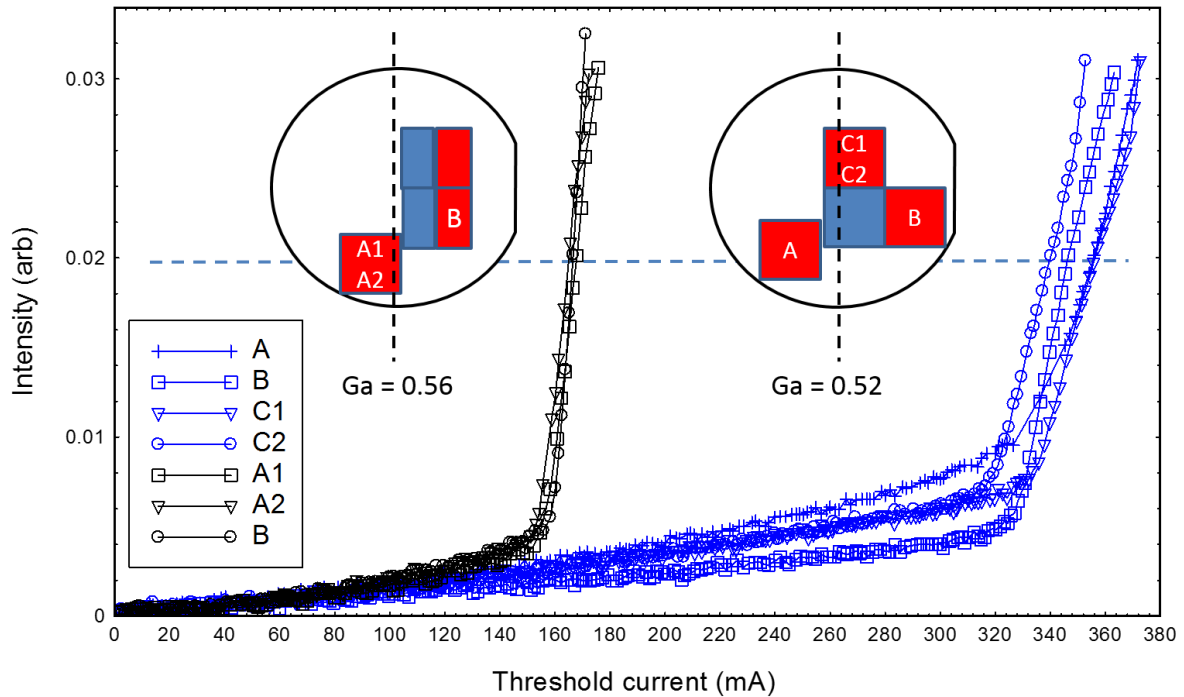


Figure 4.2: Threshold current for Ga = 0.52 (blue marked lines) and Ga = 0.56 (black marked lines) were measured at 300 K. The graph also shows the wafer of Ga = 0.52 and Ga = 0.56 with the selected data used. The horizontal dotted blue line indicates the comparison between Ga = 0.52 and 0.56.

Figure 4.2 shows the light intensity as a function of current for Ga = 0.52 in marked blue lines and Ga = 0.56 in marked black lines, the difference between them is about 170 mA, a preliminary observation indicated that the Ga = 0.56 threshold current (166 ± 1 mA) is at a lower threshold current compared to the Ga = 0.52 (348 ± 10 mA), which clearly shows the difference with gallium composition.

Next, looking at the effect of taking lasers at different position on the wafer, Ga = 0.56 threshold current seems to spread within a small distribution, although each laser was taken from different position as shown in Figure 4.2. Yet, looking at Ga = 0.52 threshold current seems to spread within a wider distribution as if there really was an effect due to extracting lasers from different places on the wafer, but observing the close threshold current readings of A and C1 which were within experimental error in Figure 4.2, this proves that it was not due to the unevenness of the growth distribution. The effect on Ga = 0.52 was more of a random

variation that is affecting the whole wafer, rather than the effect of uneven growth across the wafer. Threshold current can be affected by the pumped area of the device, therefore threshold current density is calculated in the next section to see if the variations in current were due to variation in pumped area.

4.2.3 Threshold current density

A better representation of the threshold current parameter was the threshold current density of the laser device, obtained by using the measured device lengths and using width data obtained from near-field data as described in Section 3.6 in Chapter 3. In this section I present the result of the threshold current density measurement of some of the Ga = 0.52 and Ga = 0.56 sample, measured as a function of temperature for a 2-mm-long lasers and the result of the data is presented in Figure 4.3. Figure 4.3, shows measurement of threshold current density at temperature run between 150 – 405 K, which was expected to cover the range of temperature before and after room temperature that was significant in this study. As expected in the preliminary observation in the previous section, the threshold current of Ga = 0.56 is lower than Ga = 0.52. Moreover, the Ga = 0.56 still maintained its small distribution ($140 \pm 9 \text{ A.cm}^{-2}$) at 300K and even at high temperature, for example, ($240 \pm 15 \text{ A.cm}^{-2}$) at 350K which emphasised that the threshold current density of a laser is independent of the position from which the laser was taken on the wafer. In the case of Ga = 0.52, the distribution ($340 \pm 30 \text{ A.cm}^{-2}$) at 300 K is large and even larger ($700 \pm 100 \text{ A.cm}^{-2}$) as it reached 350 K as expected by looking at the threshold current in the previous section. Since the larger distribution does not correlate with where the sample comes from suggest a fundamental characteristic of this wafer, not related to the position the lasers were taken from as mentioned in the previous section.

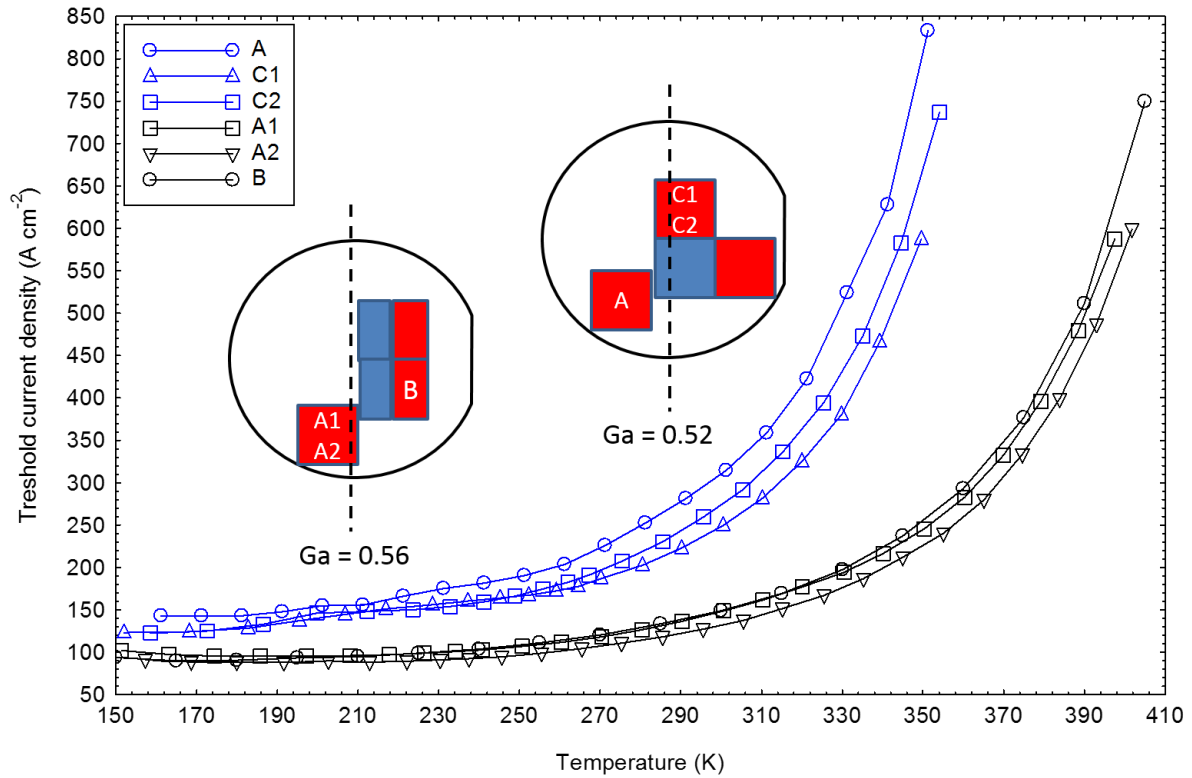


Figure 4.3: Threshold current densities for Ga = 0.52 (blue marked lines) and Ga = 0.56 (black marked lines) were measured as a function of temperature. The graph also shows the wafer of Ga = 0.52 and Ga = 0.56 with the selected data used.

Therefore, the consistency of the results in this section and the section before it, one can conclude that any result presented after this is not related to any uneven distribution of material growth across the wafer under investigation. In the coming section, the research will be based on the samples with $\text{Ga}_x\text{In}_{(1-x)}\text{P}$ upper confinement layers (UCL) with $x = 0.52$ to $x = 0.58$, but before that, a suitable cavity length with threshold current density as a function of temperature must be selected for the comparison.

4.2.4 Threshold current with different lengths

Different lengths of the laser cavity are investigated to select the most significant cavity length for the study of the threshold current density for all the samples with different gallium concentrations in the upper confining layer in the next section. In this case, Ga = 0.56 was used

as an example, the threshold current densities for each of the $Ga = 0.56$ samples of lengths 1 – 4 mm is measured as a function of temperature and the result is shown in Figure 4.4.

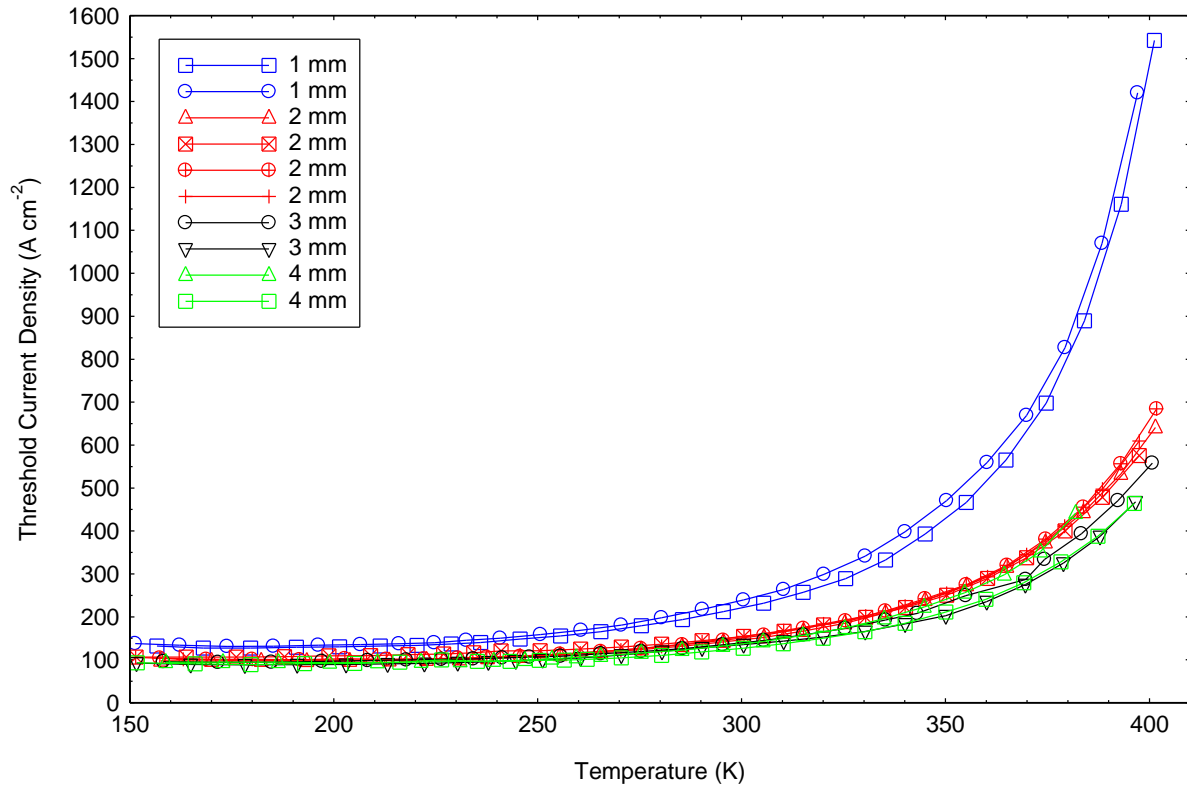


Figure 4.4: Threshold current density for different lengths of lasers as a function of temperature for $Ga = 0.56$.

Figure 4.4 shows that the threshold current densities decreases with increasing length of the laser. The obvious feature is that 1 mm devices had a very high threshold current density compared to the other lengths, while the 2 mm devices is more comparable to the 3 and 4 mm at higher temperature. In general, and based on the results of Figure 4.3 and 4.4, a 1 mm device for $Ga = 0.52$ is not likely to exhibit lasing over a sufficiently wide temperature range to make it useful in this study. In the case of 3 or 4 mm devices, these lengths could show overlapping comparable results which will have close range distributions as indicated in the previous section on threshold current density. In addition, some of the important comparisons amongst Ga composition with 2 mm device will not be apparent for 3 or 4 mm devices as differences may only be seen beyond 400K for the $Ga = 0.56$ and 0.58. Therefore, to make a good

compromise measurement in this study, 2-mm-long lasers with criteria as mentioned in Section 2.5 in Chapter 2 and in Section 3.6 in Chapter 3, will be used for comparison in the next section as well as comparison with other previous study in Chapter 5 later on.

4.2.5 Comparison of threshold current density

Threshold current densities of samples with $\text{Ga}_{(x)}\text{In}_{(1-x)}\text{P}$ upper confinement layers (UCL) with $x = 0.52$ to $x = 0.58$ were compared in this section and the results are shown in Figure 4.5. This figure shows a non-linear increase of threshold current density as a function of temperature for a 2-mm long laser for all of the Ga composition in the UCL. This figure also shows that the laser with a composition of $x = 0.58$ had the lowest threshold current density across the temperature range 240-400 K. At 300 K a value of 138 Acm^{-2} was obtained compared to a previous best of threshold current density of 150 Acm^{-2} at 300 K for 2-mm-long lasers (Al-Ghamdi et al. 2013). The laser with $\text{Ga} = 0.56$ also has a lower value of 149 Acm^{-2} at 300 K compared to previous data and also shows a promising result in terms of temperature dependence performance. As gallium composition decreases from $\text{Ga} = 0.56$, the performance of the lasers worsen from $\text{Ga} = 0.54$ at 186 Acm^{-2} to $\text{Ga} = 0.52$ at 248 Acm^{-2} at 300 K.

In a previous study by Smowton et al (2011) the threshold current density increased rapidly at higher temperature being in excess of 800 Acm^{-2} at 350K, which is different to the results of Figure 4.5 where, for example, at $\text{Ga} = 0.52$ threshold current density is as low as 593 Acm^{-2} at 350 K. Likewise, as the gallium composition in the UCL is increased, more improvement is seen with for $\text{Ga} = 0.58$ with a low value of 235 Acm^{-2} achieved and an equally low value of $\text{Ga} = 0.56$ at 256 Acm^{-2} , both at 350 K. The reason for this improvement is the topic of this and the next chapter.

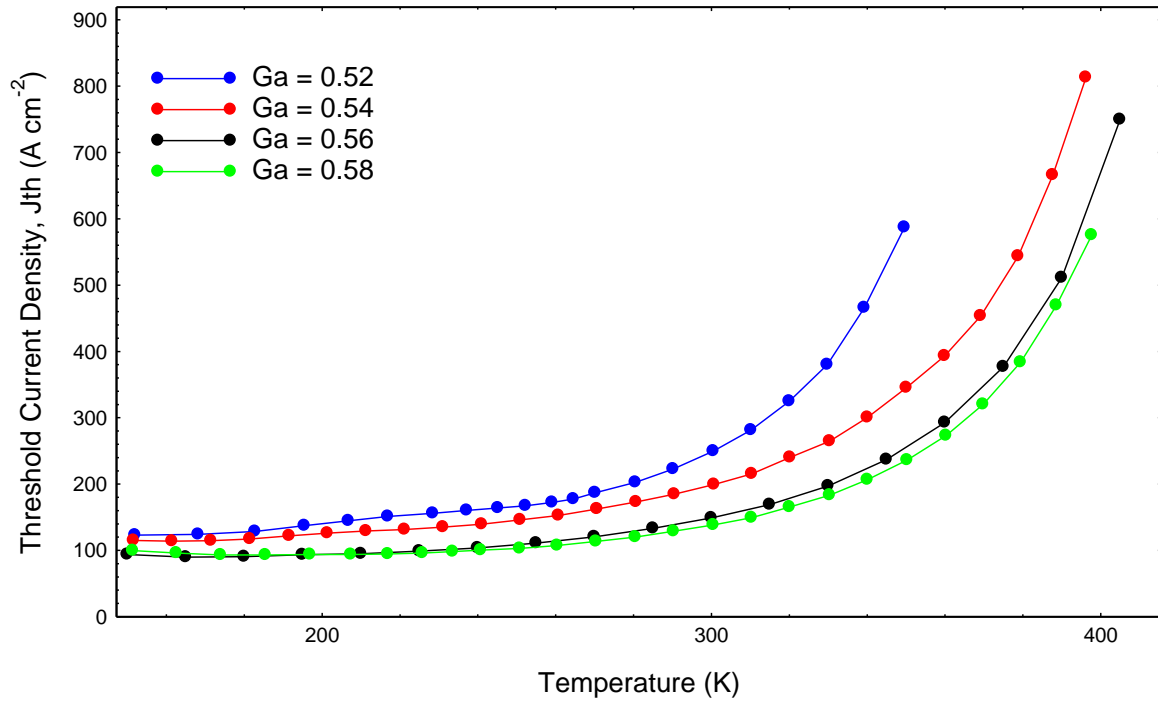


Figure 4.5: Threshold current density for 2-mm-long-lasers as a function of temperature for different gallium concentrations in the upper confining layer.

4.3 Laser energy at different sample lengths

The lasing energies of different lengths of laser are plotted on Figure 4.6. The lasing energy increases at increasing gallium composition except for $Ga = 0.52$, which is unusually higher than the trend. The result shows that shorter cavity lengths with a higher gain requirement lase at higher energy, and it is typical of quantum dot structures, where state filling occurs resulting in higher gain requirements and this will be further illustrated in Figure 4.16(b) using 300 K and 360 K data. To understand the threshold current density and lasing wavelength data for the different gallium composition, I will now turn to more fundamental measurements.

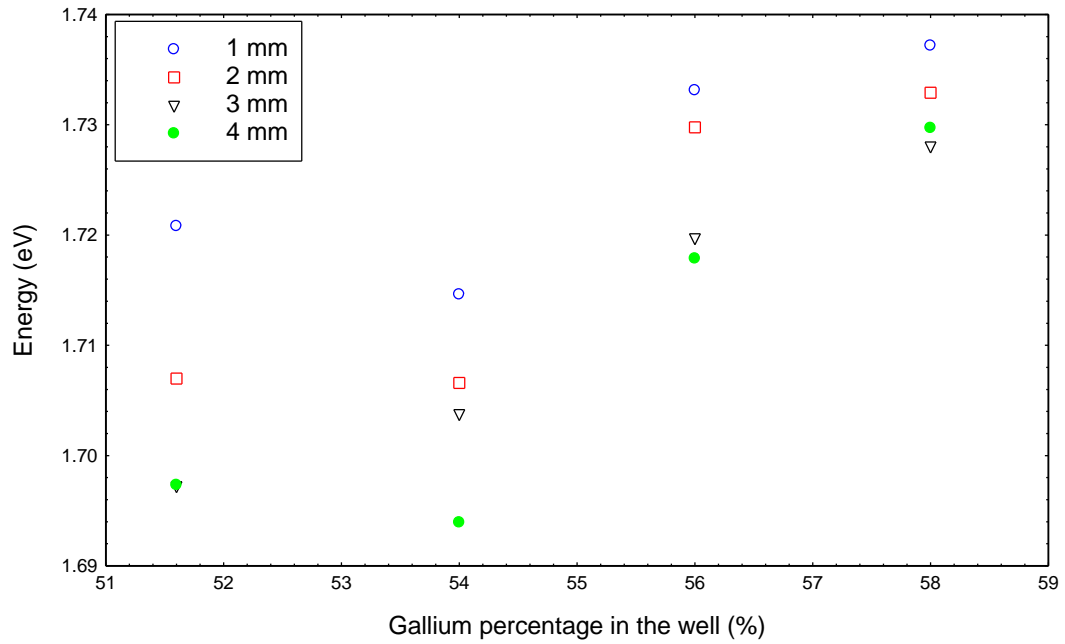


Figure 4.6: Laser energy of lasers with gallium concentration in the UCL at different lengths at 300K.

4.4 Optical Absorption Spectra

The optical absorption spectra are studied in this section, which is mentioned in Section 2.5 in Chapter 2. This includes the optical absorption spectra for Ga concentration, $x = 0.52$ to $x = 0.58$ in the $\text{Ga}_{(x)}\text{In}_{(1-x)}\text{P}$ upper confinement layers (UCL) using measurements of the amplified spontaneous emission obtained from the segmented contact technique and calculated by using Equation 3.7 in Chapter 3. Measurements of the modal absorption versus photon energy show the allowed transitions as shown on Figure 4.7.

The absorption spectra in Figure 4.7 shows features that are considered to be inhomogeneously broadened large dot ground state (LGS) and large dot excited state (LES) as previously identified (Al-Ghamdi et al. 2013) in similar samples. Absorption due to the dot states is well defined for the $\text{Ga} = 0.52$, more well defined and with higher magnitude for the $\text{Ga} = 0.54$. The magnitude of the absorption peak is almost the same for all the gallium composition except for the $\text{Ga} = 0.52$. Gain and absorption are related as described in Section

2.6.2 in Chapter 2, and so a lower value of absorption indicates that the maximum gain that can be obtained from the material will be lower.

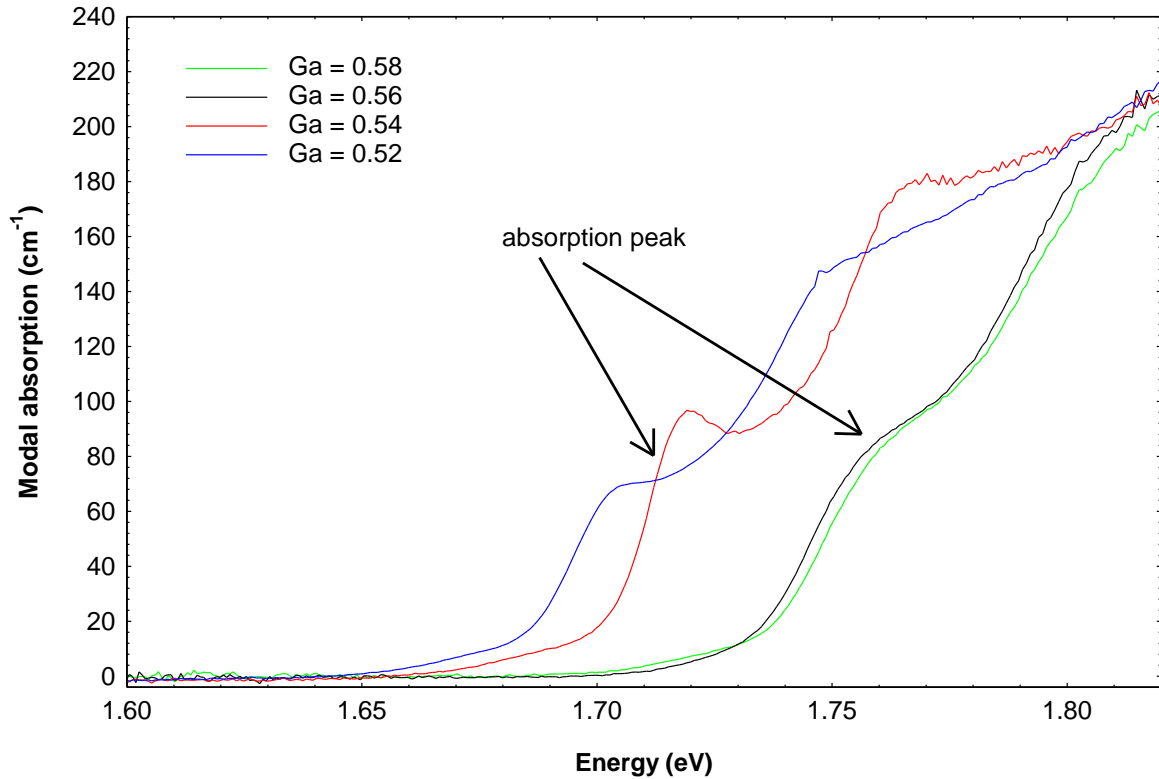


Figure 4.7: Measured modal absorption spectra of different Gallium concentration at 300 K.

The definition of the dot states at the absorption peak increased from the Ga = 0.52 to Ga = 0.54 and then became less defined for the rest of the Ga compositions. The less defined peak of the absorption dot states indicates a larger degree of inhomogeneous broadening as mentioned in Section 2.7 in Chapter 2. This will also reduce the gain at a particular degree of inversion as observed in the previous study by Elliott et al (2012). The threshold current density and the temperature dependence of threshold current density is likely to be affected by the inhomogeneous broadening as it affects the maximum available gain at a wavelength (Smowton and Blood 2010). The measurements of Figure 4.7 also indicate that the dot ground state shifts to higher energy as the UCL layer changes from $x = 0.52$ to $x = 0.58$. To explore

this more fully we examine the EPVS absorption spectra of these samples and the result of these data will be discussed further in this chapter.

4.5 Comparison of peak energies

The wavelength of the material studied has been covered using different technique as mentioned in Section 3.8 in Chapter 3 and having more information on the photon energy of the material can be useful in characterising the devices. In Figure 4.8, the results of measurements using different techniques and for lasers and other peak energies are plotted on the same graph.

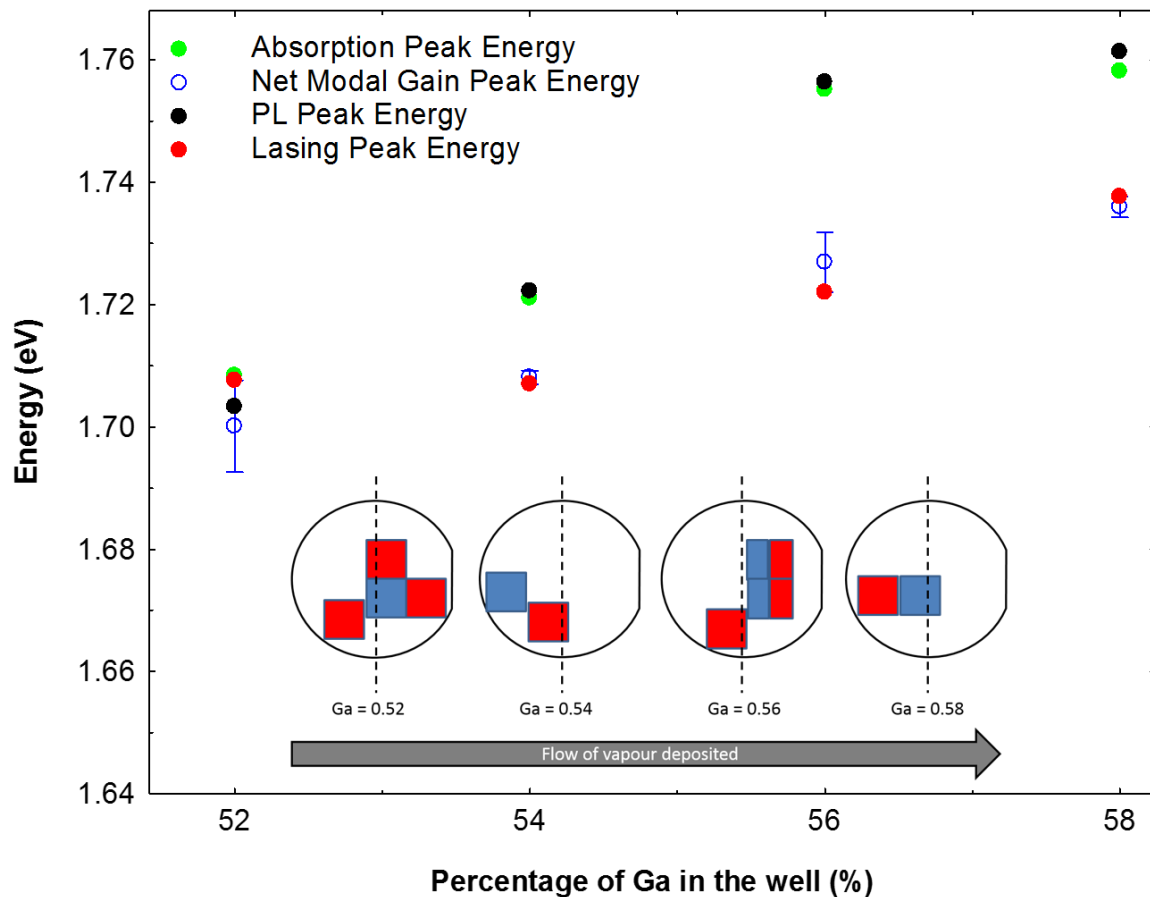


Figure 4.8: Photoluminescence (PL) peak, absorption peak, net modal gain peak and lasing peak energies for 2-mm-long laser as a function of gallium composition. The PL peak energy measurement was done at Sheffield University (mentioned in Section 3.3.3 in Chapter 3). The cut-section is added for comparison. The error bar indicates the difficulty of measurement of the net modal gain peak energy.

Both PL peak and absorption peak energies shows an increasing photon energy as gallium composition increases in Figure 4.8, which implies the fundamental characteristics of these wafers. This seems to suggest that the dot state energies are affected in the same sense as the well energy itself which increases with Ga content. The lasing energy shows increasing photon energies as gallium composition increases except for the lasing energy of Ga = 0.52 which remains high as previously shown in Figure 4.6. The most likely explanation is that the sample has a high gain requirement, which leads to a high threshold current density and a relatively short lasing wavelength similar to the behaviour of short lasers relative to long lasers in Figure 4.6. The net modal gain peak energy shows increasing photon energies as gallium composition increase. The difference between energies for laser and segmented contact measurements will be examined in the next section.

4.6 EPVS results with wavelengths

The result of the edge-photovoltage spectroscopy (EPVS) absorption measurement is discussed in this section. Edge PVS measurement as mentioned in Section 3.9 in Chapter 3 allow us to determine the photon energies of both dot states and the quantum well states and most importantly for both the segmented contact and laser samples. This section is divided into 2 parts, the first, describing different QW and QD transition energies and the second the difference in wavelength or energy of the large ground state (LGS) with position on the wafer.

4.6.1 Transition energy using EPVS for laser and segmented contact devices

The absorption spectra were taken using the EPVS measurement at both polarisation, TE and TM, on the laser and segmented contact devices for Ga concentration from $x = 0.52$ to $x = 0.58$ in the $\text{Ga}_x\text{In}_{(1-x)}\text{P}$ upper confinement layers (UCL) as mentioned in Section 3.9 in Chapter 3. The results are plotted and exciton transition energies were identified for both laser

and segmented contact devices to characterise the structure as shown in Figure 4.9. But note the intensity measurement is in arbitrary units and the shape of the spectrum is affected by the variation in distance over which absorption occurs (Smowton et al. 1996). Figure 4.9 shows the transition energies of TE and TM polarised curves indicates the quantum dot large ground state (LGS) and large excited state (LES), then the quantum well or Upper Confining Layer (UCL) and the Lower Confining Layer (LCL) of the absorption spectra (Elliott et al. 2012). The absorption at higher energies is related to the waveguide material (Smowton et al. 1996). The possible exciton transition of electrons to the heavy holes (e-hh) and light holes (e-lh) are in the quantum well (QW) region. Figure 4.10 shows a schema of the transition energies in the active region. The EPVS data will be discussed in detail in the next chapter.

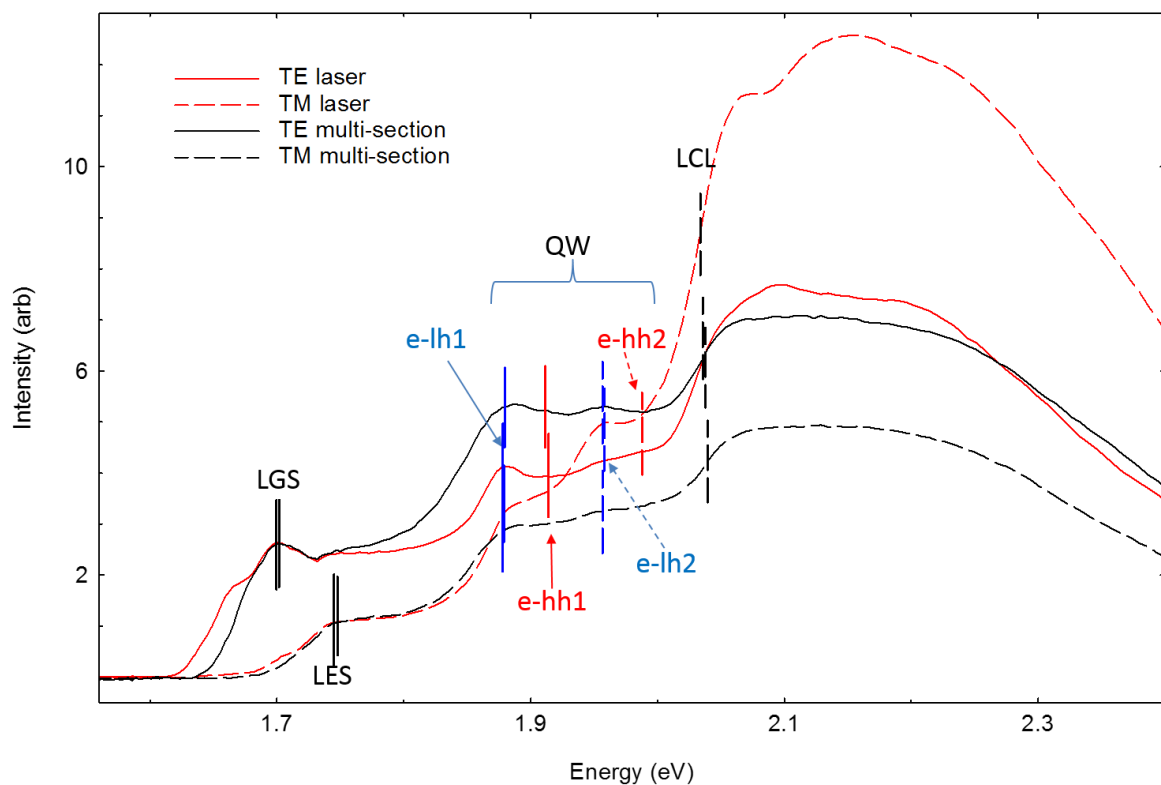


Figure 4.9: Result of an EPVS measurement on a Ga = 0.58 sample with TE and TM polariser. The small vertical lines indicates the possible transition energies taken at 300 K for both laser and segmented contact devices.

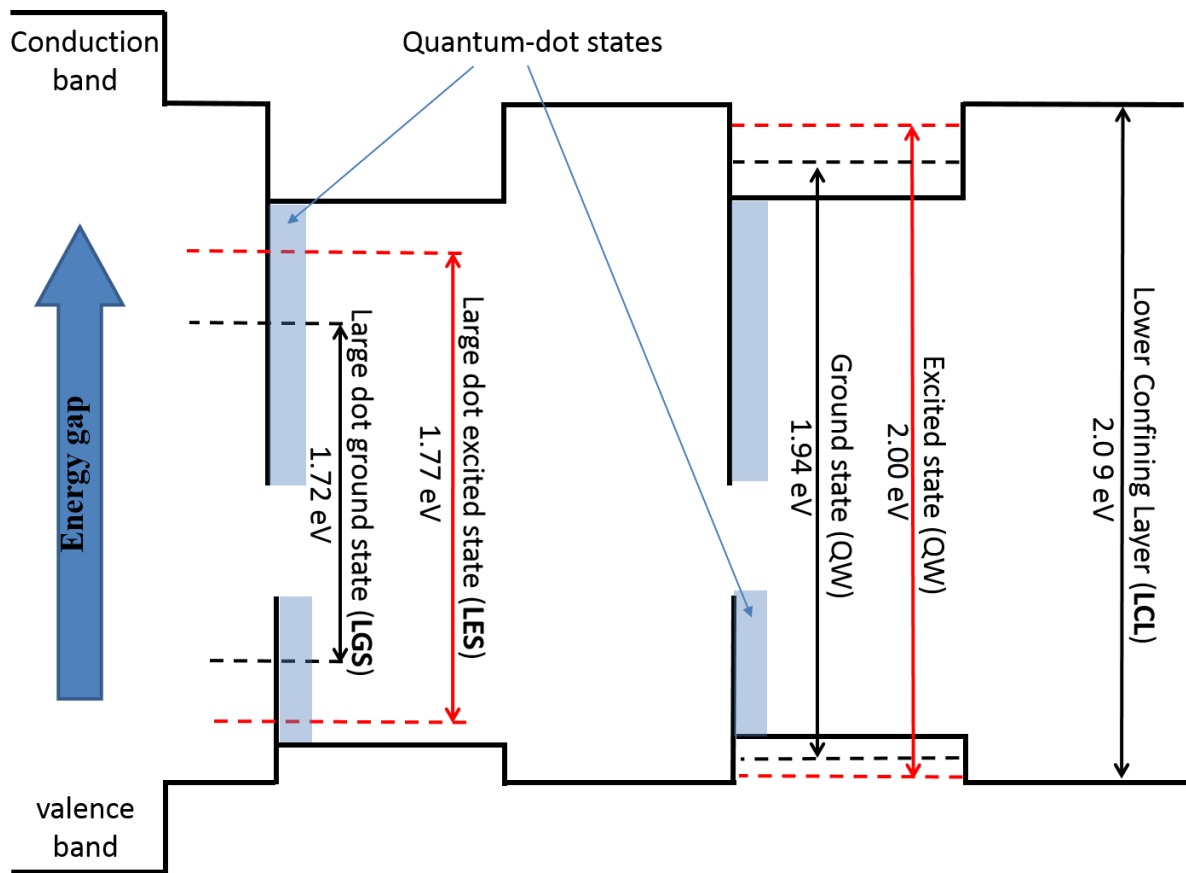


Figure 4.10: Schema of the energy transition based on valence and conduction bands for $Ga = 0.58$.

4.6.2 LGS difference on position on the wafer

Although there was no significant difference in the threshold current densities for samples taken from different places on the wafer, further investigation is needed to see whether this holds for their transition energies. The data in Figure 4.11 shows that the upstream laser in A (upstream) is closer in energy to laser and segmented contact in C (downstream), rather than laser and segmented contact energies in B (also a downstream). This indicates that there is no significant difference due to position and orientation of the cut-section of laser and segmented contact, which is in agreement with data shown in Figure 4.8. Figure 4.11, also shows a spread of peak energies, whereby the laser and segmented contact cut-section show a significant difference relative to the step size of 5 angstroms or 1.16 meV. Although, this result seems to

suggest an energy difference due to selecting the laser and segmented contact devices in different positions, such an effect is not significant when compared to the result presented in Figure 4.8, for different Ga composition, where the differences are much larger. This result shows that the correct vicinity and orientation has no significant affect on the characterisation of these samples. A summary of the gallium percentage in the upper confining layer transition energies will be compared with other studies in Chapter 5. Next, I will look into the dependence of threshold current density on temperature in the next section.

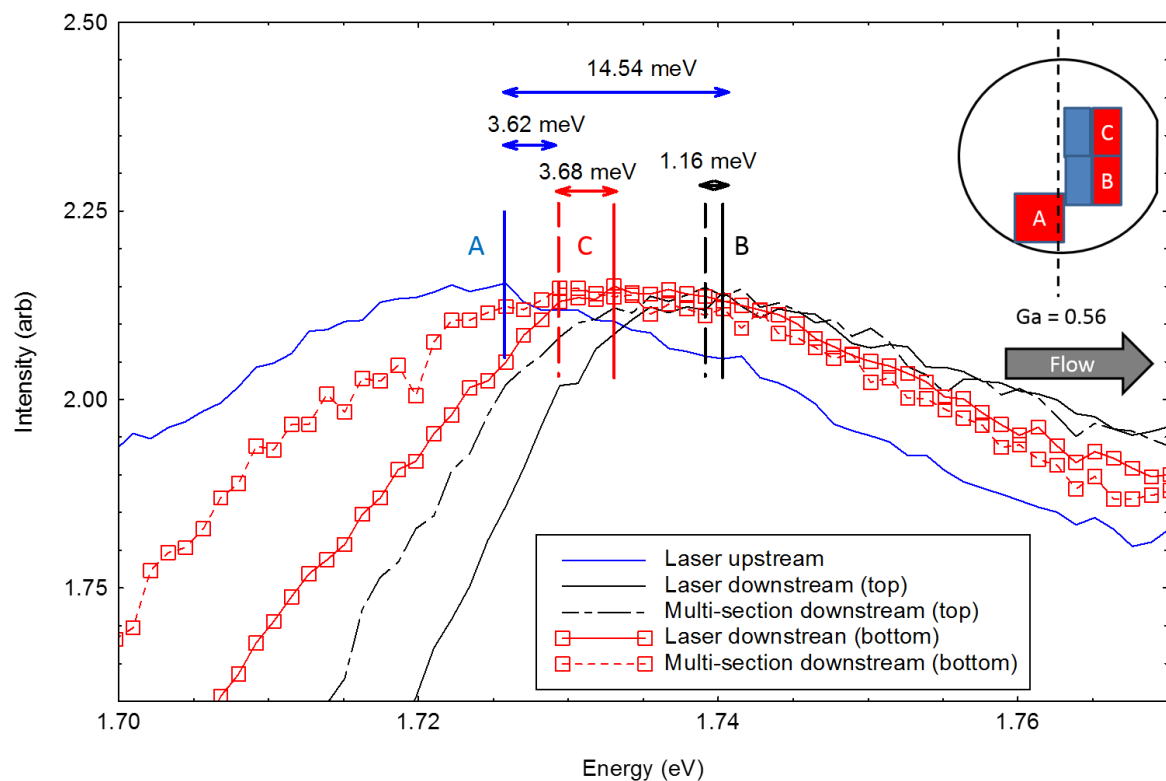


Figure 4.11: An insert of Ga = 0.56 wafer showing a laser from upstream and half and half laser and segmented contact on the top and bottom of downstream cut sections. This wafer is related to the peak LGS curves using TE polariser taken at 5 \AA wavelength steps or 1.16 meV.

4.7. The net modal gain and absorption with lasing energy

This section addresses the relationship between the laser and the segmented contact devices in terms of lasing wavelengths and gain requirements as mentioned in Section 2.9 in Chapter 2 and measurement and set up as seen in Section 3.10 in Chapter 3.

4.7.1 Measurement at room temperature

I will first introduce a new way of determining the mode loss per unit length (α_i) from the segmented contact measurements that leads to a smaller uncertainty. Before that, the mode loss per unit length (α_i) is normally determined as the value that the loss (at net modal absorption or $A + \alpha_i$) and gain (at net modal gain or $G - \alpha_i$) spectra tend to at low photon energy as illustrated in Figure 4.12(a).

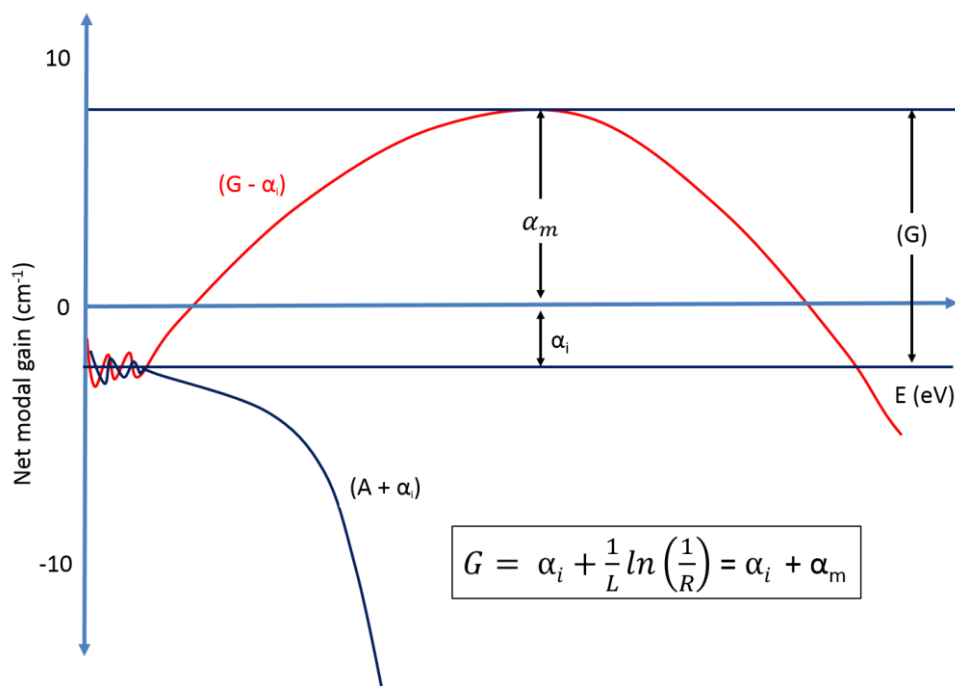


Figure 4.12(a): Schema of the net modal gain and net modal absorption spectra of the segmented contact device. The horizontal dark blue solid line represent peak net modal gain ($G - \alpha_i$) and net modal absorption ($A + \alpha_i$). The height between them is the peak modal gain (G).

However, this value is subjected to experimental uncertainty and a systematic error due to sample alignment. Figure 4.12(b) shows three segmented contact devices cleaved from the same sample of $Ga = 0.54$, each device has criteria as mentioned in Section 3.5.1 in Chapter 3. It is observed that the value of the optical mode loss per unit length (α_i) is normally determined at the low photon energy and can change with the experimental settings of each segmented contact device (device 1 = -4.90 cm^{-1} , device 2 = -7.64 cm^{-1} and device 3 = -4.70 cm^{-1}).

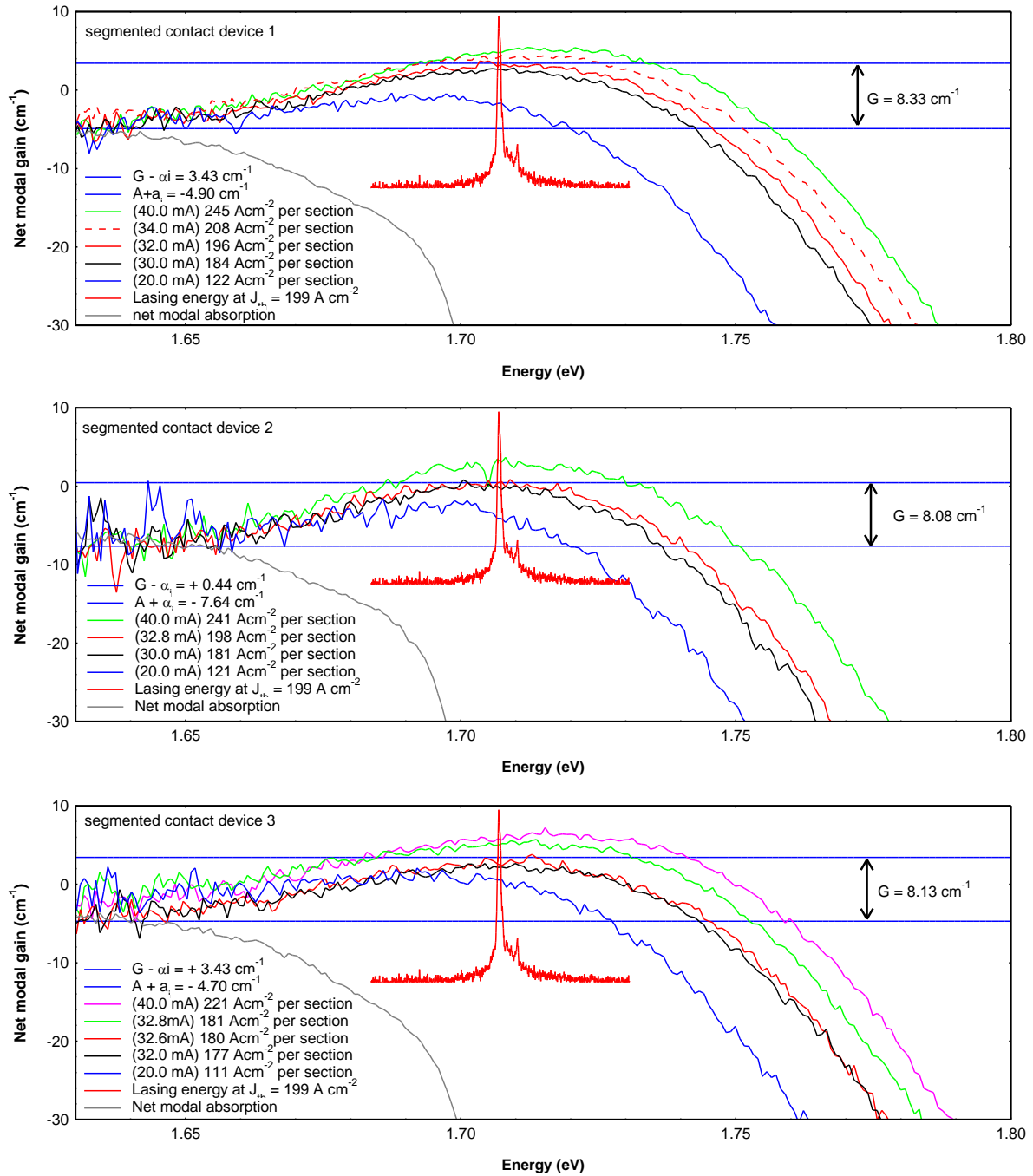


Figure 4.12(b): Net modal gain and net modal absorption spectra of three segmented contact devices measured at 300 K and at a current density corresponding to threshold of a 2-mm-long laser. A lasing energy of a 2-mm-long laser (in arbitrary units) is added to the respective graph at 300 K for the $G = 0.54$ for comparison.

Therefore, the device selection is based on the lowest α_i that can achieve the highest gain requirement, in which case either segmented contact device 1 or 3 can be selected. The selection is based on the nearest possible current density that is expected to be achieved, when compared to the threshold current density of the laser.

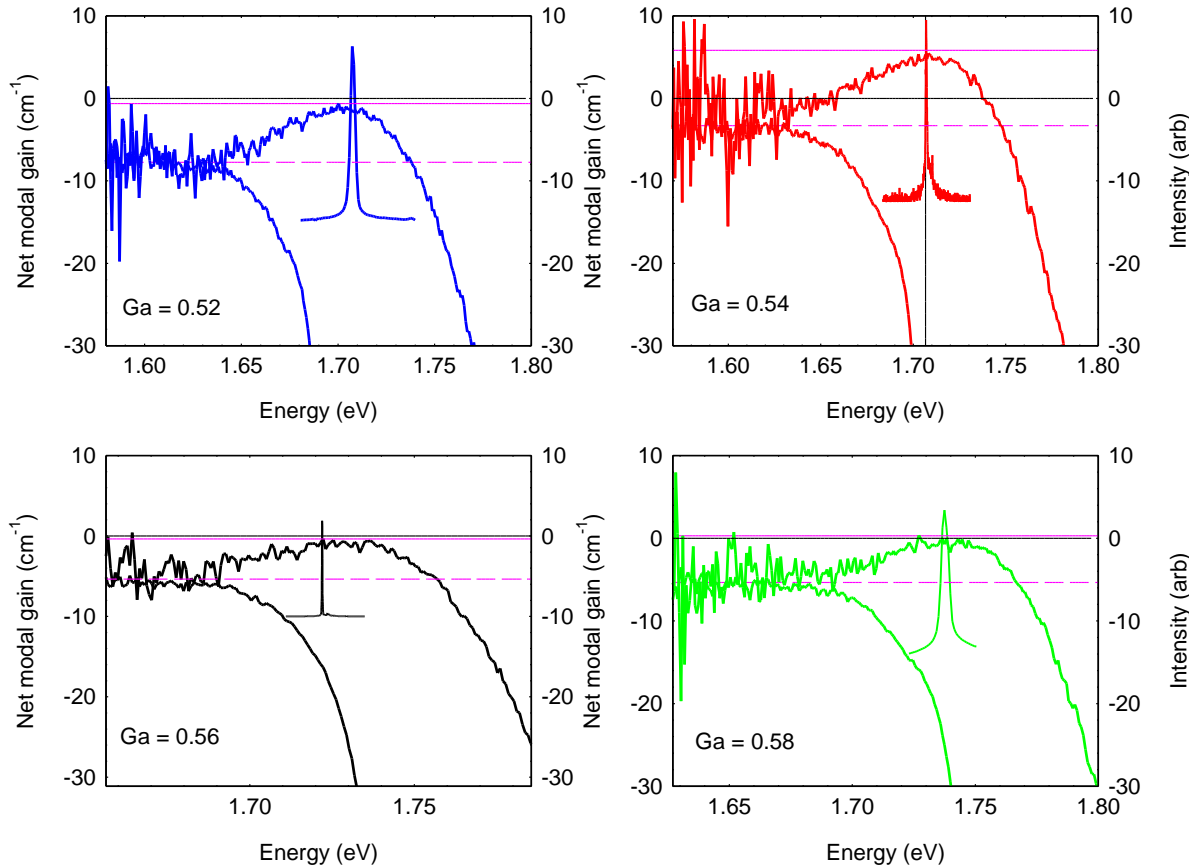


Figure 4.12(c): Net modal gain and net modal absorption spectra of the segmented contact device measured at 300 K and at a current density corresponding to threshold of a 2mm long laser. A lasing energy of a 2-mm-long laser (in arbitrary units in y-axis) is added to the respective graph at 300 K. The difference between the pink solid and the dotted-line represents the value of the peak modal gain (G) of $6 \text{ cm}^{-1} + \alpha_i$ as described in Figure 4.12(a).

The selected segmented contact device needs to achieve current density corresponding to the peak net modal gain of 6 cm^{-1} for a 2-mm-long laser which lase at $199 \pm 15 \text{ Acm}^{-2}$ as indicated in Figure 4.12(b) at 300 K. For example in Figure 4.12(b), the segmented contact device 1 requires a current density between 196 to 208 Acm^{-2} . This is the current density to

achieve a peak net modal gain of 6 cm^{-1} for a 2-mm-long laser, for a good comparison as mentioned in Section 2.5 in Chapter 2.

Here I will use the fact that the peak net modal gain ($G - \alpha_i$) of a 2-mm-long laser, also known as the mirror loss (α_m), is 6 cm^{-1} at the threshold current density, which is based on the gain requirement calculation as mentioned in Section 2.5 in Chapter 2 and Sections 3.4 and 3.10.2 in Chapter 3. As expected, the calculated gain requirement indicates that the value of peak modal gain (G) has to be larger than 6 cm^{-1} given that α_i is non zero. In theory as illustrated in Figure 4.12(a), the peak net modal gain for a 2-mm-long laser (i.e. 6 cm^{-1}) is extracted from the value of the peak modal gain (G), measured at a current density corresponding to threshold and with the gain peak at the lasing energy of a 2-mm-long laser. Therefore, whatever value is left from this extraction, should be the value for the optical mode loss per unit length (α_i) as shown practically in Figure 4.12(b).

Figure 4.12(c) shows the measured value of the net modal gain for the current density corresponding to threshold for a 2-mm-long laser and the absorption spectra of the segmented contact devices of all the Ga composition in the UCL measured at 300 K. A lasing spectrum of a 2-mm-long laser is added to the respective Ga composition in the UCL (colour coded). Looking at the peak of the net modal gain ($G - \alpha_i$), as in the example of Ga = 0.54, one would expect the lasing energy to coincide very close to the peak of the net modal gain curve (Smowton and Blood 2010), which seems to be true within the experimental uncertainty.

The pink horizontal dotted-line represents the optical mode loss (α_i) and the pink horizontal solid line represents the peak net modal gain - corresponding to the loss requirement for lasing as shown in Figure 4.12(c) for each gallium composition in the UCL. Basically α_i was determined at the low energy photon as mentioned in the previous Section 4.7.1. However, all the Ga composition have peak net modal gain ($G - \alpha_i$) below or at zero per unit length, except for G = 0.54. There is an obvious shift of the net modal absorption ($A + \alpha_i$) and net

modal gain ($G - \alpha_i$) spectra when compared to the net modal gain of 6 cm^{-1} . However the value of G is always larger than 6 cm^{-1} . In the next section, the behaviour of the different Ga composition in the UCL samples as a function of temperature is investigated.

4.7.2 Measurement as a function of temperature

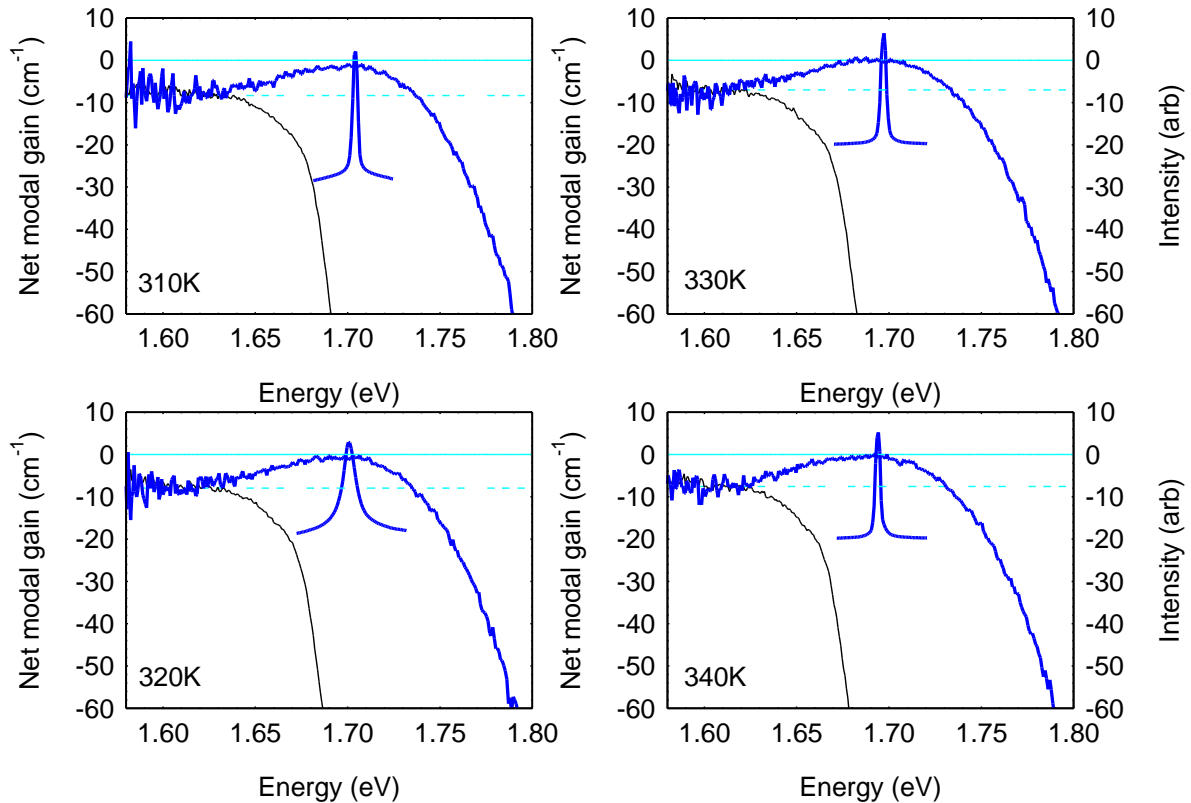


Figure 4.13: Net modal gain and net modal absorption spectra of the Ga = 0.52 segmented contact device measured at 310 – 340 K of Ga = 0.52. The lasing wavelength energy taken at the same temperature for a 2-mm-long laser of Ga = 0.52 is added to the respective graphs. The difference between the blue solid and the dotted-line represents the value of the peak modal gain (G) at 6 cm^{-1} as described in Figure 4.12(a).

The result in Figure 4.13 shows the relationship between the measurements of the Ga = 0.52, segmented contact samples measured at a current density corresponding to threshold for a 2-mm-long laser and the lasing energy at 310K – 340K. From these results, the lasing energy of the laser lies consistently close to the peak net modal gain of the segmented contact

measurement at different temperatures. Not only that, the value of the peak modal gain (G) at the gain requirement for each $G_a = 0.52$ in this example, shows consistency at each temperature, in this case, the average value of the peak modal gain ($G = 7.08 \pm 0.31 \text{ cm}^{-1}$).

4.8 Current density match, modal Gain (G) and optical mode loss value (α_i)

The measurement of the optical mode loss per unit length for the different G_a composition in the UCL is studied in this section.

4.8.1 Net modal absorption and modal gain

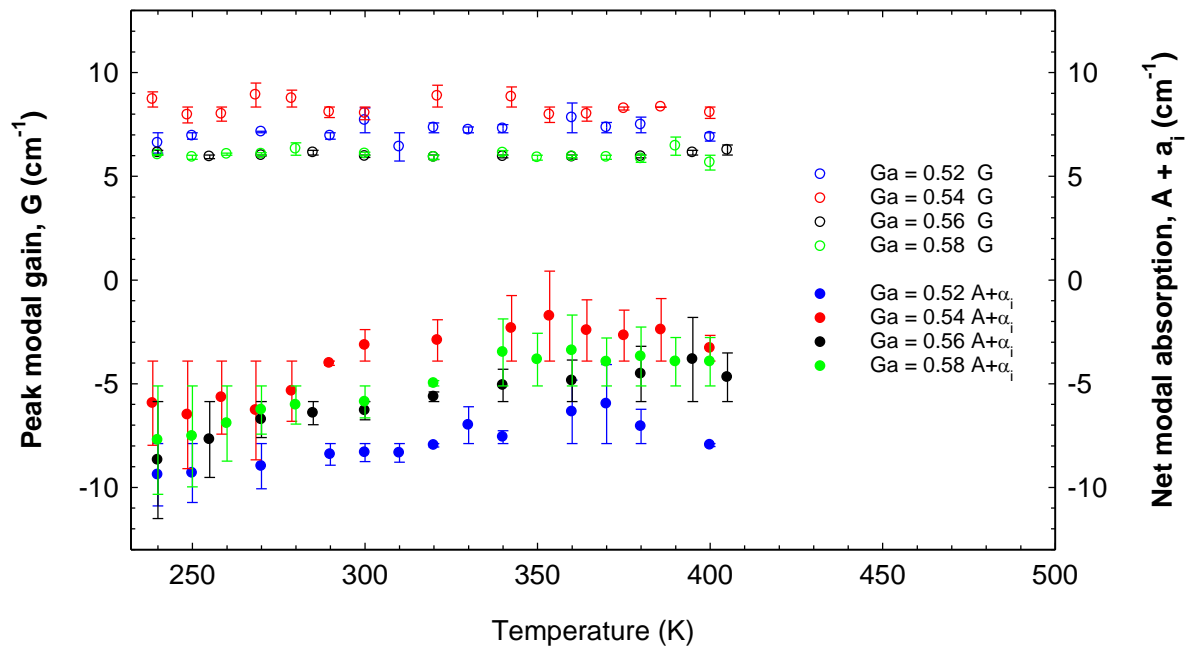


Figure 4.14: The net absorption and peak modal gain as a function of temperature. Related error-bars are included for uncertainty.

Figure 4.14 shows the net modal absorption ($A + \alpha_i$) and the peak modal gain (G) for each sample. In determining α_i at the value to which loss ($A + \alpha_i$) and gain ($G - \alpha_i$) spectra tend at low photon energy as illustrated in Figure 4.12(a), has not only introduced a large error but also indicates that the net modal absorption is temperature dependent in the case of these G_a

compositions. The measurement is also susceptible to experimental uncertainty and a systematic error due to sample alignment as shown in Figure 4.14. However, this is quite different to the measurement of the average peak modal gain (G) at the current density necessary to achieve threshold in a laser as clearly indicated in Section 4.7.2, where the error is smaller and the value of peak modal gain is fairly constant, even at different temperatures as shown in Figure 4.14. The value of the optical mode loss per unit length (α_i) is determined by subtracting 6 cm^{-1} from the average G for each sample in Figure 4.14 and the result is tabulated in Table 4.1.

4.8.2 The Optical Mode Loss Value

| Percentage of $\text{Ga}_{(x)}\text{In}_{(1-x)}\text{P}$ upper confinement layers (%) | Average Modal Gain, G (cm^{-1}) | Average optical mode loss per unit length. α_i (cm^{-1}) |
|---|--|--|
| 52 | 7.10 ± 0.30 | 1.10 ± 0.30 |
| 54 | 8.30 ± 0.30 | 2.30 ± 0.30 |
| 56 | 6.03 ± 0.20 | 0.03 ± 0.20 |
| 58 | 6.02 ± 0.40 | 0.02 ± 0.40 |

Table 4.1: The average modal gain with optical mode loss per unit length as a function of Gallium concentration in the UCL for a 2-mm-long lasers.

The optical mode loss per unit length (α_i) was discussed in the Section 4.7.2 which shows that extracting the net modal gain ($G - \alpha_i$) value of 6 cm^{-1} from the averaged value of the modal gain (G) will give the optical mode loss per unit length (α_i) as shown in Table 4.1. The technique of finding out the optical mode loss per unit length (α_i) using the average value of modal gain (G) as mentioned in Section 4.7.2 is more accurate and significant than

determining α_i at the value which loss ($A + \alpha_i$) and gain ($G - \alpha_i$) spectra tend to at low photon energy as previously illustrated in Figure 4.12(a).

4.8.3 Net modal gain and laser

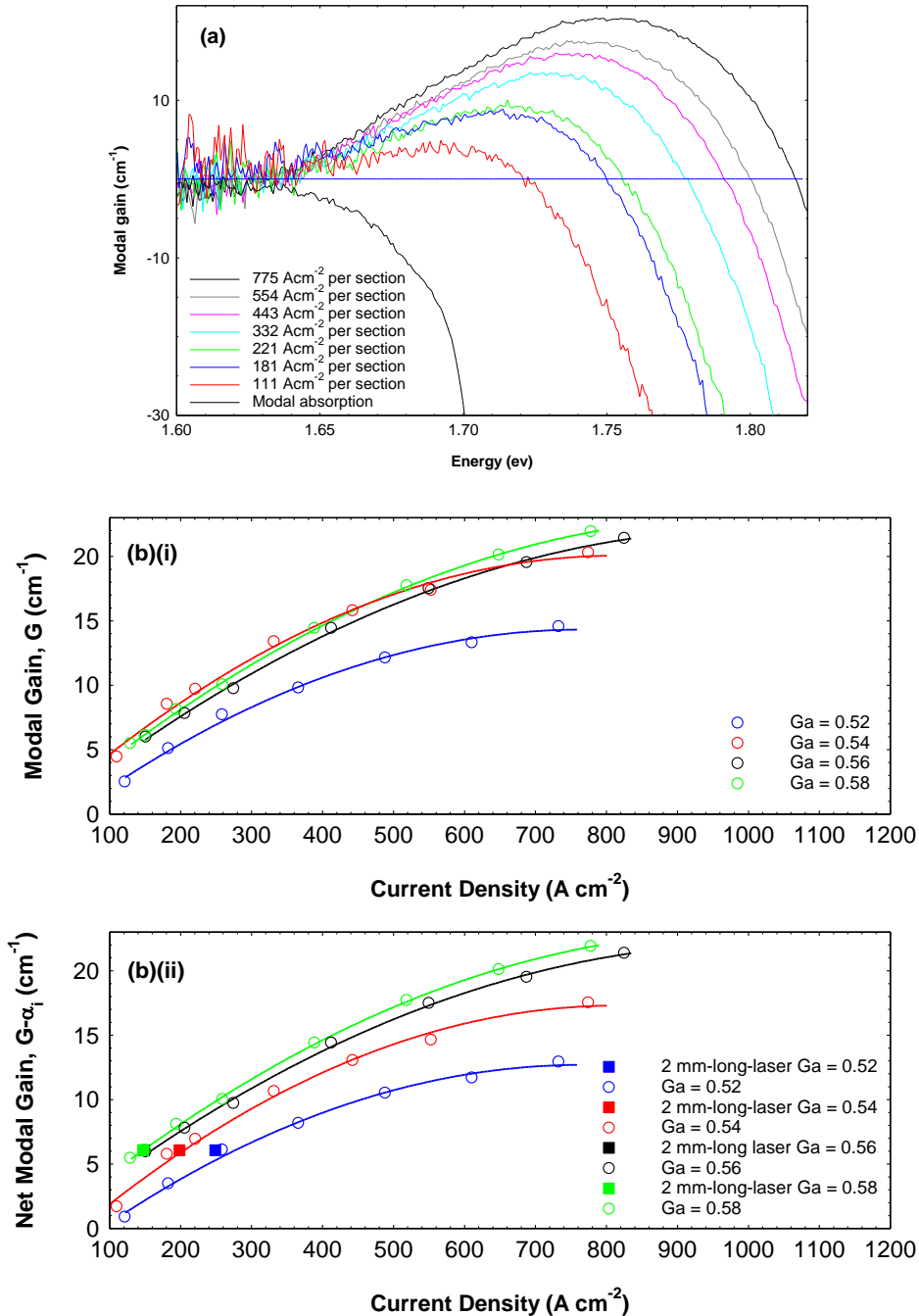


Figure 4.15: (a) The modal gain (G) as a function of current density at 300 K for $G_a = 0.54$. (b)(i) The modal gain (G) as a function of current density at 300 K (open circles). (b)(ii) The full squares represent 2-mm-long laser threshold current densities of the different G_a compositions in the UCL with calculated net modal gain ($G - \alpha_i$) of 6 cm^{-1} at 300K.

Figure 4.15(a) shows the modal gain (G) as a function of energy at 300 K. In the modal gain measurement the sample was pumped at different levels of current density, including the current density (181.0 Acm^{-2}) to achieve peak modal gain of 6 cm^{-1} for a 2-mm-long laser for $G_a = 0.54$. The modal gain increases with increasing current density. Figure 4.15(b)(i) shows the peak modal gain as a function of current density, the modal gain increases with increasing current density for all the gallium composition. The modal gain (G) is comparable for all, except at $G_a = 0.52$, which is at a lower modal gain and has a high current density requirement than the rest and this is consistent with the discussion of the absorption spectra in section 4.4. Figure 4.15(b)(ii) shows the net modal gain of the segmented contact measurement ($G - \alpha_i$), which is the value necessary to achieve lasing and therefore relevant for laser operation, is higher at fixed current density for $G_a = 0.56$ and 0.58 because α_i is lower for these samples.

4.9 Gain and Absorption spectra

Before considering these spectra in detail I need to describe the temperature dependence of the absorption edge as mentioned in Section 2.9 in Chapter 2, which is shown in Figure 4.16(a). The absorption edge energy increases with temperature linearly for all the gallium compositions. Gradients are similar within the experimental uncertainty and the energy values change similarly to the Varshni equation (Equation 2.28) as mentioned in Chapter 2. Measurements of gain and absorption spectra taken with the segmented contact method as described in Section 2.9.1 in Chapter 2 at temperatures of 300 K and 360 K are shown in Figure 4.16(b) for $G_a = 0.52$ as an example. The whole segmented contact curves were shifted to 0 cm^{-1} for modal gain (G), this is done to accurately measure each transparency energy (E_{Trans}). The data in Figure 4.16(b) shows the base measurement of the modal gain and absorption spectra at the current density necessary to achieve peak net modal gain of 6 cm^{-1} at 300 K (blue

curves). Three measurements were made at 360 K (red curves): firstly the current density equivalent to the current density to achieve peak net modal gain of 6 cm^{-1} at 300 K. Secondly, the current density to achieve the inversion level of 300 K at 360 K and thirdly the current density to achieve peak net modal gain of 6 cm^{-1} at 360 K. Also shown are their respective absorption spectrum (red curve). The inversion level by definition is the difference between the transparency point energy (E_{Trans}) with the absorption edge energy (E_{Abs}) (Smowton and Blood 2010). Then, in order to compare the change in the inversion level with the change of temperature, all the gain and absorption spectra were rigidly shifted by 23 meV (which was the shift necessary to make the 300 K and 360 K absorption curves overlap) as mentioned in Section 2.9 in Chapter 2. This rigid shift follows the shift of the energy gap of these materials with temperature.

By using the same current injection ($J_{1360\text{K}} = J_{300\text{K}}$), neither the gain requirement nor the inversion level at 300 K is achieved in Figure 4.16(b). With the current injection increased to $J_{2360\text{K}}$, the same inversion level as at 300 K can be achieved at 360 K and, yet it is lacking the correct peak net modal gain of 6 cm^{-1} . It seems that at higher temperature, an even higher current density is needed ($J_{3360\text{K}}$) to achieve peak net modal gain of 6 cm^{-1} of a 2-mm-long laser. One would expect the peak gain to decrease for a given carrier density as the electrons and holes are distributed over more energy states at higher temperature. For a constant peak gain maintained in this experiment, a higher total carrier density is needed to achieve the same gain at higher temperature and this is due to two effects. The first is that as the temperature is increased there is more non-radiative recombination so the carrier density, as indicated by the inversion level, decreases, and secondly even with the same inversion level the gain is still reduced due to carrier spreading.

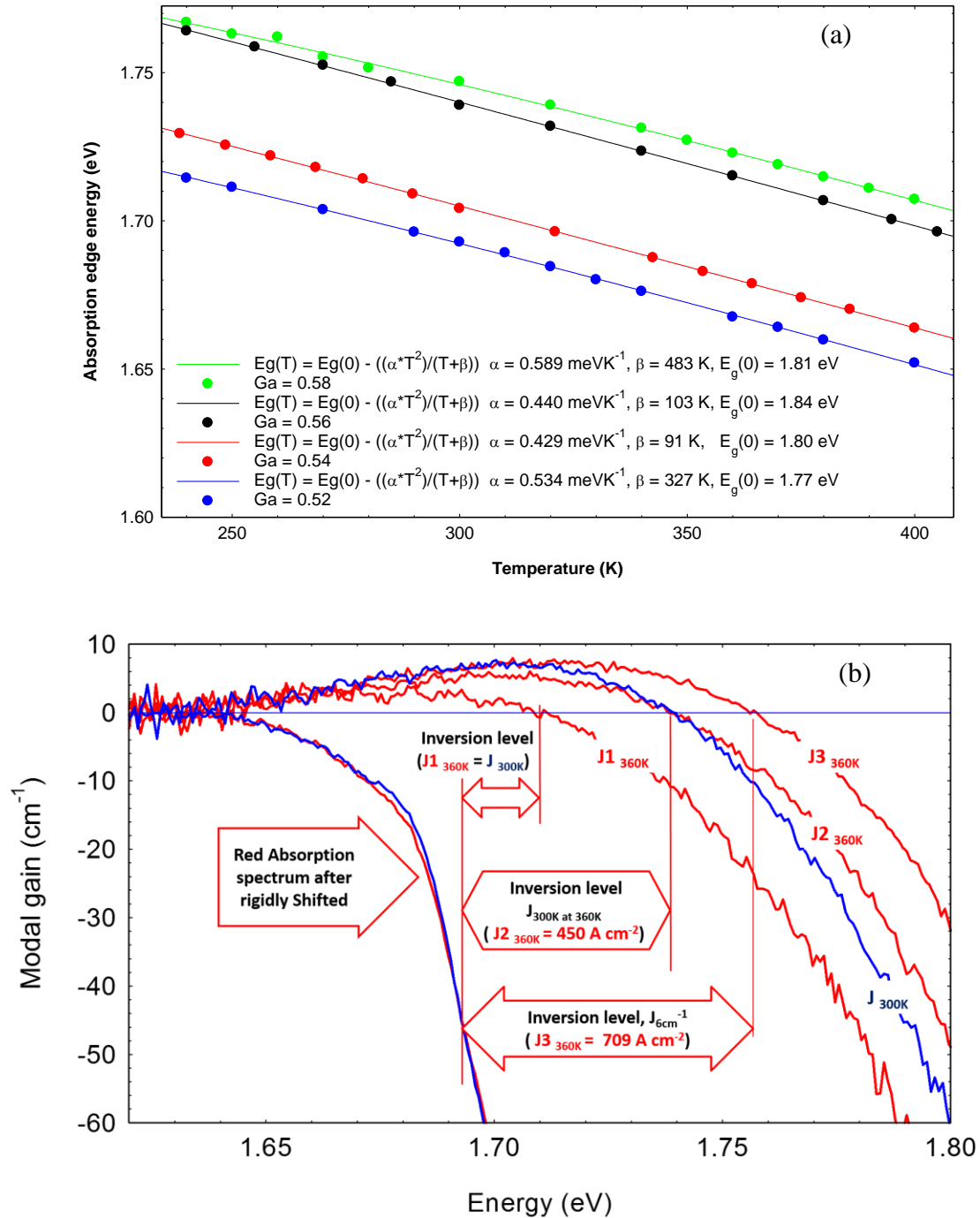


Figure 4.16: (a) The absorption edge energy as a function of different temperatures for all the gallium compositions. Lines of best fit according to Varshni equation as mentioned in Section 2 (Equation 2.28) were added to each curve. (b) Measurement of the modal gain spectra at (i) current density necessary to achieve peak net modal gain of 6 cm^{-1} at 360 K (J_{360K}), (ii) current density to achieve inversion level of 300 K at 360 K (J_{360K}) and (iii) current density at 360 K equivalent to the current density to achieve peak net modal gain of 6 cm^{-1} at 300 K ($J_{360K} = J_{300K}$), with their respective absorption spectra for $Ga = 0.52$. Then, a rigid shift was applied to the absorption and gain spectra (red curves) by 23meV to overlap with the current density at 300 K (blue curves). $Ga = 0.52$ was used as an example.

Using data obtained for the Ga = 0.52 sample as an example in Figure 4.16(b), the effects can be quantified. To maintain the peak modal gain of 300 K at 360 K, the current density requirement needed to achieve the same peak modal gain was 259 A.cm⁻² at 300 K, but to achieve the same peak gain at 360 K, a current density of 709 A.cm⁻² is needed. To maintain the same inversion level at 360 K as at 300 K a current density of 450 A.cm⁻² is required. The transparency energy at the point where the gain crosses the horizontal blue line in the Figure 4.16(b), which can be associated with the quasi-Fermi level separation for a system in thermal equilibrium, does show a substantial increase for the 360 K data when the current density is set at 709 A.cm⁻² to maintain the same peak gain.

4.10 Temperature dependence of threshold current density

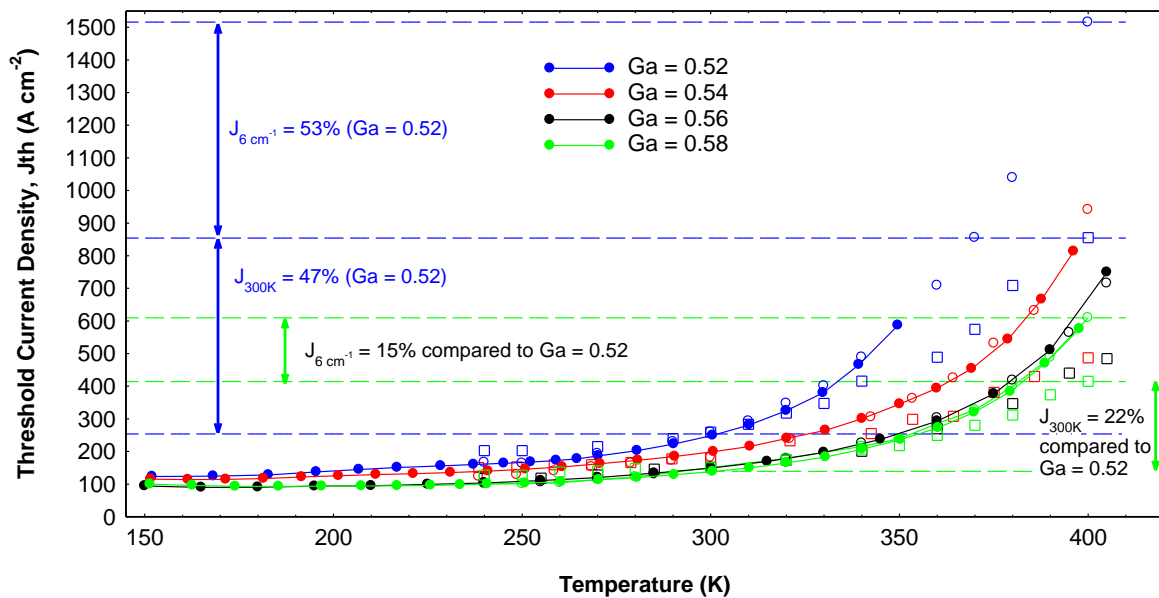


Figure 4.17: Laser measurement: The threshold current density of 2-mm-long lasers as a function of temperature for all Ga composition (closed circles). Segmented contact method measurement: Current density ($J_{6\text{ cm}^{-1}}$) to achieve peak modal gain of 6 cm⁻¹ (Open circles) and current density ($J_{300\text{K}}$) to achieve inversion level required at 300K at increasing temperature (Open squares).

Figure 4.17 shows the threshold current density for a 2-mm-long laser as a function of temperature and Ga composition in the UCL. Figure 4.17 also shows the current density ($J_{6\text{ cm}^{-1}}$

¹⁾ that is necessary to achieve a peak net modal gain of 6 cm^{-1} (opened-circle) and then current density ($J_{300\text{K}}$) to achieve the corresponding inversion level of 300 K at 240 – 400 K, both as a function of temperature as previously explained. The data for the current density to achieve a peak net modal gain of 6 cm^{-1} agrees with the threshold current density from laser measurements as would be expected. The value of the segmented contact technique is to separate out the effect of the increased inversion level and the increased current density required to compensate for the increased carrier spreading from other factors.

Table 4.2 shows that $G_a = 0.52$ at 100 % current density ($J_{6\text{cm}^{-1} \text{ at } 400\text{K}} - J_{6\text{cm}^{-1} \text{ at } 300\text{K}}$) is reduced, in terms of temperature dependence of threshold current down to 37 % as G_a composition increases to $G_a = 0.58$. There is a clear reduction of the current density to achieve inversion level at 300 K at 400 K ($J_{300\text{K inversion level}} - J_{6\text{cm}^{-1} \text{ at } 300\text{K}}$) from 47 % ($G_a = 0.52$) down to 22 % of $G_a = 0.58$. Furthermore, there is an even clearer reduction of the additional current density to achieve a peak net modal gain of 6 cm^{-1} at 400 K ($J_{6\text{cm}^{-1} \text{ at } 400\text{K}} - J_{300\text{K inversion level}}$) from 53 % ($G_a = 0.52$) down to 15 % of $G_a = 0.58$ at higher inversion level. It is also clear that whereas the carrier spreading effect is larger for the $G_a = 0.52$ sample, the non-radiative recombination effect is larger for the $G_a = 0.58$ sample. Let us investigate further the $J_{300\text{K}}$ and $J_{6 \text{ cm}^{-1}}$ as a function of temperature in the next section.

| Ga | Percentage (%) | | |
|------|---|---|---|
| | $J_{6\text{cm}^{-1} \text{ at } 400\text{K}} - J_{6\text{cm}^{-1} \text{ at } 300\text{K}}$ | $J_{300\text{K inversion level}} - J_{6\text{cm}^{-1} \text{ at } 300\text{K}}$ | $J_{6\text{cm}^{-1} \text{ at } 400\text{K}} - J_{300\text{K inversion level}}$ |
| 0.52 | 100 | 47 | 53 |
| 0.58 | 37 | 22 | 15 |

Table 4.2: Percentage of current densities to achieve peak net modal gain ($J_{6 \text{ cm}^{-1}}$), difference between $J_{6\text{cm}^{-1}} - J_{300\text{K inversion level}}$ and difference between $J_{300\text{K inversion level}} - J_{6\text{cm}^{-1} \text{ at } 300\text{K}}$ for $G_a = 0.52$ and 0.58 taken at temperature between 300 – 400K.

4.11 Current density as a function of temperature at 300 K inversion level

The effect of temperature on inversion level is studied in this section. This section is divided into three parts, first the current density to achieve inversion level required at 300K as

a function of temperature, then the inversion level at temperatures of 240K, 300K and 360K, lastly the current density to achieve a fixed inversion level as a function of temperature.

4.11.1 Current density to achieve the same inversion level as 300K

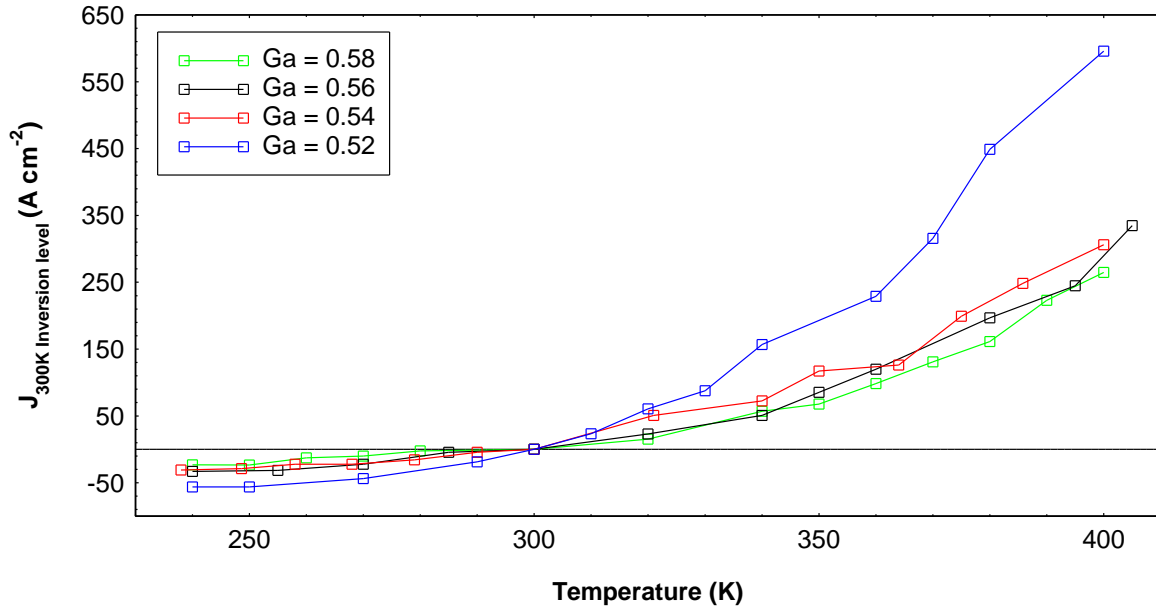


Figure 4.18: Current density to achieve the same inversion level required at 300K as a function of temperature extracted from Figure 4.17.

Figure 4.18 shows the current density to achieve the same inversion level required at 300 K as a function of temperature, extracted from the Figure 4.17. The measurement of the current density to achieve the inversion level of 300 K was started around 240 K, where thermally activated leakage is minimised. As expected between 240 K to 280 K the current density is almost constant since processes such as non-radiative recombination are relatively constant at these temperatures. Above 280 K the current density to achieve the 300 K inversion level starts to increase, most likely due to the thermal activated leakage (Smowton and Blood 2010) as mentioned in Section 2.6 in Chapter 2. Nonradiative recombination is the main cause of thermally activated leakage in real index guided laser structures reported by Dutta et al.

(1984). All the Ga compositions are comparable in J_{300K} inversion level except for $Ga = 0.52$, which is at a higher value.

4.11.2 Inversion level with current density

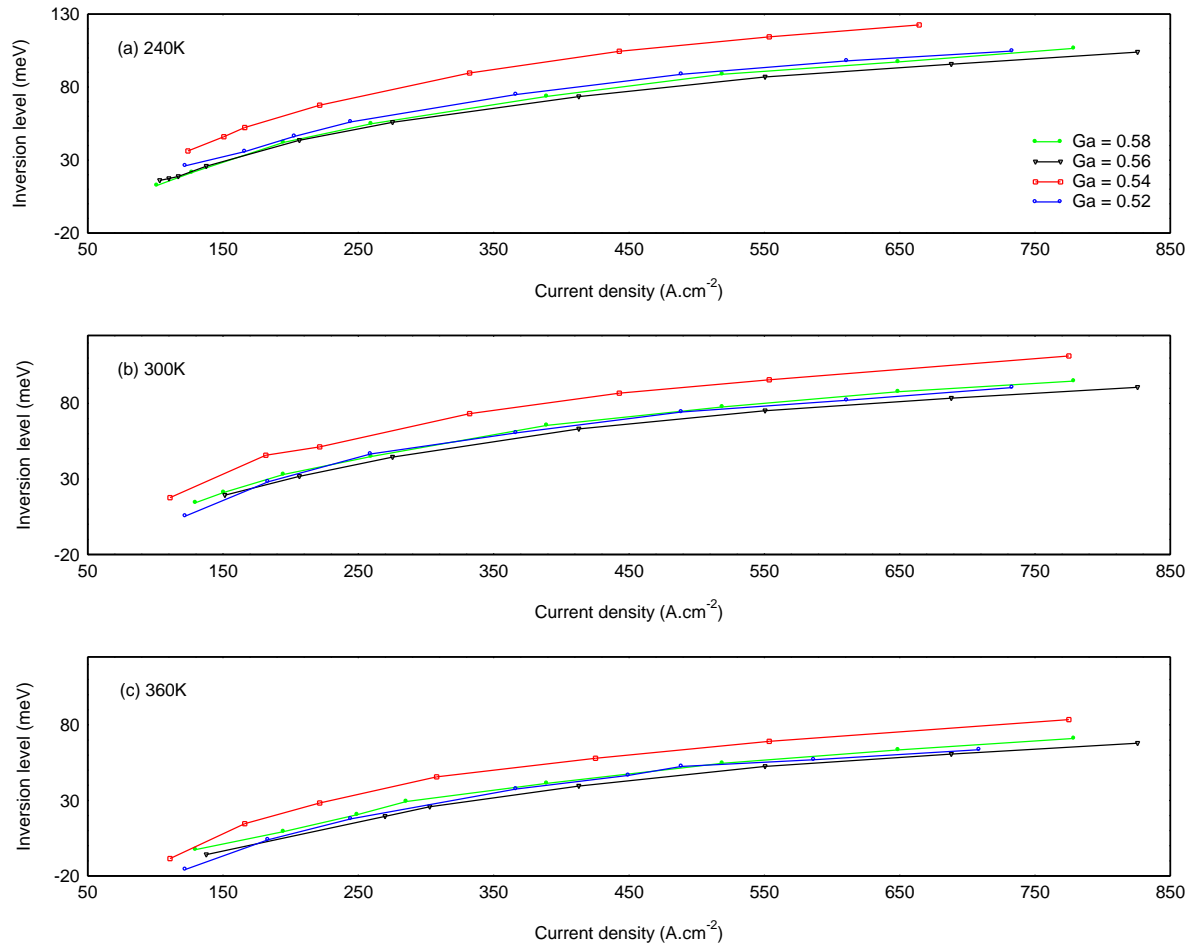


Figure 4.19: Inversion level as a function of current density at (a) 240 K. (b) 300 K and (c) 360 K for all the gallium compositions.

Figure 4.19 shows the inversion level as a function of current density measured at 240 K, 300 K and 360 K for all the gallium compositions. In general all the gallium concentration show a more rapid increase of inversion level at a low current densities, then a gradual levelling off to a saturated inversion level at larger current density. Figure 4.19 at 240 K shows all the gallium compositions had almost the same inversion level at the same current density, except

for the Ga = 0.54, which is at a higher inversion level, the trend is similar for temperature at 300 K and 360 K. The higher inversion level for Ga = 0.54 indicates it is intrinsically better as was suggested in section 4.4 where it had the best defined and larger magnitude absorption peak. The fact that it is a poorer laser is probably due to the larger α_i as shown in table 4.1 and needs higher inversion level to achieve the necessary gain requirement, hence higher threshold current density.

4.11.3 Current density at a fixed inversion level

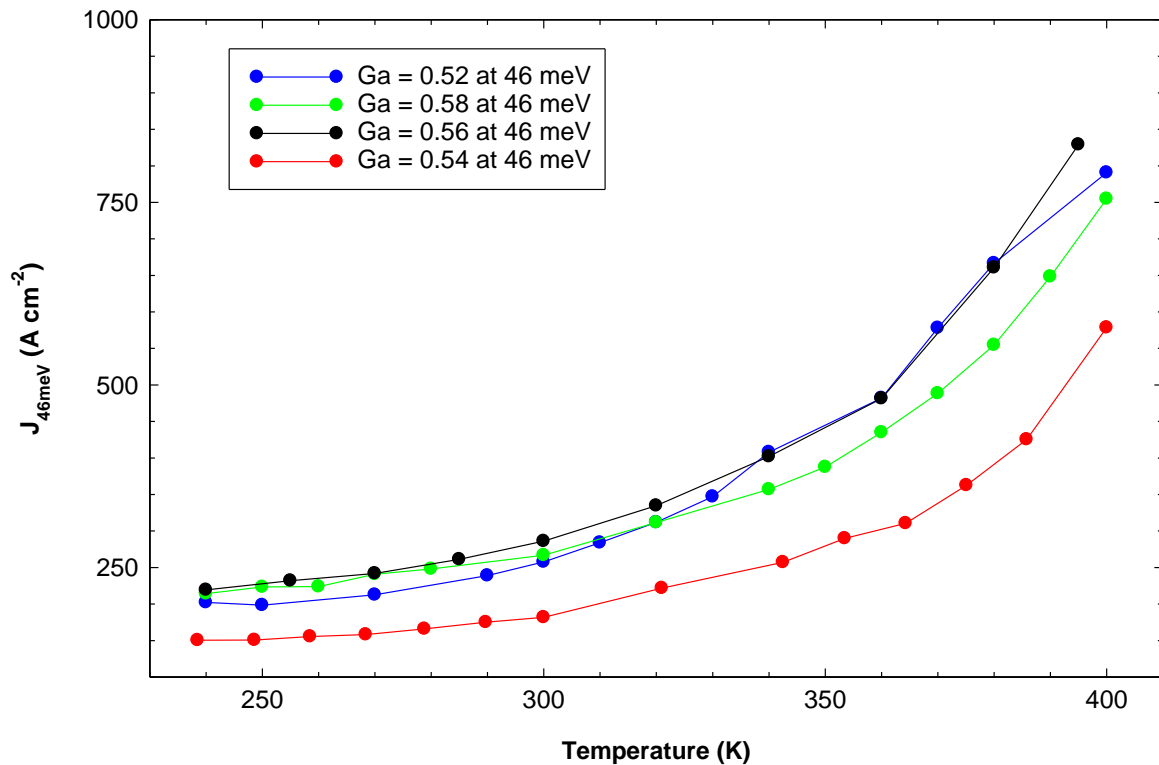


Figure 4.20: the current density at a fixed inversion level (46 meV) as a function of temperature for different Ga composition.

To examine whether the higher temperature dependence of the Ga = 0.52 sample in Figure 4.18 is due to a property of Ga = 0.52 or simply because the inversion level is higher for this sample due to high α_i , I consider a fixed inversion level. Current density for a fixed inversion level of 46 meV for all the available temperatures is plotted in Figure 4.20. The

graph shows a fairly comparable current density at a fixed value of 46 meV at increasing temperature for all Ga composition, except at Ga = 0.54 which has an obviously lower current density. This supports the understanding Ga = 0.54 has a better material quality, which clearly shown by its lower current density, and very likely the reduced threshold current density in Figure 4.17 for the 0.56 and 0.58 Ga compositions were due to their lower α_i values as indicated previously in Table 4.1. Ga = 0.52 is not intrinsically poorer than 0.56 or 0.58 with regard to the recombination rate at fixed inversion level.

4.12 Higher inversion and inversion level at a fixed gain as a function of temperature

The effect of temperature at higher inversion level and inversion level at a fixed gain is studied in this section. This section is divided into two parts, the first considers the current density to achieve higher inversion level as a function of temperature and the second the inversion level necessary to achieved a fixed peak net modal gain as a function of temperature.

4.12.1 Changes in current density to achieve higher inversion level

There is a clear reduction of additional current density to achieve a peak net modal gain of 6 cm^{-1} with increasing Ga composition in Figure 4.21. The difference in current density between $J_{6\text{cm}^{-1}}$ and $J_{300\text{K inversion level}}$ extracted for the available temperatures for each gallium composition, to verify the affect of carrier spreading at higher inversion level is shown in Figure 4.21. At higher temperature, current density decreases at increasing Ga composition with Ga = 0.56 and 0.58 almost comparable. This reflects that an excess of current density is required to achieve a peak net modal gain of 6 cm^{-1} at higher inversion level, which is due to the carrier spreading at high energy states. This indicates how carrier spreading can have a huge impact on the gain requirement in QD structures.

An increase of threshold current density is needed at higher temperature to achieve peak net modal gain at 6 cm^{-1} for a 2-mm-long laser. It is needed to compensate for the carrier spreading, within higher energy states of the broadening gain spectrum. The higher Ga composition significantly reduces this effect. It is clearly shown that increasing the gallium composition in the upper confining layer of the QW can have a huge impact in reducing the current density in Figure 4.21.

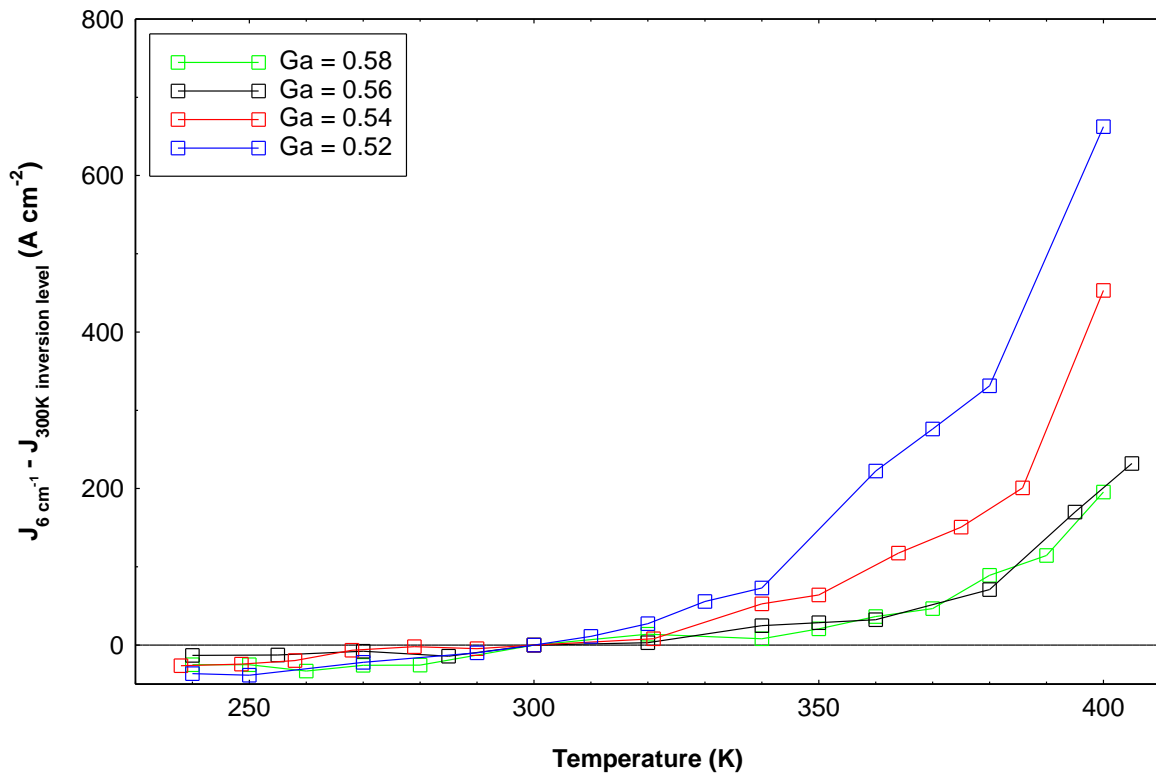


Figure 4.21: Difference in current density between $J_{6 \text{ cm}^{-1}}$ and $J_{300 \text{ K inversion level}}$ as a function of temperature extracted from Figure 4.17 to show current spreading at higher inversion level.

4.12.2 Inversion level to achieve a fixed peak net modal gain

The inversion level, defined as the difference between quasi-Fermi level separation required and the absorption edge, and the value to achieve a peak net modal gain of 6 cm^{-1} are plotted in Figure 4.22. In general all the graph with straight line fit show a gradual increase of inversion level from 240 to 400K. For example at 300K, Ga = 0.52 and 0.54 are both at 46 meV, while Ga = 0.56 and 0.58 are 19 meV and 21 meV, respectively. The sample with Ga =

0.56 has the lowest rate of change of inversion level as a function temperature. The increasing inversion level reflects the the fact that as temperature increased, spreading of the carriers is also increased in the available states, meaning the materials must be driven to higher inversion level or correspondingly higher carrier density to achieve the same peak gain (Smowton et al. 2011).

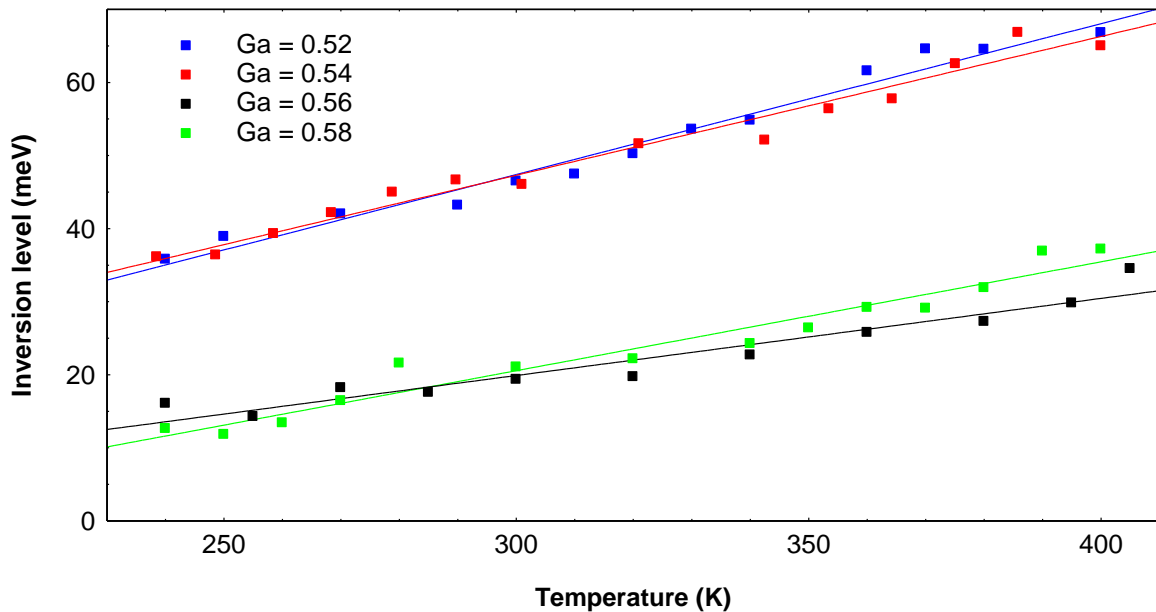


Figure 4.22: Inversion level necessary to achieve a peak modal gain of 6 cm^{-1} as a function of temperature.

4.13 Gain requirement as a function of temperature

The effect of temperature on the gain requirement at different inversion levels is studied in this section. This section is divided into two parts, first the gain requirement at the 300 K inversion level for each sample as a function of temperature, followed by the gain requirement at a fixed inversion level as a function of temperature.

4.13.1 Gain requirement at 300 K inversion level

The effects of carrier spreading on gain peak can be observed more directly. Figure 4.23(a) shows the peak net modal gain for the inversion level required to achieve 6 cm^{-1} at 300

K as a function of temperature. The peak net modal gain ($G - \alpha_i$) decreases as temperature increases at the same inversion level for all the Ga composition. However, since the α_i values are different, the peak gains achieved in the samples are different as shown in Figure 4.23 (b) and this may cause the differences in temperature dependence seen. Therefore in Figure 4.24, the gain at a fixed inversion level of 46 meV is plotted as a function of temperature.

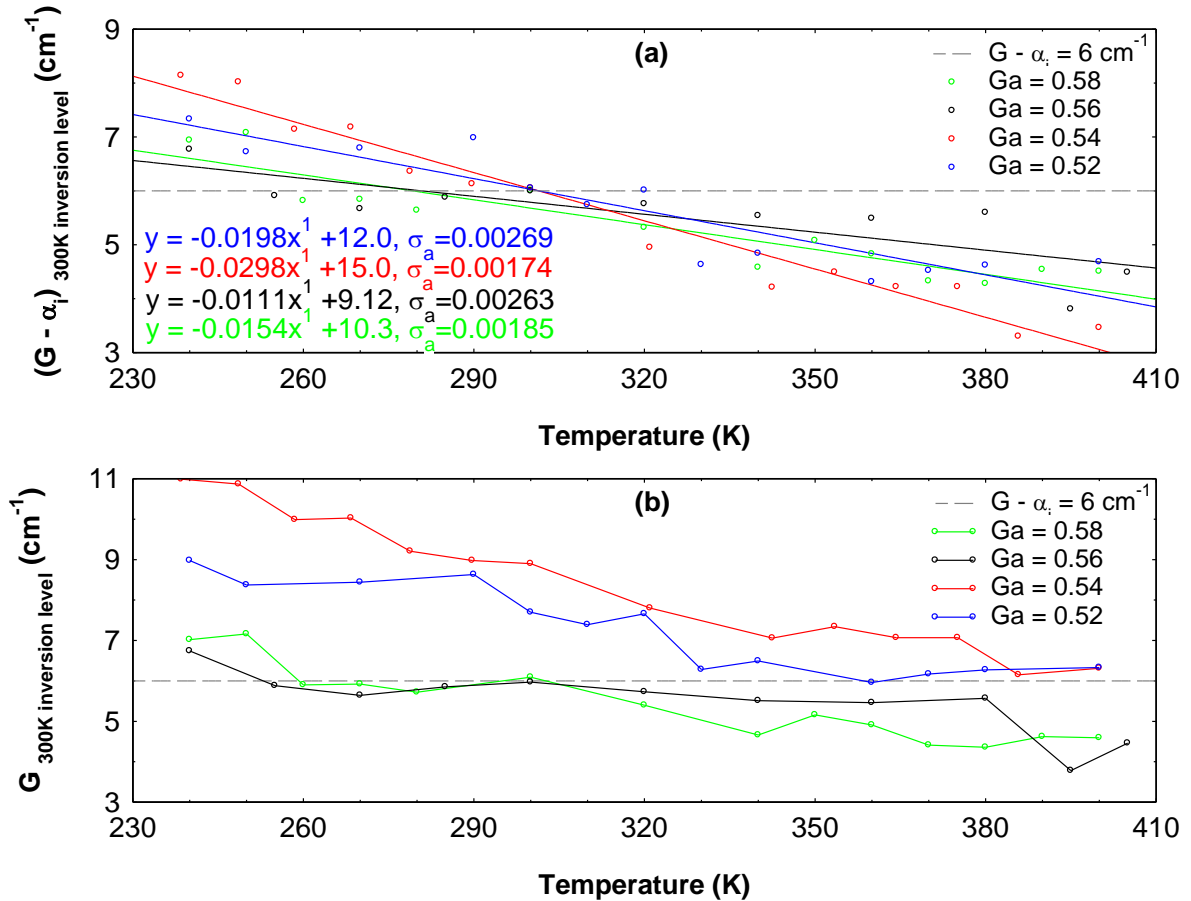


Figure 4.23: (a) Peak net modal gain ($G - \alpha_i$) at the inversion level requirement of 300 K as a function of temperature for all the Ga compositions with lines of best fit for all the Ga compositions. (b) Peak modal gain (G) at the inversion level requirement of 300 K as a function of temperature for all the gallium compositions. The grey dotted line indicates the mirror loss ($G - \alpha_i$) of 6 cm^{-1} .

4.13.2 Gain requirement at a fixed inversion level

Again, the peak modal gain decreases as temperature increases. At a 46 meV inversion level, the Ga = 0.56 and 0.58 have higher peak modal gain compared to the Ga = 0.52 and 0.54. The temperature dependence is now similar for the Ga = 0.54 – 0.58 samples and even less

pronounced for the Ga = 0.52 sample indicating that the larger temperature dependence seen for Ga = 0.52 and 0.54 in Figure 4.22 and 4.23 is simply a result of the higher α_i values of these samples.

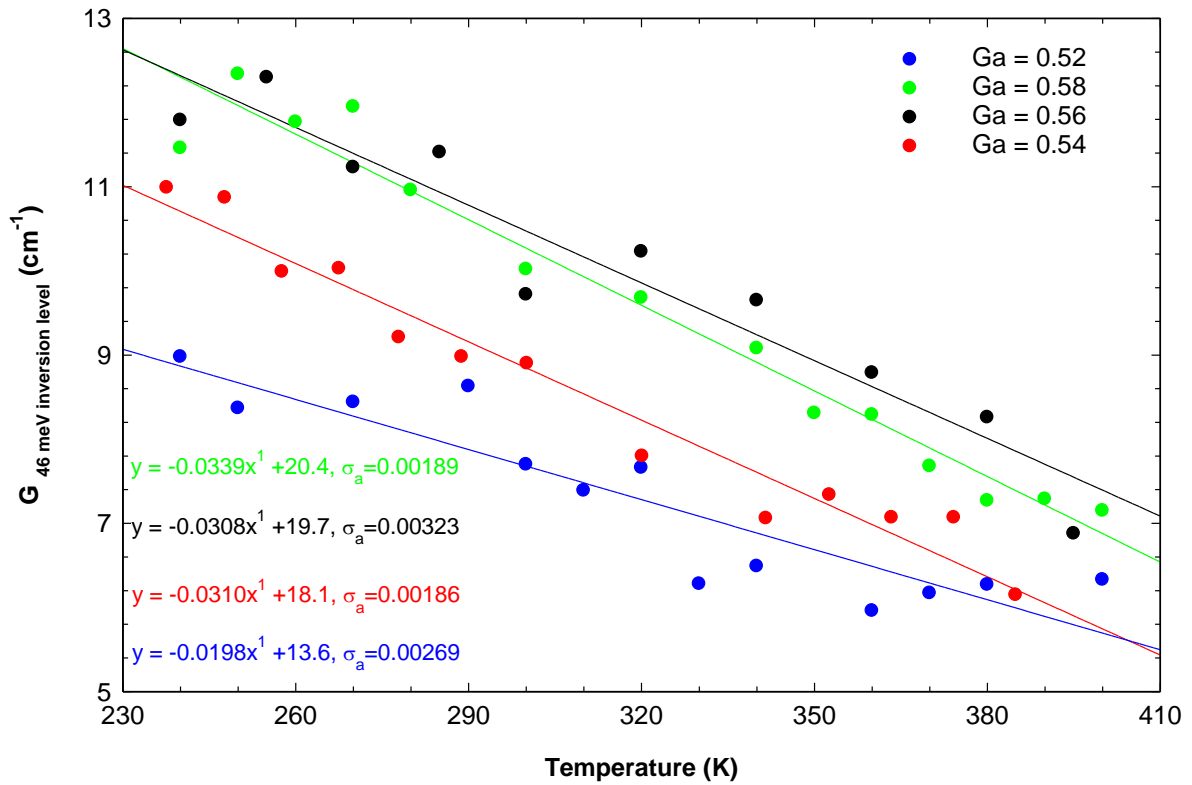


Figure 4.24: Peak modal gain at a fixed inversion level (46 meV) as a function of temperature for different Ga compositions.

4.14 Unamplified spontaneous emission

The unamplified spontaneous emission (mentioned in Section 3.11 in Chapter 3) from data of Figure 4.17 is studied in this section. This section describes three parts. First the comparison of unamplified spontaneous emission at the current density to achieve a peak net modal gain of 6 cm^{-1} as a function of energy and temperature. Second the unamplified spontaneous emission at current density at a fixed inversion level as a function of energy and temperature. Lastly, comparison of the rate of spontaneous emission between current density at a fixed peak net modal gain of 6 cm^{-1} and inversion level as a function of temperature for Ga = 0.54 and 0.58.

4.14.1 Unamplified spontaneous emission at a fixed peak net modal gain

Figure 4.25 shows the unamplified spontaneous emission rate spectra as a function of energy at different temperatures for Ga = 0.54 and 0.58 at a current density to achieve peak net modal gain of 6 cm^{-1} (threshold for a 2-mm-long laser). In general there are two main peaks for each Ga composition; the low energy peaks represent the quantum dots states while the high energy peaks correspond to the GaInP quantum well states as mentioned by Al-Ghamdi (2009).

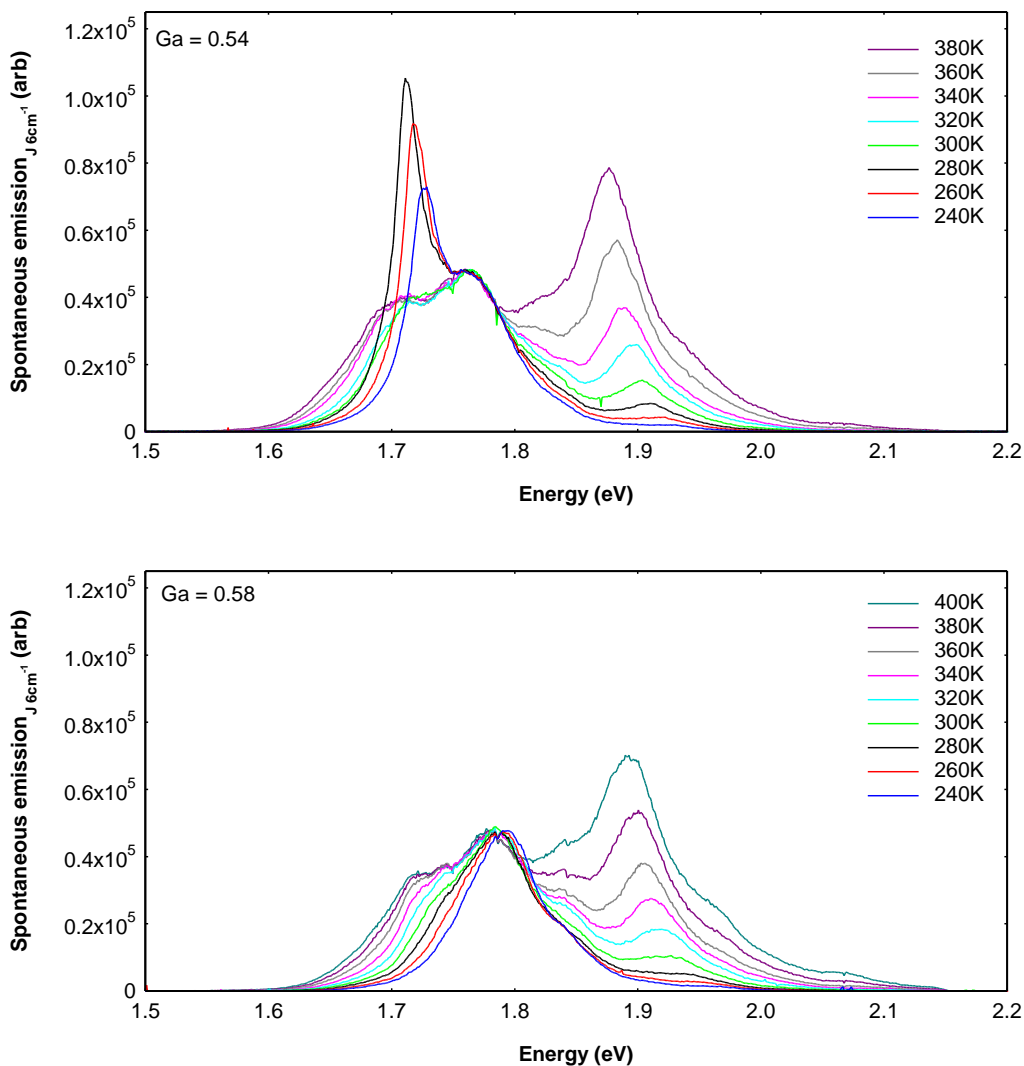


Figure 4.25: Spontaneous emission spectra measured at threshold current density as a function of temperature.

Based on these data, the recombination associated with the quantum dots (area under the first peak) increases approximately linearly with increasing temperatures, whereas that associated with the quantum wells increases at a much faster rate (area under second peak). Although the experiment was carried out as carefully as possible with the correct alignment as mentioned in Section 3.11 in Chapter 3, unfortunately there is still some stimulated emission scattered vertically and appearing below 300K and seen at approximately 1.72 meV in the upper figure. Yet this measurement is still significant in clarifying the unamplified spontaneous emission for characterisation of the selected samples. The sample data in Figure 4.25 is normalised at the peak quantum dot value of 1.76 meV and 1.78 meV for Ga = 0.54 and Ga = 0.58, respectively.

An important aspect of Figure 4.25, is the difference in amplitude of the curves near 2.1 eV. This energy corresponds to the bandgap of the lower confining layer (LCL). As we observe as the temperature increases, some of the energetic carriers from the quantum well (UCL) escape to the lower confining layer (LCL) and this happens more in the Ga = 0.58 than in the Ga = 0.54. Since the data is normalised at the QD energies, the QW rate of spontaneous emission as a function of temperature, gives a comparison of the occupation in the QD and QW states at a current density to achieve peak net modal gain of 6 cm^{-1} .

4.14.2 Unamplified spontaneous emission at a fixed inversion level

Figure 4.26 shows the unamplified spontaneous emission rate as a function of energy at different temperatures for Ga = 0.54 and 0.58 at current density for a fixed inversion of 46 meV. The existence of stimulated emission is still obvious in the Ga = 0.54 sample data. It is interesting to note that both spontaneous emission rates show an almost similar trend for the quantum dot and quantum well states. Again the leakage of more energetic carriers is seen in the LCL region at 2.1 meV, as apparent in Ga = 0.58. As the Ga composition increases the dot

and well states move to higher energy and closer to the LCL, which is at fixed energy as described in Section 2.4.2 in Chapter 2. Therefore at a fixed inversion level, the LCL will be more populated for $G_a = 0.58$ in principle. Thus again the normalised QD will be a useful comparison for these samples in terms of occupation in the QD and QW states at a current density at a fixed inversion level, which will be described next.

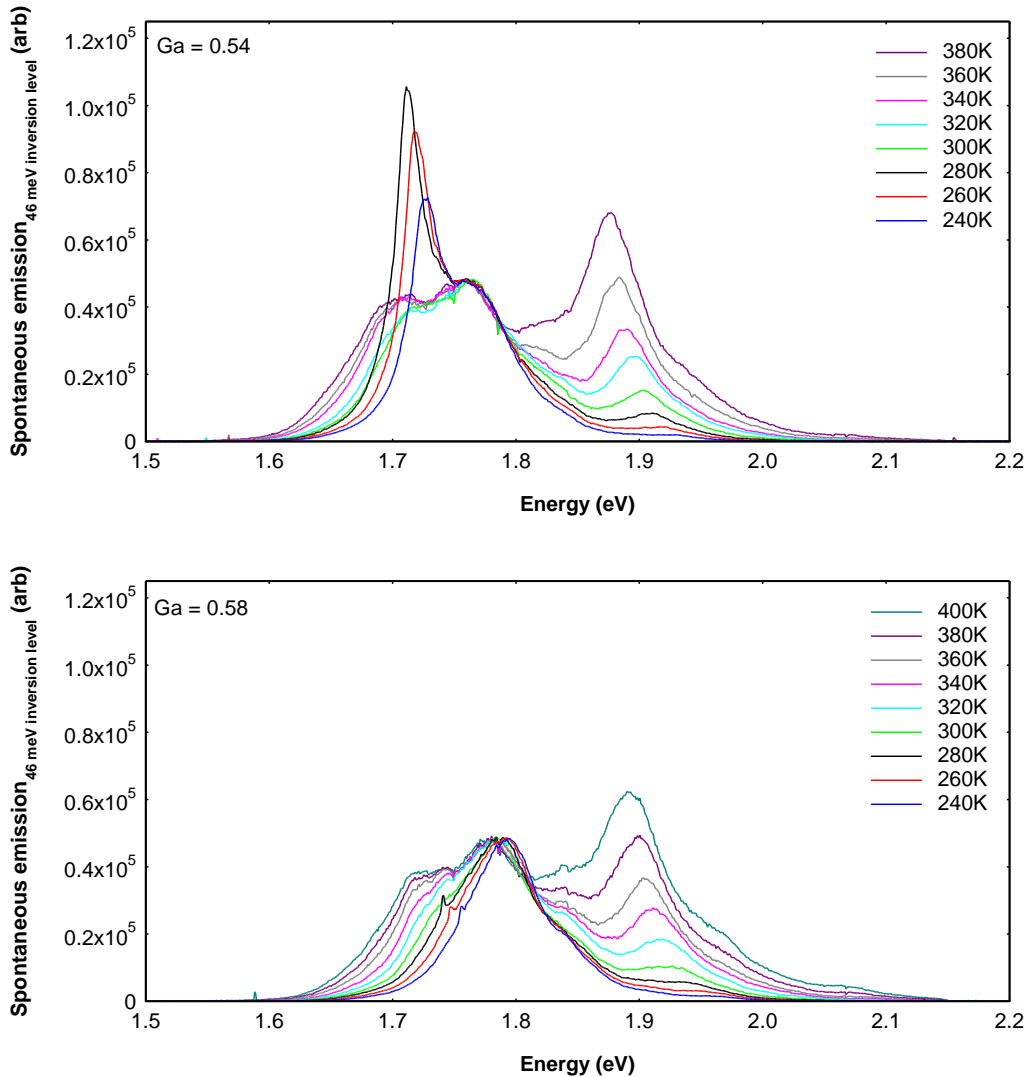


Figure 4.26: Spontaneous emission spectra measured at a fixed inversion level (46 meV) as a function of temperature.

4.14.3 Rate of spontaneous emission as a function of temperature

Figure 4.27 shows the rate of spontaneous emission corresponding to the emission from the QW for current density to achieve peak net modal gain of 6 cm^{-1} and the current density at

a fixed inversion level. The rapid increase of the rate of spontaneous emission when compared to the QW states in the $G_a = 0.58$ suggests that there are more filled QW states in the $G_a = 0.54$. This may be because more carriers are supplied to the $G_a = 0.54$ to compensate for its high optical mode loss (α_i), when compared to $G_a = 0.58$. This is apparent when we look at the almost equal rate of spontaneous emission in Figure 4.27 showing the current density for a fixed inversion level for $G_a = 0.54$ and 0.58 . Figure 4.27 shows $G_a = 0.54$ rate of spontaneous emission is slightly higher than the $G_a = 0.58$, which may be due to the incomplete removal of the stimulated emission for $G_a = 0.54$ as mentioned earlier in this section.

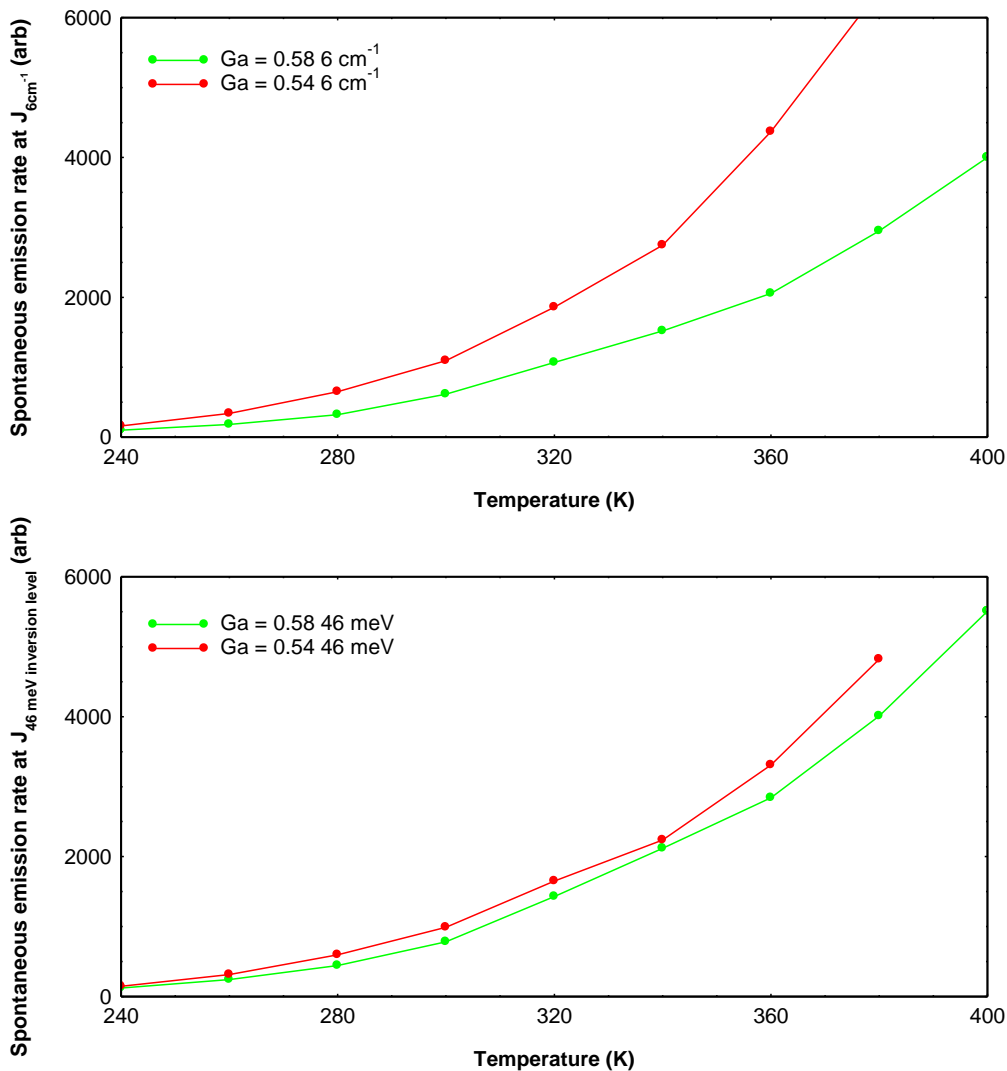


Figure 4.27: Spontaneous emission rate corresponding to the emission from the QW at $J_{6\text{cm}^{-1}}$ and at $J_{46\text{ meV inversion level}}$ as a function of temperature.

4.15 Summary

| Experiment | Result |
|---|--|
| 1. Characteristics of the wafers grown. | The differences that exist between samples of the same Ga compositions are due to random variation that is affecting the whole sample. |
| 2. Fundamental measurements. | It is established that there is no drastic change in the fundamental characteristics apart from the effects due to Ga composition. |
| 3. Introducing a new way of determining the mode loss per unit length (α_i) | Extracting the peak net modal gain ($G - \alpha_i$) value of 6 cm^{-1} from the averaged value of the modal gain (G) will give the optical mode loss per unit length (α_i). This technique is more accurate and significant than determining α_i at the value to which loss ($A + \alpha_i$) and gain ($G - \alpha_i$) spectra tend to at low photon energy. |
| 4. The value of current density to achieve a peak net modal gain of 6 cm^{-1} with the segmented contact method are expected to agree with the threshold current densities from laser measurements. | The value of the segmented contact technique is to separate out the effect of the increased inversion level and the increased current density required to compensate for the increased carrier spreading from other factors. For a constant peak gain to be maintained at higher temperatures, two effects must be considered. The first is that as the temperature is increased there is more non-radiative recombination so the carrier density, as indicated by the inversion level, decreases, and secondly even with the same inversion level the gain is still reduced due to carrier spreading. |
| 5. The current density to achieve the inversion level required at 300 K and the current density to achieve a fixed inversion level as function of | Above 280 K the current density to achieve the 300 K inversion level starts to increase, most likely due to the thermal activated leakage. The data shows a fairly comparable current density at a fixed value of 46 meV at increasing temperature for all Ga composition, except at Ga = 0.54 which has an obviously lower current density. This suggests Ga = 0.54 has a better material quality. The fact that it is a poorer laser is |

| | |
|---|--|
| <p>temperatures are examined.</p> | <p>probably due to the larger α_i necessitating a higher current density to achieve the required gain.</p> |
| <p>6. (a) The extra current density to achieve a peak net modal gain of 6 cm^{-1} compared to that required to achieve the 300K inversion level.</p> | <p>An increase in threshold current density is needed at higher temperature to achieve peak net modal gain at 6 cm^{-1} for a 2-mm-long laser. It is needed to compensate for the carrier spreading to higher energy states. The higher Ga composition significantly reduces this effect.</p> |
| <p>(b) The inversion level necessary to achieved a fixed peak net modal gain as a function of temperature is considered.</p> | <p>The increasing inversion level reflects the the fact that as temperature increases spreading of the carriers in the available states is also increases, meaning the materials must be driven to higher inversion level or correspondingly higher carrier density to achieve the same peak gain.</p> |
| <p>7. Gain decreases with temperature are studied directly.</p> | <p>The peak net modal gain for the inversion level required to achieve 6 cm^{-1} at 300K as a function of temperature decreases as temperature increases for all the Ga compositions. However, since the α_i values are different, the peak gains achieved in the samples are different and this causes the differences in temperature dependence. This was confirmed by showing the gain at the same fixed inversion level as a function of temperature for all samples.</p> |
| <p>8. The unamplified spontaneous emission at $J_{6 \text{ cm}^{-1}}$ and constant inversion level are studied.</p> | <p>Spontaneous emission rate spectra measured at $J_{6 \text{ cm}^{-1}}$ show more filled QW states for Ga = 0.54 compared to Ga = 0.58 and compared with data taken at constant inversion level indicates that more carriers are supplied to the Ga = 0.54 to compensate for its high optical mode loss (α_i), when compared to Ga = 0.58. As the temperature increases, some of the energetic carriers from the QW escape to the lower confining layer (LCL) and spontaneous emission measurements show this happens more in the Ga = 0.58 than in the Ga = 0.54.</p> |

Chapter 5

Comparison of Three Growth Series

5.1 Introduction

Three series of growth are compared in this section. There were 2 series (Series 1 & Series 2) of Ga compositions grown before Series 3, which I analysed in Chapter 4. Comparison between all three growth series has not been done before, which makes it an important study on the progress of this series. Based on the study by Elliott et al. (2012), a comparison will be made on the threshold current density as function of temperature, absorption spectrum, edge-photovoltage spectroscopy measurement and optical mode loss per unit length. Throughout this chapter data for Ga = 0.56 from Series 3 is included, even though there is no comparator sample in Series 2 to give a better picture of the whole result. Now let us look at the threshold current density.

5.2 Threshold current density comparison

In this section, only the comparison for Series 2 and 3 is shown, as the Series 1 had a much higher threshold current density (Elliott et al. 2012). This is due to the intended low Al composition in the cladding layers. Lowering the Al composition in the cladding layer of the (AlGa)InP, from Al = 1.0 composition (Series 2 & 3) to Al = 0.70 (Series 1) tends to lower the optical confinement factor (Γ) of the devices. The lowering of this confinement factor (Γ) causes the threshold current density to be increased as reported by other related studies (Bour 1993; Kim et al. 2006). Figure 5.1 shows that all the Ga compositions in Series 3 have lower threshold current temperature-dependence except for Ga = 0.54. The Ga = 0.54 seems to be

maintaining its threshold current density for these two series. Further investigation is needed to understand this comparison by looking into the absorption spectra of these series.

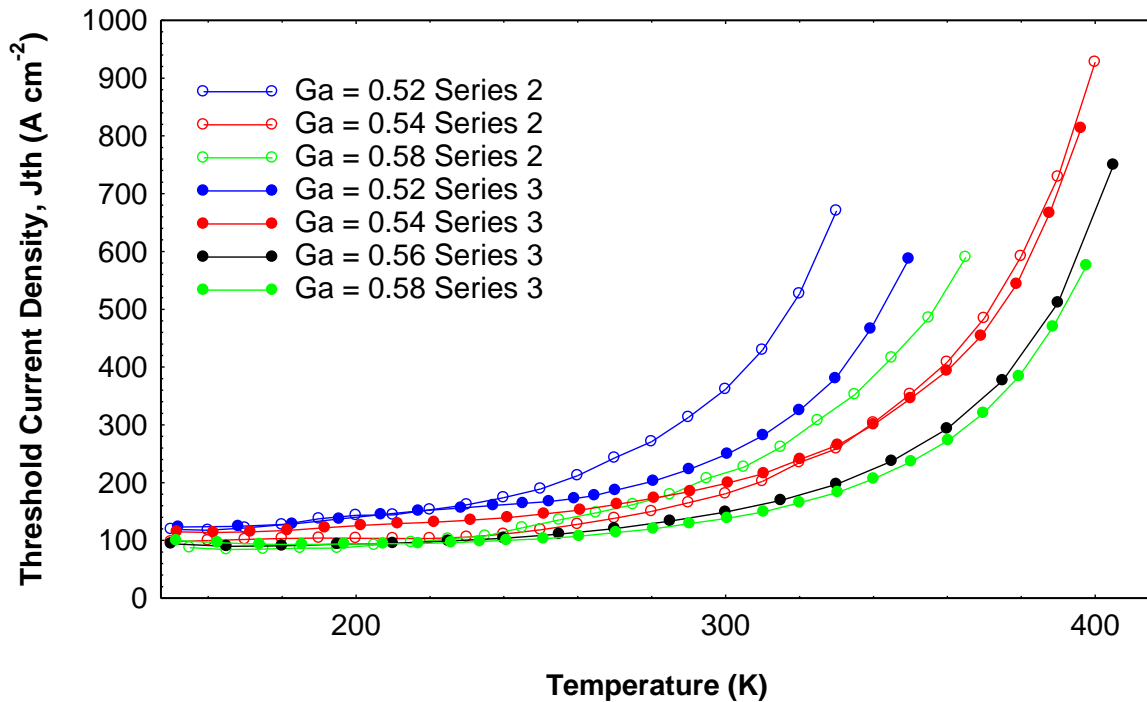


Figure 5.1: Threshold current density as a function of temperature for Series 2 adapted from Elliott et al. (2012) and 3.

5.3 Absorption spectrum comparison

All the 3 series will be compared in terms of their absorption spectra, this includes the data from the previous study (Elliott et al. 2012). The difference in the p-cladding layer growth temperature of these series will be compared to a previous study (Smowton et al. 2010) on the effect of different growth temperatures. Moreover a comparison at a fixed absorption amplitude and comparison of dot large ground state (LGS) energies will also be discussed.

5.3.1 Absorption spectrum energy

Figure 5.2 shows a comparison of optical absorption spectra of these series. Series 1 and 2 seems to follow the same trend as mentioned in Section 4.4 in Chapter 4 for Series 3,

where the features move to higher energy with higher Ga composition. All of Series 1 is at a higher energy than the rest. The reason for this is due to the difference in the p-cladding growth temperature as mentioned in previous study (Elliott et al. 2012). It is clearly seen that the dot absorption spectra of all Ga = 0.54 structures are more well defined and higher than those of other Ga compositions. This is true for all the growth series. This finding is related to the third growth series result mentioned in the previous section 4.4 in Chapter 4, which mentioned about the lowering of the inhomogeneous broadening in Ga = 0.54. Another feature to look at are the small dot (SD) peaks adapted from Al-Ghamdi et al. (2013, p.390), which shows change in energy between Series 1 and 3, where 35 meV for Ga = 0.52, 28.7 meV for Ga = 0.54 and 33.1 meV for Ga = 0.58. Next, I will look at how changing growth temperature can have effect on the SD peaks.

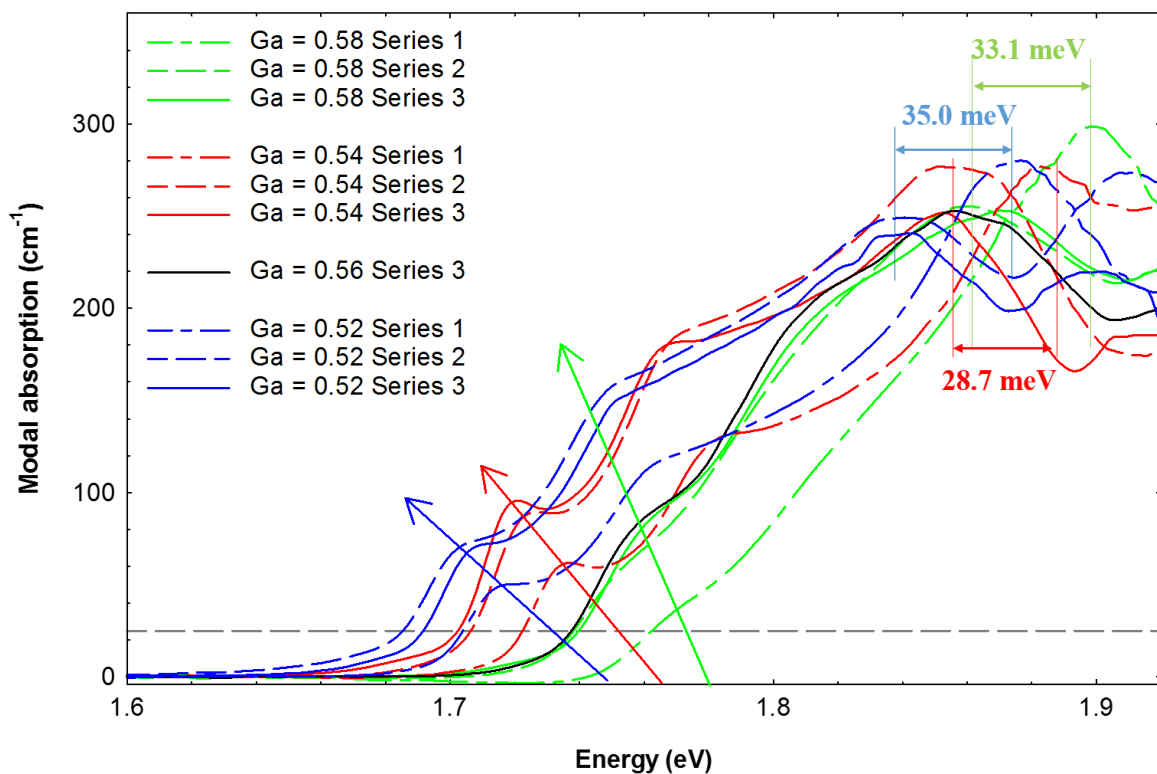


Figure 5.2: Shows the comparison of optical absorption spectra of these series. Series 1, 2 and 3 seems to follow the same trend as mentioned in Chapter 4, although Series 3 is at a higher energy than the rest. Data series 1 and 2, adapted from Elliott et al. (2012, p.3). The small dot (SD) peaks adapted from Al-Ghamdi et al. (2013, p.390), show changes in energy between Series 1 and 3, where 35 meV for Ga = 0.52, 28.7 meV for Ga = 0.54 and 33.1 meV for Ga = 0.58.

5.3.2 Comparison of growth temperature

The p-cladding growth temperature were intended to be set at 690°C for Series 2 (Elliott et al. 2012) and 3 (the current series), and 710°C for Series 1 (Elliott et al. 2012). Based on a previous study (Smowton et al. 2010) on different growth temperatures for the QD shown in Figure 5.3, the energy difference, for example at 25 cm⁻¹ between growth temperatures 690°C to 710°C is 32.4 meV, and between 710°C to 750°C is 39.3 meV. Therefore, one can speculate that changing the QD growth temperature from 690°C to 710°C (32.4 meV) has similar effect to the changing the p-cladding growth temperature from 690°C to 710°C. By changing the p-cladding growth temperature from 690°C to 710°C, changes the SD peak energies (Figure 5.2) in the range of 28.7 – 35.0 meV. This means that increasing the p-cladding growth temperature of Series 1 shifted the SD peak energy to a higher energy. Next, I will look at the comparison of the LGS energies of the growth series.

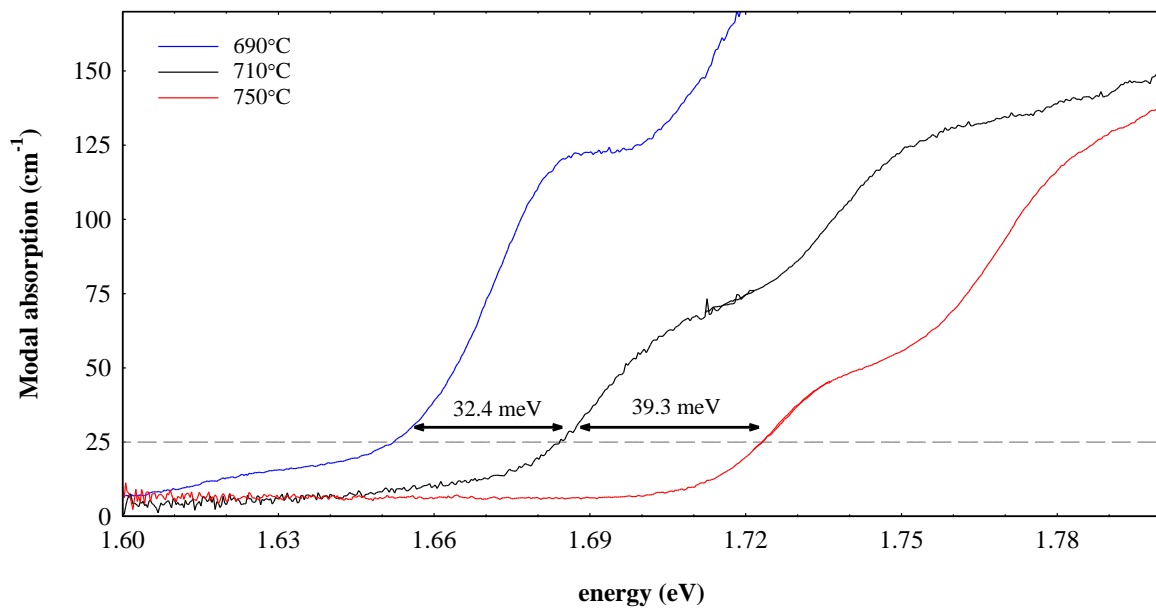


Figure 5.3: Different growth temperature for comparison. A horizontal line similar to Figure 5.2 is drawn for comparison, adapted from Smowton et al (2010, p.89).

5.3.3 Comparison of dot large ground state energies

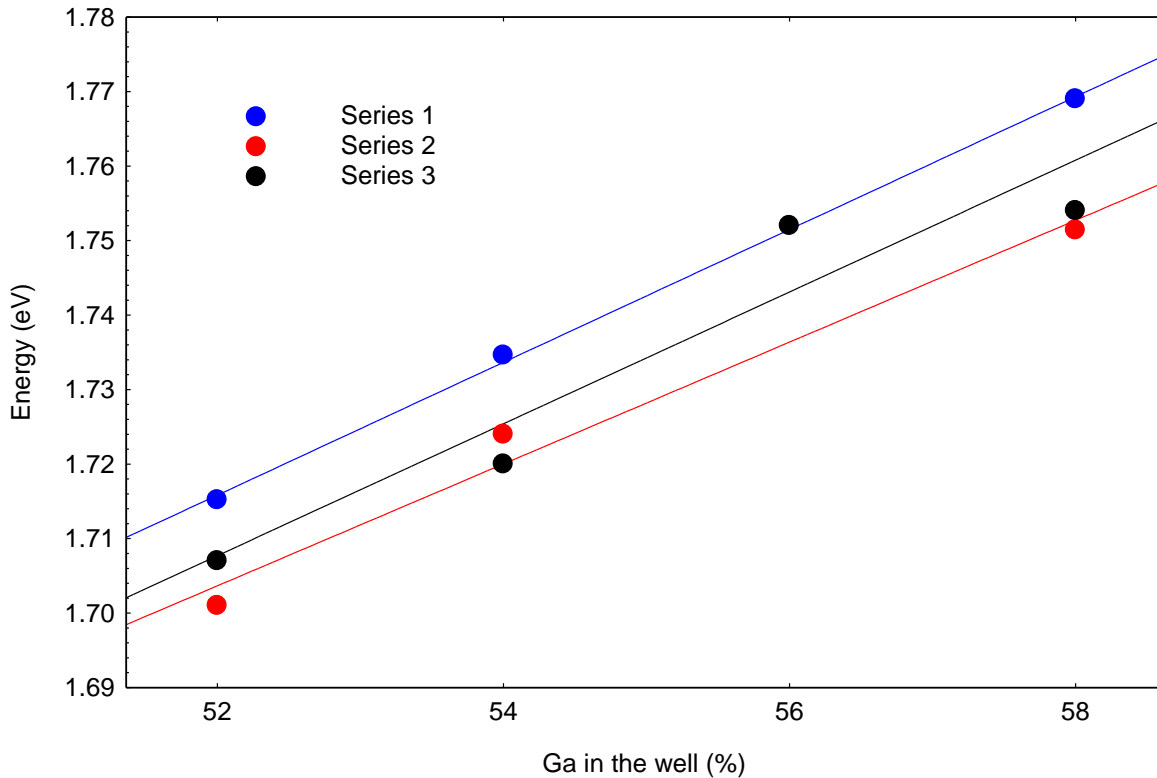


Figure 5.4: Comparison of growth series of large ground state energies with best fit lines through each data series, taken from Table 5.2 (indicated with large arrows).

Using the data in Figure 5.2, values of large ground state energies (indicated with large arrows) were extracted and plotted in Figure 5.4. This figure shows the comparison between the three growth series in terms of dot ground state energy as a function of Ga composition with best fit lines drawn on each series. The series are almost parallel in terms of gradients, which suggests a simple offset. As indicated earlier, the difference between these series is the intended change in the p-cladding growth temperature mentioned previously.

5.4 QW and QD transition energies

There are two separate experiments that can be combined to show the transition energies of these series. Based on previous study (Elliott et al. 2012) of Series 1 and 2,

measurement of absorption spectra with the segmented contact technique can be combined with the EPVS transition energies spectra for calibration.

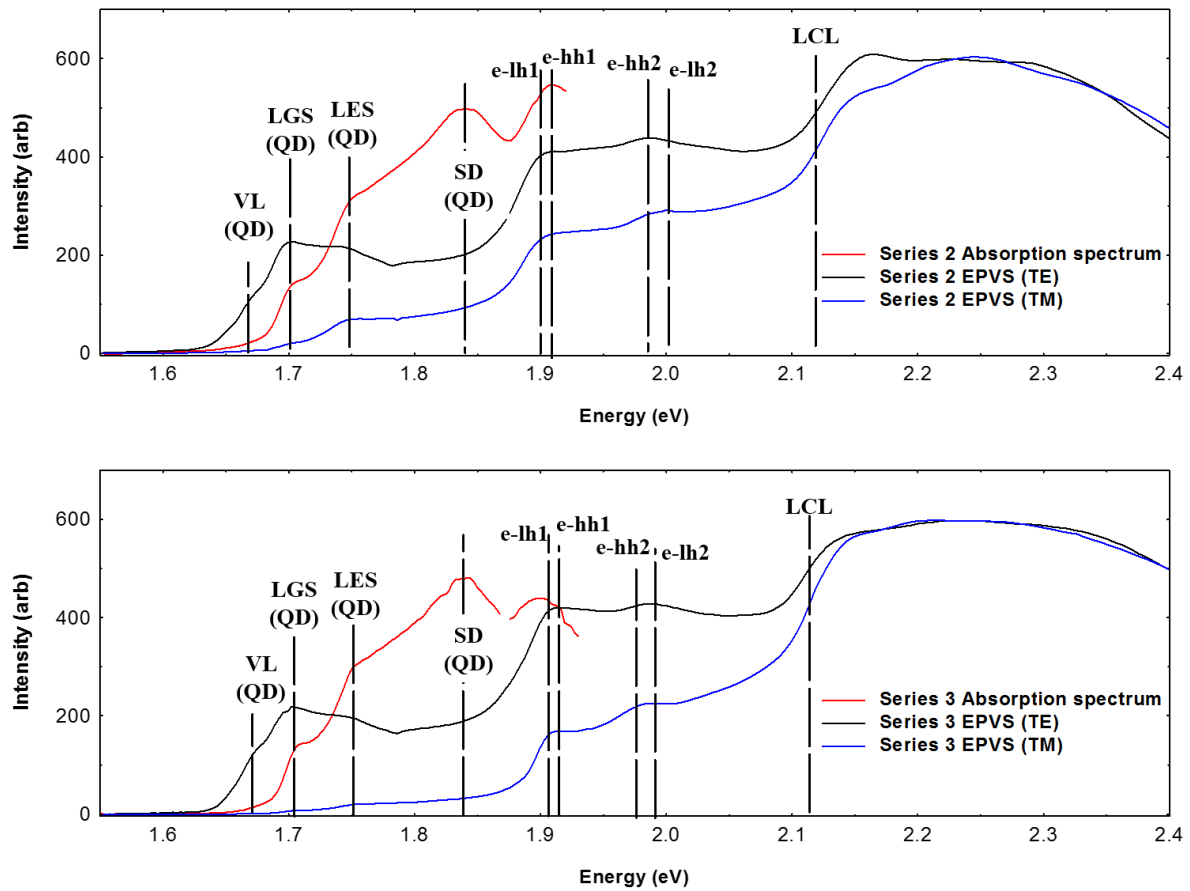


Figure 5.5: Comparing transition energies for Ga = 0.52 gallium composition for Series 2 & 3 taken at 300K for TE and TM of the EPVS measurement and the absorption spectrum measurement of the segmented contact method. The figure shows three sets of features: measured quantum dots energies; very large (VL), large ground states (LGS), large excited states (LES) and small dots (SD) quantum dots, adapted from Al-Ghamdi et al (2013, p.1). The measured quantum dots large ground states (LGS) and large excited states (LES), the measured quantum well: e-lh and e-hh, and the lower confining layer (LCL) transition energies is similar to Figure 4.9 in Chapter 4. Combination of both experiment, adapted from Elliott et al (2012, p.4).

Features indicated in a previous study (Al-Ghamdi et al. 2013) on the absorption spectrum with the segmented contact technique can show a clear features of quantum dots energies that can be overlapped with the features in the EPVS data. An example Ga = 0.52 of Series 2 & 3 is shown in Figure 5.5. This figure shows three absorption curves, two from the

EPVS measurement (TE and TM spectra) and one from the absorption spectrum of the segmented contact method (SCM). The figure shows four sets of measured quantum dot energies: very large (VL), large ground states (LGS), large excited states (LES) and small dots (SD) (adapted from Al-Ghamdi et al. 2013). Measured quantum well: e-lh and e-hh and the lower confining layer (LCL) transition energies (adapted from Elliott et al. 2012), which is similar to Figure 4.9 in Chapter 4 with extra features VL and SD. In this example, almost similar energy transitions were observed between series 2 and 3. The summary of the transition energies of all the samples will be explained in the next section.

5.5 Summary of the transition energies of three growth series

A results summary of transition energies for all EPVS measurements and absorption spectra using the segmented contact technique measurement for Series 2 and 3 taken at 300 K were combined with the existing data of Series 1 (Elliott et al. 2012). Figure 5.6 shows three sets of data. The explanation for Figure 5.6 will be divided into three regions: LCL, UCL and QD.

In the LCL transitions region of the Figure 5.6, the calculated LCL value for Series 1 is at a constant 2.093 eV as mentioned in Table 2.1 in Section 2, while the average LCL value of Series 2 and 3 is 2.121 ± 0.020 eV, which is 33.2 meV difference in energy between them.

Figure 5.7 shows the UCL transitions region, at first glance, it can be seen that both ground and excited states (e-lh and e-hh) in measured Series 2 and 3 data lies close to the calculated energies e-lh and e-hh of Series 1 (Elliott et al. 2012). It can also be seen that the energy of the e-hh energy level is above the e-lh energy in the ground state of the UCL. This change is due to the tensile strain (Elliott et al. 2012) affecting the energy gap, because of the UCL composition change as predicted in previous studies (Yablonovitch and Kane 1986; Adams 1986; Coldren and Corzine 1995). This strain effect is clearly shown in Figure 2.14

adapted from Mogensen (1996) and Coldren et al (2012) in Chapter 2. Looking at the e-hh1 transition (all red lines) in the ground state of Series 2 and 3, the measured e-hh1 values (red dashed line and thin red line) are lower in energy compared to the calculated e-hh1 energy value (thick red line) of Series 1, while in the case of the e-lh1 transition (all blue lines) in the ground states of Series 2 and 3, the measured e-lh1 values (blue dashed line and thin blue line) are lower in energy than the calculated e-lh1 value (thick blue line) of Series 1. One reason for this is might be that as the p-cladding layer of Series 1 was grown at a higher temperature (710°C), more inter-diffusion between the quantum well material and the surrounding active region caused a shift in the light hole of the ground and excited states to a higher energy value due to a change in the strain in the quantum well.

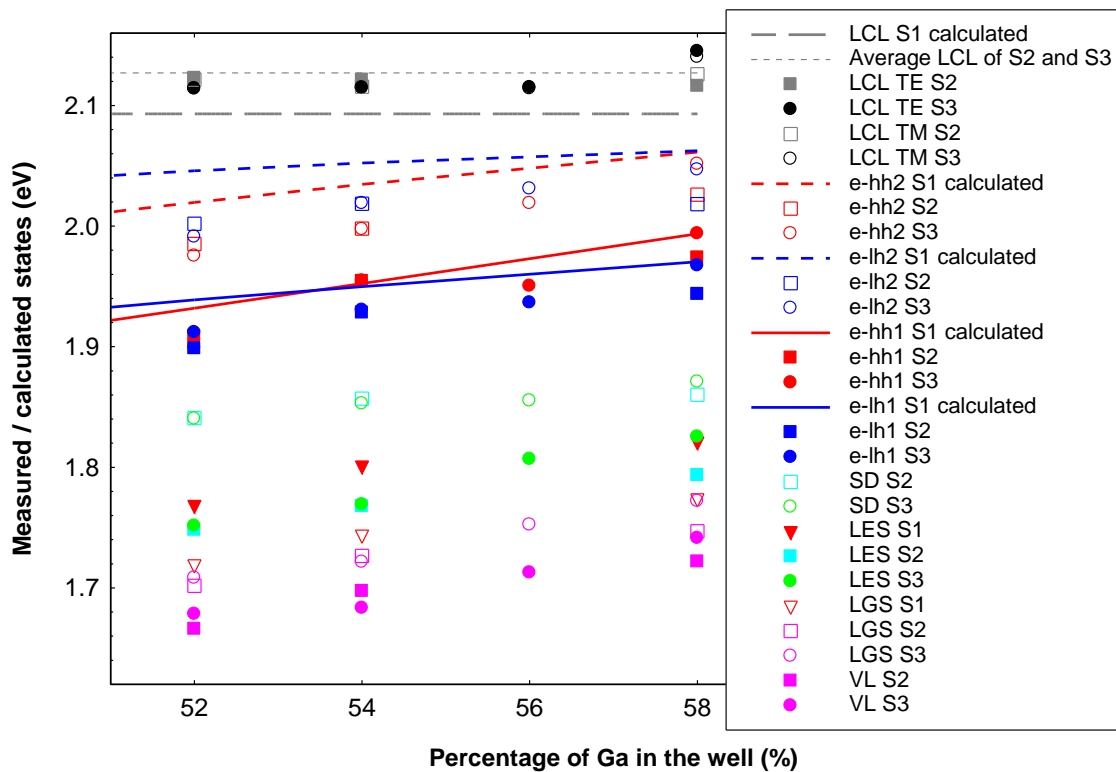


Figure 5.6: Transition energies for all the gallium composition structure for Series 1, 2 & 3 were summarised, taken at 300K. There were three shapes used in this diagram, triangle (∇) represent Series 1 (S1) adapted from Elliott et al (2012, p.4), square (\square) Series 2 (S2) and circle (\circ) Series 3 (S3). The data comprise of three regions: measured QD, measured and calculated UCL and the measured and calculated LCL. The small dashed line is the average measured LCL (2.121 ± 0.020 eV). Calculated dashed lines of LCL of the material (2.093 eV) from Series 1 (Elliott et al. 2012, p.4).

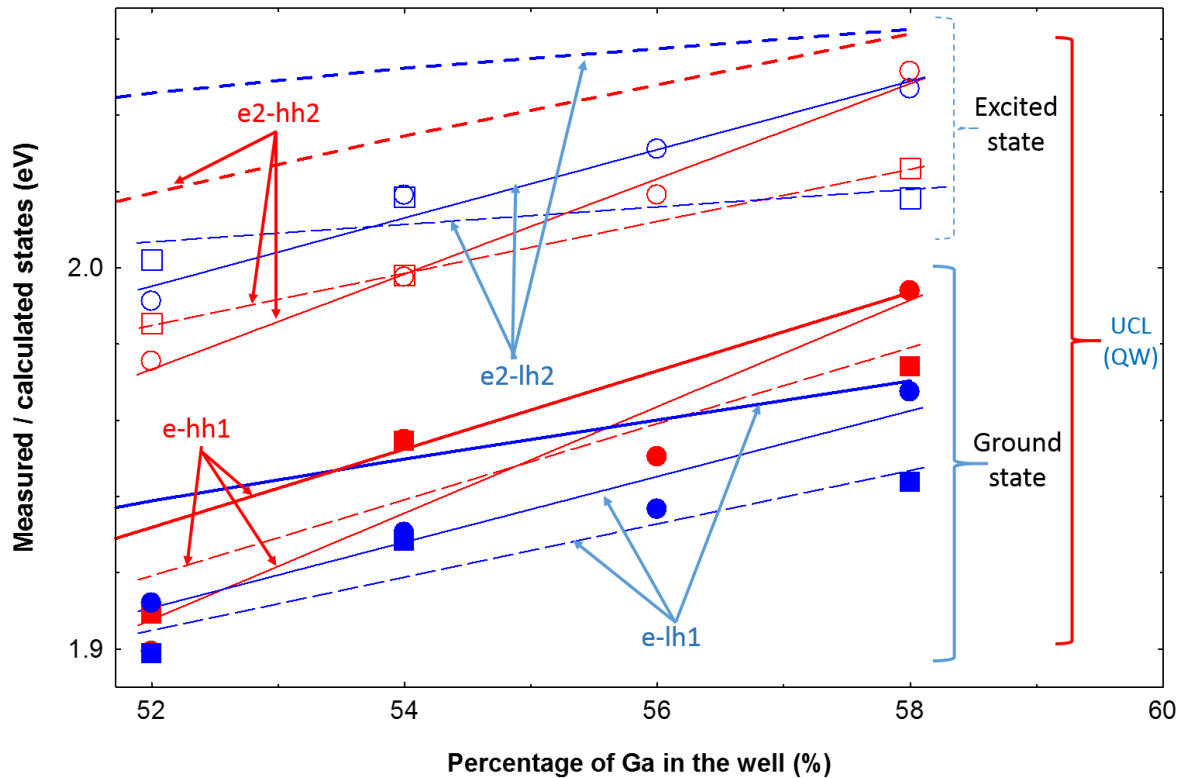


Figure 5.7: Focussing on the transition energies of the UCL (taken from Figure 5.6). The calculated Best fit lines for Series 1 as mentioned in Figure 5.6(a). Best fit lines added for comparison: at ground state e-lh1 (thin blue line – Series 3 and blue dashed line – Series 2) and e-hh1 (thin red line – Series 3 and red dashed line – Series 2), at excited state e2-lh2 (thin blue line – Series 3 and blue dashed line – Series 2), e2-hh2 (thin red line – Series 3 and red dashed line – Series 2).

Figure 5.8 shows the quantum dot transition region, small dots (SD) for Series 2 and 3 show a slow increase in energy as gallium composition increases. The large excited states (LES) show an increase in energy as gallium composition increases for all series and this is also true for the large ground states (LGS). Lastly, very large (VL) quantum dots for Series 2 and 3 shows an increase in energy as gallium composition increases. These increases in energy indicate that the quantum dot distributions are within expected limits of each grown Ga composition series. The transition energies of UCL and quantum dot increases almost at the same magnitude i.e. parallel to each other in Figure 5.6 as Ga composition increases and this was also reported in Elliott et al (2012). This could cause some carrier leakage to the LCL at elevated temperatures as the UCL draws closer to the surface of the well at increasing Ga

composition. This is clearly indicated in Section 4.16 in Chapter 4, where more carrier leakage in Ga = 0.58 compared to Ga = 0.54 for both unamplified spontaneous emission at $J_{6\text{cm}^{-1}}$ and $J_{46\text{ meV}}$ around 2.06 meV near the LCL. Next I will compare the mode loss per unit length between Series 2 and 3.

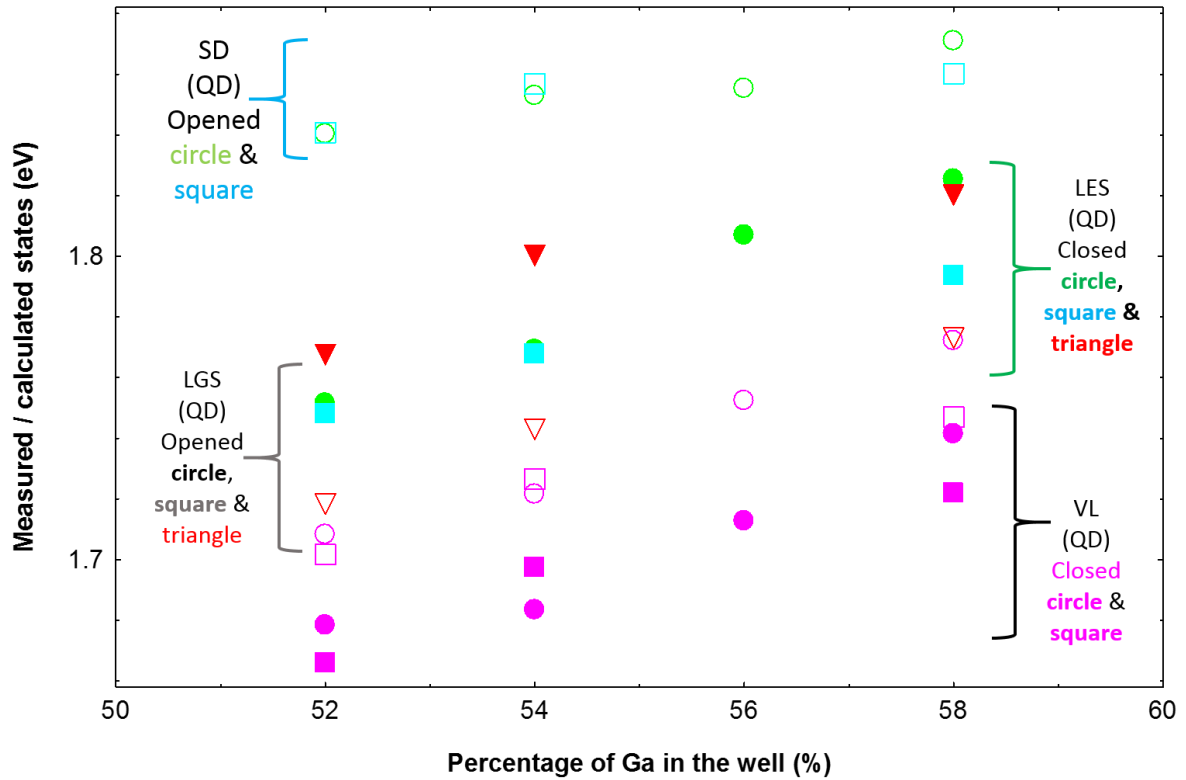


Figure 5.8: Focussing on the four sets of measured quantum dot energies (taken from Figure 5.6): very large (VL), large ground states (LGS), large excited states (LES) and small dots (SD) (adapted from Al-Ghamdi et al. 2013). There were three shapes used in this diagram, triangle (∇) represent Series 1 (S1) adapted from Elliott et al (2012, p.4), square (\square) Series 2 (S2) and circle (\circ) Series 3 (S3).

5.6 Optical mode loss comparison

The optical mode loss per unit length of each Ga composition in the UCL in Series 2 and 3 is shown in Table 5.1. In this table, the α_i values for Series 3 (the current series) is based on the average value of peak modal gain of different temperatures (240 – 400 K) as mentioned in Table 4.1 in Chapter 4. The Series 2 is only based on the 300 K reading, which explains the large uncertainty of optical mode loss (α_i) values of Series 2. To compare the threshold current

density of each Ga composition in the UCL between Series 2 and 3 from Figure 5.1, a simple estimation of the threshold current density using the modal gain versus current density from Figure 4.15(b) at 300K is used. Since the Ga = 0.54 threshold current density as a function of temperature curves is overlapping as shown in Figure 5.1, only Ga = 0.52 and 0.58 composition of Series 2 and 3 will be compared in this case. The estimated peak modal gain of Series 2 (Ga = 0.58) is at 9.5 cm^{-1} (i. e. $G = 3.5 \text{ cm}^{-1} + 6\text{cm}^{-1}$). Therefore by using Figure 4.15(b)(i) to estimate the current density, the graph shows that the current density of Ga = 0.58 of Series 2 is about $238 \pm 20 \text{ A cm}^{-2}$. The threshold current density of Ga = 0.58 of Series 2 data, is estimated to be $218 \pm 20 \text{ Acm}^{-2}$. This is at a difference of 20 Acm^{-2} , which is within experimental uncertainty.

| Percentage of Ga _(x) In _(1-x) P upper confinement layers | Optical mode loss (α_i) (cm^{-1}) | |
|--|---|-----------------|
| | Series 2 | Series 3 |
| 0.52 | 7.4 ± 2.0 | 1.10 ± 0.30 |
| 0.54 | 3.0 ± 1.0 | 2.30 ± 0.30 |
| 0.56 | n/a | 0.03 ± 0.20 |
| 0.58 | 3.5 ± 1.0 | 0.02 ± 0.40 |

Table 5.1: Optical mode loss per unit length for each Ga composition in each series is extracted from the peak modal gain (G) at a current density corresponding to threshold current density of a 2-mm-long laser at 300 K. In Series 3, the average G values as a function of temperature (Table 4.1) is used. As for Series 2, the G values are taken only at 300 K in this comparison, therefore the errors are larger.

Thus, one can say that the improvement in the threshold current temperature dependency in Series 3 compared to Series 2 in terms of Ga = 0.58, is due to the lowering of the optical mode loss value in Series 3. This is also true for Ga = 0.54 in Series 2 & 3, where their similarity is due to the comparable value of their optical mode losses, which explains the overlapping of their threshold current density. Using similar steps on Ga = 0.52 of Series 2, the

peak modal gain is 13.4 cm^{-1} (i. e. $G = 7.4 \text{ cm}^{-1} + 6\text{cm}^{-1}$), which is about $585 \pm 30 \text{ A cm}^{-2}$ as estimated in Figure 4.15(b)(i). Placing this current density value on the graph of $G_a = 0.52$ of Series 2 data in Figure 5.1, indicates that the current density is $360 \pm 30 \text{ A cm}^{-2}$. This is at a difference of 225 Acm^{-2} above the expected value. Even by taking the lower value of loss (i.e. 5.4 cm^{-1}), such that the peak modal gain is 11.4 cm^{-1} (i. e. $G = 5.4 \text{ cm}^{-1} + 6\text{cm}^{-1}$), which is about $440 \pm 30 \text{ A cm}^{-2}$ and with the same current density of $360 \pm 30 \text{ A cm}^{-2}$. There is still a difference of 80 Acm^{-2} above the expected value. This means not only it is different in the optical mode loss value, but there is also another unknown characteristic which cannot be explained further. Whatever seems to be the problem, it lies beyond the simple estimation of the threshold current density using the modal gain versus current density previously mentioned. Thus, one can conclude that the lowering of the optical mode loss plays an important role, not only in lowering the threshold current density but also lowering the threshold current temperature-dependence of these series.

5.7 Summary

| Experiment | Result |
|---|--|
| 1. Threshold current density comparison between Series Growth 2 and 3 are compared. | Lowering the Al composition in the cladding layer of the AlInP, tends to lower the optical confinement factor (Γ) of the devices. The lowering of this confinement factor (Γ) causes the threshold current density to be increased. |
| 2. The optical absorption spectra of Series 1, 2 and 3. | The optical absorption spectra of Series 1 and 2 seem to follow the same trend as Series 3, where the features move to higher energy with higher Ga composition. All of Series 1 is at a higher energy than the rest. The reason for this is probably the difference in the p-cladding growth temperature. |
| 3. The optical mode loss comparison showed the optical mode loss per unit length of each Ga composition in the UCL in Series 2 and 3. | The results show that the improvement in the threshold current temperature dependence in Series 3 compared to Series 2 in terms of Ga = 0.58, was due to the lowering of the optical mode loss value in Series 3. This is also true for Ga = 0.54 in Series 2 and 3, where their similarity is due to the comparable value of their optical mode loss, which explains the overlapping of their threshold current density. In conclusion, the optical mode loss plays an important role, not only in lowering the threshold current density but also lowering the threshold current temperature-dependence of these series. |

Chapter 6

Conclusion and Future Work

6.1 Introduction

InP semiconductor quantum dot lasers are interesting optoelectronic devices with unique properties that need to be understood and utilised for applications such as photodynamic therapy or any such applications that can make full use of its wavelength range of 680 – 750 nm. In this study I have looked into the properties of wafers having Ga composition of 0.52, 0.54, 0.56 and 0.58 in the quantum well upper confining layer above each dot layer, which shows an improvement in lowering the temperature dependence of the threshold current. The conclusions and further work are discussed next.

6.2 Conclusions for Chapter 4 and 5

Threshold current densities of InP quantum dot lasers with $\text{Ga}_{(x)}\text{In}_{(1-x)}\text{P}$ upper confinement layers (UCL) with $x = 0.52$ to $x = 0.58$ show an improved performance with respect to lowering the threshold current density and lowering the temperature dependence of threshold current density in this 3rd growth Series. The laser with a composition of $x = 0.58$ had the lowest threshold current density across the temperature range 240-400 K. At 300 K a value of 138 A.cm^{-2} was obtained compared to a previous best of threshold current density of 150 A.cm^{-2} at 300 K for 2-mm-long lasers. Moreover, improvement is seen for $\text{Ga} = 0.58$ with a low value of 235 cm^{-2} achieved and a low value of $\text{Ga} = 0.56$ at 256 cm^{-2} , both at 350 K.

The main reason for this study is to identify the factors in the improved performance of lasers with respect to lowering the threshold current density and lowering the temperature dependence of threshold current density for samples with different Ga composition in the upper confining layer (UCL). Therefore, a technique called the segmented contact method using the

same laser structure and fabricated into sections as mentioned in Chapter 3 is used. The value of the segmented contact technique is to separate out the effect of the increased inversion level and the increased current density required to compensate for the increased carrier spreading from other factors as reported by Smowton et al. (2011). Since the measurement used in this study involved the comparison between laser and segmented contact devices, several tests were carried out to make sure that their comparability is due to their characteristics not for other reasons. In Chapter 4, I began by introducing the characteristics of the wafer grown with different Ga compositions with samples selected from random areas of the wafer to be processed into segmented contacts and laser devices. The result of the characterisation of the samples selected in terms of threshold current and current density proves that the differences that exist between samples is due to random variations that is affecting the whole sample, rather than the effect of uneven growth across the wafer. Wavelength measurements indicate that QD and QW states are equally affected by the change in Ga composition. Looking at the transition energies between laser and segmented contact devices taken at different place on the same wafer sample, showed some energy difference but this was not significant compared to the large energy difference between the Ga compositions. It is established that there is no drastic change in the fundamental characteristics of any significance apart from the effects due to Ga composition.

Several lengths of lasers were used in this study and at the end it was decided that a 2-mm-long laser device is the most suitable length for comparison. This is because it is comparable to a 3- and 4-mm device and yet has a lower threshold current density when compared to a 1-mm device. Moreover, a 2-mm device is useful in comparison with earlier series in the Chapter 5. In general, the data for the current density to achieve a peak net modal gain of 6 cm^{-1} of the segmented contact method is expected to agree with the threshold current density from laser measurements. In theory, the peak of the net modal gain ($G - \alpha_i$) value of 6

cm^{-1} for a 2-mm-long laser is also expected to coincide with the lasing energy of the 2-mm-long laser (Snowton and Blood 2010). The mode loss per unit length (α_i) is normally determined as the value that the loss ($A + \alpha_i$) and gain ($G - \alpha_i$) spectra tend to at low photon energy, which is subject to experimental uncertainty and a systematic error due to sample alignment. Therefore, a new way of determining the mode loss per unit length was introduced by extracting the energy of the peak net modal gain value of 6 cm^{-1} for a 2-mm-long laser from the averaged value of the modal gain (G), which is more accurate and significant than determining α_i just at the value which loss and gain spectra tend to at low photon energy. The highest α_i value is 2.30 cm^{-1} for $\text{Ga} = 0.54$, 1.10 cm^{-1} for $\text{Ga} = 0.52$, and $\text{Ga} = 0.56$ and 0.58 have almost zero α_i values.

To maintain the same peak gain at 300 K as at a higher temperature for instance 360 K, one will need to compensate for two situations. First, increasing the current density to achieve 300 K inversion level to compensate for the nonradiative recombination processes and secondly adding more current density on top of that to compensate for the carrier spreading to higher energy states. Spontaneous emission rate spectra measured at $J_6 \text{ cm}^{-1}$ show more filled QW states for $\text{Ga} = 0.54$ compared to $\text{Ga} = 0.58$ and compared with data taken at constant inversion level indicating that more carriers are supplied to the $\text{Ga} = 0.54$ to compensate for its high optical mode loss (α_i), when compared to $\text{Ga} = 0.58$. As the temperature increases, some of the energetic carriers from the QW escape to the lower confining layer (LCL) and spontaneous emission measurements show this happens more in the $\text{Ga} = 0.58$ than in the $\text{Ga} = 0.54$.

Three series of samples grown at different times but with similar designs were compared in the study. Lowering the Al composition in the cladding layer, tends to lower the optical confinement factor (Γ), which caused the threshold current density to be increased in

Series 1. The results show that α_i plays the dominant role, not only in lowering the J_{th} but also lowering the threshold current temperature-dependence of these series.

6.3 Future work

In this thesis, three different growth series have been discussed. A significant amount of improvement such as lowering the threshold current density, reducing the threshold current temperature-dependence and lowering of the internal mode loss per unit length of the different Ga composition have been dealt with in this study. Moreover, if the mode loss per unit length (α_i) could be made the same for all the Ga composition, Ga = 0.54 composition would have the lowest threshold current density and better material quality amongst the other Ga compositions.

Looking at the unamplified spontaneous emission through the top-contact window gave a good indication of the thermal activated leakage beyond the active region of these structures as shown in Chapter 4 & 5. Previous work (Wood et al. 1999) shows direct evidence for electron leakage through the p-cladding of previous devices. More careful investigation is needed to investigate this situation in future growth series for further improvement in reducing the electron leakage in the cladding layer. Changing Ga composition is fully utilised in three growth series, thus improvement will not come from changing the current selection of Ga = 0.52 to 0.58. One thing to try would be varying the Al composition in the lower confining layer (LCL) higher than 0.30. The variation of the Al compositions will also have an effect of controlling the amount of carrier leakage in the cladding layer, which indirectly has an effect on active region of the InP/GaInP of quantum dot semiconductor lasers. Instead of Al = 0.3 in barrier $(Al_{0.3}Ga_{0.7})_{0.52}In_{0.48}P$, values up to 0.7 as suggested by Bour (1993) could show an improvement of electron confinement.

References

- Adams, A. R. 1986. Band-structure engineering for low-threshold high-efficiency semiconductor lasers. *Electronics Letters* 22(5), pp. 249 - 250.
- Ahopelto, J. et al. 1999. Selective growth of InGaAs on nanoscale InP islands. *Applied Physics Letters*, 65(13), pp. 1662 - 4.
- Akahane, K. et al. 2010. High Characteristic Temperature of Highly Stacked Quantum-Dot Laser for 1.55- μ m Band. *IEEE Photonics Technology Letters*, 22(2), pp. 103 - 105.
- Al-Ghamdi, M. S. 2009. Optoelectronic properties of InP/AlGaInP quantum dot laser diodes. PhD Thesis, Cardiff University.
- Al-Ghamdi, M. S. et al. 2009. Effect of temperature on threshold current density in InP/AlGaInP quantum dot laser structures. *Int. J. Nano Biomaterials* 2, pp. 147 - 154.
- Al-Ghamdi, M. S. et al. 2013. Absorption, Gain, and Threshold in InP/AlGaInP Quantum Dot Laser Diodes. *IEEE Journal of Quantum Electronics*, 49(4), pp. 389 - 394.
- Arakawa, Y. and Sakaki, H. 1982. Multidimensional quantum well laser and temperature dependence of its threshold current. *Applied Physics Letters* 40(11), pp. 939 - 941.
- Asryan, L. V. and Luryi, S. 2002. Temperature-insensitive semiconductor quantum dot laser", *Solid-State Electronics*, 47(2003) pp. 205 - 212.
- Bernard, M. G. A. and Duraffourg, G. 1961. Laser conditions in semiconductors. *Phy. Status. Solidi* 1(47), pp. 699 - 703.
- Berry, G. 1996. Theoretical studies of electromagnetic wave propagation in semiconductor optical devices. PhD Thesis, Cardiff University.
- Bhattacharya, P. and Mi, Z. 2007. Quantum-Dot Optoelectronic Devices. *Proceedings of the IEEE*, Vol. 95(9), pp. 1723 - 1739.
- Blood, P. 1991. Physics and technology of heterojunction devices. In: Morgan, D. V. and Williams, R. H. *Physics and technology of heterojunction devices*. London: Peter Peregrinus Ltd, pp. 231 - 282.
- Blood, P. 2009. Gain and Recombination in Quantum Dot Lasers. *IEEE Journal of Selected Topics In Quantum Electronics*, Vol. 15(3), pp. 808 - 818.

- Blood, P. et al. 2003. Characterization of Semiconductor Laser Gain Media by the Segmented Contact Method. *IEEE Journal of Selected Topics in Quantum Electronics* 9(5), pp.1275-1282.
- Bour, D. P. 1993. AlGaInP quantum well lasers, Chapter 9. In: Zory, P. S. J, Eds. *Quantum well lasers*. New York: Academic Press, pp. 415 - 460.
- Coldren, L. A. and Corzine, S. W. 1995. *Diode lasers and photonic integrated circuits*. New Jersey: John Wiley & Sons.
- Coldren, L. A. et al. 2012. *Diode lasers and photonic integrated circuits*. New Jersey: John Wiley & Sons.
- Deppe, D. G. et al. 2009. Quantum dot laser diode with low threshold and low internal loss. *Electronic Letters* 45(1), pp. 54 - 55.
- Dutta, N. K. et al. 1984. Analysis of leakage currents in 1.3- μm InGaAsP Real-Index-Guided Lasers. *Journal of Lightwave Technology*. Vol. 2(3), pp. 201- 208.
- Eliseev, P. G. et al. 2000. Transition dipole moment of InAs/InGaAs quantum dots from experiments on ultralow-threshold laser diodes. *Applied Physics Letter* 77(2), pp. 262 - 264.
- Elliott, S. N. et al. 2012. The effect of strained confinement layers in InP self-assembled quantum dot material. *Semicond. Sci. Technol.* 27, pp. 1 - 6, 094008.
- EPSRC National Centre for III-V Technologies. 2011. Metal Organic Chemical Vapour Deposition [Online]. Available at: <http://www.epsrciii-vcentre.com/epitaxyservices.aspx?tab=2>. [Accessed: 13 August 2014].
- Flores, Y. V. et al. 2013. Thermally activated leakage current in high-performance short-wavelength quantum cascade lasers. *Journal of Applied Physics* 113, pp. 134506-1 - 134506-10.
- Fox, M. 2010. *Optical properties of solids*. 2nd ed. London: Oxford University Press.
- George, A. A. 2007. *Carrier Distributions in Long Wavelength Quantum Dot Laser Diodes*. PhD Thesis, Cardiff University.
- Ghiti, A. et al. 1988. Long wavelength strained layer lasers. *Heterojunction and Quantum Well Devices: IEE Colloquium on Physics, Engineering and Applications*. London 27 Oct 1988, London: IET, pp. 1 - 3.
- Griffiths, K. 1992. *Automated Laser Diode Measurement*, MSc Dissertation, Cardiff University.

- Grundmann, M. and Bimberg, D. 1997. Theory of random population for quantum dots. *Physical Review B* 55(15), pp. 9740 - 9745.
- Grundmann, M. et al. 1996. Growth, characterization, theory and lasing of vertically stacked quantum dots". Eighth International Conference on Indium Phosphide and Related Materials, Schwabisch-Gmund, 21-25 Apr 1996. Stuttgart: IEEE, pp. 738 - 741.
- Ioffe Physico-Technical Institute. 2001. Electronic archive: New Semiconductor Materials [Online]. Available at: <http://www.ioffe.ru/SVA/NSM/Semicond/GaInP/basic.html> [Accessed: 02 September 2014].
- Jin, C.Y. et al. 2006. High-performance 1.3 μm InAs/GaAs quantum-dot lasers with low threshold current and negative characteristic temperature. *IEE Proc.-Optoelectron.*, 153(6), pp. 280 - 283.
- Kim, K. W. et al. 2006. Enhanced Performance of an InGaAs/GaAs Single Quantum Well Laser Diode by Introducing a High A-Content Al_xGa_{1-x}As Cladding Layer. *Journal of the Korean Physical Society*, 49(3), pp. 1169 - 1172.
- Lasher G. and Stern, F. 1964. Spontaneous and Stimulated Recombination Radiation in Semiconductors. *Physical Review* 133(2A), pp. A553 – A563.
- Leonard, D. et al. 1993. Direct formation of quantum-sized dots from uniform coherent islands of In-GaAs on GaAs surfaces. *Applied Physics Letters* 63(23), pp. 3203 - 3205.
- Madhukar, A. et al. 1994. Nature of strained InAs three dimensional island formation and distribution on GaAs(100). *Applied Physics Letters* 64(20), pp. 2727 - 2729.
- Matthews, D.R. et al. 2002. Experimental investigation of the effect of wetting-layer states on the gain-current characteristic of quantum-dot lasers. *Applied Physics Letters* 81(26), pp. 4904 - 4906.
- Mobarhan, K. S. (2014). Test and Characterization of Laser Diodes: Determination of Principal Parameters in Application note no. 1, Newport Corporation. [Online]. Available at: http://www.newport.com/servicesupport/PDF_Files/APPNOTE1.pdf [Accessed: 14 September 2014].
- Mogensen, P. C. 1996. Strain limits in (Al_yGa_{1-y})_xIn_{1-x}P quantum well laser diodes. PhD Thesis, Cardiff University.

- Mowbray, D. J. and Skolnick, M. S. 2005. New physics and devices based on self-assembled Semiconductor quantum dots. *Journal of Physics D: Applied Physics*, 38(13), pp. 2059-2076.
- Nishi, K. et al. 1999. A narrow photoluminescence linewidth of 21 meV at 1.35 μm from strain-reduced InAs quantum dots covered by In_{0.2}Ga_{0.8}As grown on GaAs substrates. *Applied Physics Letters* 74(8), pp. 1111-13.
- Pikus, G. E. and Bir, G. L. 1959. Effect of deformation on the hole energy spectrum of germanium and silicon. *Sov. Phys. Solid State*, New York: American Institute of Physics, 1, pp. 1502-1517.
- Riedl, T. et al. 1998. Injection lasers with vertically aligned InP/GaInP quantum dots: Dependence of the threshold current on temperature and dot size. *Applied Physics Letters* 73(25) pp. 3730 - 3732.
- Ryou, J. H. et al. 2001. Photopumped red-emitting InP/In_{0.5}Al_{0.3}Ga_{0.2}P self-assembled quantum dot heterostructure lasers grown by metalorganic chemical vapor deposition. *Applied Physics Letters* 78(26), 4091 - 4092.
- Sayid, S. A. et al. 2010. Temperature sensitivity of 1.55 μm (100) InAs/InP-based quantum dot lasers. *Indium Phosphide & Related Materials (IPRM)*, 2010 International Conference. Kagawa, 31 May – 04 June 2010. Tokyo: IEEE, pp. 1-2.
- Seravelli, L. et al. 2007. Quantum dot strain engineering of InAs/InGaAs nanostructures. *Journal of Applied Physics* 101 024313.
- Silfvast, W. T. 1996. *Laser fundamentals*. London: Cambridge University Press.
- Snowton, P. M. et al. 1996. Role of sublinear gain-current relationship in compressive and tensile strained 630 nm GaInP lasers. *International Journal of Optoelectronics* 10(5), pp. 383 - 391.
- Snowton, P. M. et al. 2005. InP/GaInP Quantum dot lasers emitting between 690-750nm. *IEEE Journal of Selected Topics in Quantum Electronics* 11(5) pp. 1035 - 1040.
- Snowton, P. M. et al. 2007. Gain in p-doped quantum dot lasers. *J. Appl. Phys.* 101, 013107, pp. 1-7.
- Snowton, P. M. et al. 2008. Origin of temperature-dependent threshold current in p-doped and undoped In(Ga)As quantum dot lasers. *IEEE Journal of Selected Topics in Quantum Electronics*, 14(4), pp. 1162 - 1170.

- Snowton, P. M. et al. 2009. InP Quantum Dot 7xxnm Laser Diodes. 9th IEEE Conference on Nanotechnology 2009. Genoa, 26-30 July 2009. Genoa: IEEE, pp. 508 - 509.
- Snowton, P. M. et al. 2010. Effect of growth temperature on InP QD lasers. *IEEE Photonics Technology Letters* 22(2), pp 88 - 90.
- Snowton, P. M. et al. 2011. Temperature-Dependent Threshold Current in InP Quantum-Dot Lasers. *IEEE Journal of Selected Topics in Quantum Electronics* 17(5), pp. 1343 - 1348.
- Snowton, P. M. and Blood, P. 1997. Visible emitting (AlGa)InP laser diodes. In: Manasreh, M. O. ed. *Strained-layer quantum wells and their applications. Optoelectronic properties of semiconductors and superlattices*, Vol. 4. Amsterdam: Gordon and Breach, pp. 431-487.
- Snowton, P. M. and Blood, P. 2010. Quantum Dot Lasers: Theory and Experiment. In: Lee, E.- H. et al. *VLSI Micro- and Nanophotonics: Science, Technology, and Applications*, Ohio: CRC Press, Taylor and Francis Group, 9, pp. 9 - 34.
- Sobiesierski, A. and Snowton, P. M. 2011. Quantum-Dot Lasers: Physics and Applications. In: Bhattacharya, P. et al eds. *Comprehensive Semiconductor Science and Technology*, Vol. 6. Amsterdam: Elsevier, pp. 353 - 384.
- Sreekumar, R. et al. 2011. Effect of high energy proton irradiation on InAs/GaAs quantum dots: Enhancement of photoluminescence efficiency (up to 7 times) with minimum spectral signature shift. *Materials Research Bulletin* 46 (2011) pp. 1786 - 1793.
- T. Riedl, E. et al. 1998. Injection lasers with vertically aligned InP/GaInP quantum dots: Dependence of the threshold current on temperature and dot size. *Applied Physics letters* 73(25), pp. 3730 - 3732.
- Tatebayashi, J. et al. 2003. Low threshold current operation of self-assembled InAs/GaAs quantum dot lasers by metal organic chemical vapour deposition. *Electronics Letters* 39(15) pp. 1130 – 1131.
- Thompson, G. B. H. 1980. *Physics of semiconductor laser devices*. New Jersey: John Wiley & Sons.
- Varshni, Y. P. 1967. Temperature dependence of the energy gap in semiconductors. *Physica* 34(1), pp. 149 - 154.

- Walter, G. et al. 2001. Coupled InP quantum dot InGaP quantum well InP-InGaP-In(AlGa)P-InAlP heterostructure diode laser operation. *Applied Physics Letters* 79(20), pp. 3215 - 3217.
- Wilson, J. and Hawkes, J. F. B. 1987. *Laser principles and applications*. Europe: Prentice Hall.
- Wilson, J. and Hawkes, J. F. B. 1998. *Optoelectronics: an introduction*. 3rd ed. Europe: Prentice Hall.
- Wood, S. A. et al. 1999. Direct monitoring of thermally activated leakage current in AlGaInP laser diodes. *Applied Physics Letters* 74(17), pp. 2540 - 2542.
- Wu, M. C. 2008. Lecture 15: Strained quantum well laser, EE 232 Lightwave devices. University of California [Online]. Available at: <http://www-inst.eecs.berkeley.edu/~ee232/fa08/lectures/EE232-15.pdf> [Access: 02 September 2014].
- Yablonovitch, E. and Kane, E.O. 1986. Reduction of lasing threshold current density by the lowering of valence band effective mass. *Journal of Lightwave Technology* LT-4(5), pp. 504 - 506.
- Zundel, M. K. et al. 1998. Red-light-emitting injection laser based on InP/GaInP self-assembled quantum dots. *Applied Physics Letters* 73(13), pp. 1784 - 1786.

Publications

Conferences:

2012

1. Farfield Divergence of InP Quantum Dot Lasers, Makarimi Kasim, Peter. M. Smowton, Stella N. Elliott and Andrey B. Krysa, 40th Anniversary Conference, Semiconductor and Integrated Optoelectronics, Cardiff, United Kingdom, 02 - 04 April 2012.
2. Farfield Divergence of InP Quantum Dot Lasers. Makarimi Kasim, Peter. M. Smowton, Stella N. Elliott and Andrey B. Krysa. Postgraduate Research Student Conference 28 September 2012.

2013

1. Effect of Ga concentration on the threshold current temperature dependence of InP/GaInP quantum dot lasers, Makarimi Kasim, Stella N. Elliott, Peter M. Smowton and Andrey B. Krysa. Semiconductor and Integrated Optoelectronics, Cardiff, United Kingdom, 09 - 11 April 2013.

2014

1. "Effect of Gallium Concentration in quantum well on the threshold current temperature-dependence of InP Quantum Dot Lasers" and "Understanding the high temperature threshold increase mechanisms in InP quantum dot lasers". Poster and talk during Semiconductor and Integrated OptoElectronics Conference (SIOE 2014). Cardiff, United Kingdom, 29 April - 01 May 2014.
2. "Improved laser performance in NIR InP Dot Based Structures with Strained Layers". IEEE International Semiconductor Laser Conference, 7 - 10 September 2014, Palma Spain. <http://islc2014.exordo.com>.

Papers:

2014

1. “Reducing Thermal Carrier Spreading in Quantum Dot Lasers”. M. Kasim, S.N. Elliott, S. Shutts, A. B. Krysa and P. M. Snowton. IEEE Journal of Selected Topics In Quantum Electronics, submitted.